UNIVERSITÀ DEGLI STUDI DI CAMERINO

School of Advanced Studies

DOCTORAL COURSE IN

SCIENCES AND TECHNOLOGY - THEORETICAL AND
EXPERIMENTAL PHYSICS

XXXIV° **cycle**

CONSEQUENCES OF CONFINEMENT ON VORTEX ORDERING AND DYNAMICS IN SUPERCONDUCTING NANOSTRIPES

PhD Student
Benjamin Alexander McNaughton

Supervisors
Prof. Andrea Perali
Prof. Nicola Pinto
Prof. Milorad V. Milošević

Consequences of Confinement on Vortex Ordering and Dynamics in Superconducting Nanostripes

Thesis submitted in accordance with the requirements of the University of Camerino, Italy, and the University of Antwerp, Belgium, for the degree of Doctor of Philosophy in Physics
by

Benjamin Alexander McNaughton

Supervised by Prof. Andrea Perali, Prof. Nicola Pinto, and Prof. Milorad V. Milošević

May 2022

Dedication

I dedicate this work to ones I love and whom love me so. Perseverance and self-belief will always lead to success. So in the most lost of days never forget that the right path is just a step away. For my little Leonardo.

Acknowledgements

Let me firstly thank my supervisors, Professor Andrea Perali, Professor Nicola Pinto, and Professor Milorad V. Milošević for there support throughout my Ph.D., both professionally and personally. Thank you to my partnering universities, the University of Camerino and Antwerp University for providing me the opportunity to achieve the prestigious accolade of a Ph.D. title. My deep and sincere gratitude to my family, to my son Leonardo and his ever supporting mother Barbara for being my shining stars and believing in me. To my mother for the years of belief, even through my crazy teenage years, and all her love and energy she sacrificed to help me here. To my Dad for all his wisdom he passed on to me, helping me become a man and his continuous acceptance. To my brother and sister for their love and support they gave me over these years. Finally to everyone that I met along the way, that carried me through these years one way or another.

List of Publications

Peer-reviewed Journal Publications

1. McNaughton, B., Pinto, N., Perali, A., & Milošević, M. V. (2022). Causes and consequences of ordering and dynamic phases of confined vortex rows in superconducting nanostripes. Nanomaterials, 12(22), 4043.
2. Pinto, N., McNaughton, B., Minicucci, M., Milošević, M. V., & Perali, A. (2021). Electronic Transport Mechanisms Correlated to Structural Properties of a Reduced Graphene Oxide Sponge. Nanomaterials, 11(10), 2503.
3. McNaughton, B., Milošević, M. V., Perali, A., & Pilati, S. (2020). Boosting Monte Carlo simulations of spin glasses using autoregressive neural networks. Physical Review E, 101(5), 053312.
4. Scriva, G., Costa, E., McNaughton, B., & Pilati, S. (2022). Accelerating equilibrium spin-glass simulations using quantum annealers via generative deep learning. arXiv preprint arXiv:2210.11288.

Contents

Abbreviations

AC   Alternating Current
AVL   Abrikosov Vortex Lattice
BCS   Bardeen-Cooper-Schrieffer
DC   Direct Current
EM   Electromagnetic
GL   Ginzburg-Landau
gTDGL   Generalised Time-Dependent Ginzburg-Landau
IBSC   Iron Based Superconductor
IDE   Intrinsic Detection Efficiency
IR   Infrared
MRI   Magnetic Resonance Imaging
NMR   Nuclear Magnetic Resonance
QUBO   Quadratic Unconstrained Binary Optimization
SN   Superconducting Nanostripe
SNSPD   Superconducting Nanostripe Single Photon Detector
SQUID   Superconducting Quantum Interference Device
V-aV   Vortex-Antivortex
V-V   Vortex-Vortex

Introduction

The scientific field of superconductivity has presented both theoretical and experimental physicists with unexpected findings since its initial discovery. Currently, nanoscale superconductivity is a rapidly developing research area, as scientists endeavor to gain insight into how fluctuations at this scale significantly impact the behavior of superconductors. Superconducting nanostripes (SNs) are a critical component in superconducting electronics, with widespread applications in quantum technology. For example, superconducting nanostripe single-photon detectors (SNSPDs) have been proposed for use in quantum communication, as well as in fields such as astronomy and spectroscopy [1, 2, 3, 4]. These developments have the potential to revolutionize technology and our understanding of the natural world. Superconducting nanostripes are particularly suitable for the detection of individual photons due to their ability to tune the applied biased current in a manner that maximizes their intrinsic detection efficiency [5]. Using the same detection mechanism, SNSPDs can also serve as a bolometer, capable of detecting particle collisions [6, 7]. In addition to single-photon detectors, other examples of superconducting electronics include prototype logic devices [8, 9, 10]. Research has shown that the strength of interactions between vortices and strip edges can be controlled by changing the magnetization orientation in the strips using a small in-plane magnetic field. As a result of the controlled acceleration or deceleration of superconducting vortices, strong tunable anisotropy is introduced into the vortex dynamics, which is highly favorable for the development of logic devices [8]. Reference [10] discusses a study of a superconducting H-bar nanostripe, which revealed that a single row of vortices was the optimal configuration for generating a giant non-local electrical resistance. In this configuration, the vortices were able to move several microns away from the local current drive without being altered by the passing current, enabling feasible long-range information transfer by the vortices.

Another important addition to the family of superconducting electronics is the flux qubit [11, 12, 13], which is a crucial component in the development of quantum computers. Flux qubits can be magnetically coupled, creating a system that is analogous to an Ising spin model [14, 15]. The magnetic coupling of flux qubits is particularly useful because optimization problems can often be transformed into a quadratic unconstrained binary optimization (QUBO) [16, 17]. By allowing the system to relax into the ground state via quantum annealing [18, 19], flux qubits can be utilized to solve a wide range of optimization problems. Superconducting diodes have garnered significant interest for their ability to transport current in a single direction with minimal energy loss, making them highly attractive for numerous applications. The first instance of a magnetically tunable superconducting diode effect was demonstrated in an artificial superlattice [20], which further highlights the potential of superconducting electronics for a wide range of practical applications. The discovery of the magnetically tunable superconducting diode effect in artificial superlattices has generated significant interest in the field, leading to recent studies on the intrinsic mechanisms underlying this effect [21]. Interestingly, studies have also shown that superconducting vortices in fluxon pumps and lenses exhibit diode-like behavior when subjected to alternating current [22, 23]. Specifically, vortices are pumped out of a restricted region of the superconductor, and when AC is applied, the vortices become jammed, leading to the observed diode-like behavior.

Narrow superconducting nanostripes have been shown to exhibit an enhancement in critical parameters. For instance, in an artificial heterostructure consisting of such stripes, the critical temperature was observed to increase from 23 K to 150 K [24]. Furthermore, when the dimensions of stripes are reduced from 3D to 2D, an amplification in the critical current density can occur, as observed for niobium film when the thickness is reduced [25]. The strong confinement forces present at the edges of narrow SNs can significantly impact the behavior of the condensate, particularly that of the vortex lattice due to its topology [26]. The edge barrier [27] creates a strong vortex confinement [28], resulting in effects such as the enhancement of critical current density, as observed experimentally for a NbN nanostripe. Confinement in narrow SNs can also result in significant magnetoresistance oscillations under specific experimental conditions. For instance, time-averaged voltage/resistance as a function of the applied magnetic field displays distinct peaks during transitions between static and dynamic vortex phases [29, 30, 31]. At higher applied fields with multiple rows of vortices or high currents, continuous motion of vortices leads to a monotonic background, on top of which resistance oscillations due to entries of additional vortices are superimposed [29, 32].

Observations of commensurate effects between the width of a superconductor and the number of rows of vortices have revealed a corresponding relationship with the critical current as a function of the magnetic field perpendicular to the plane (with a fixed SN width w), as well as a relationship with the critical current as a function of width (with a fixed magnetic field H), representing a manifestation of confinement effects [33, 34]. Over the years, research has explored the criteria that govern the entry of vortices from the edge of a thin superconductor, with these studies addressing this subject [35, 36, 37, 38, 39]. While it was initially proposed that the current density at the edge of the superconductor exceeding the depairing current (J_{DP}) was the driving mechanism [40], subsequent observations have shown that the edge current actually surpasses J_{DP}, thereby challenging the previous hypothesis. According to Vodolazov's research [39], the criteria governing vortex entry into a superconductor at its edge is a threshold value of the supervelocity (kinematic momentum) at the edge.

Electromagnetic resonators represent a compelling use case for utilizing superconducting nanostripes or films, as demonstrated by several studies [41, 42, 43]. Under the influence of a sufficiently strong transport current, the crossing of vortices through a superconductor-normal metal system results in a dynamic electromagnetic field around the stripe. The highest intensity of the induced magnetic field is concentrated at the edges of the stripe. As a vortex crosses this field, the interaction between the magnetic fields triggers the emission of photons [42]. A solitary vortex crossing through the narrow structure results in the emission of a single photon that necessitates the use of superconducting nanowire single-photon detectors for detection. On the other hand, when a synchronized row of vortices passes through the structure, a much stronger signal is produced, which can be detected experimentally [43].

In the context of narrow SNs, rows of vortices can cross the stripe either asynchronously or synchronously, as reported in several studies [44, 29, 45]. The nature of the crossing is dependent on the competing forces such as confinement, vortex-vortex interaction, and Lorentzian forces, which together dictate the dynamics of the vortex motion. However, despite the extensive research in this area, the criteria governing synchronous crossings remain poorly understood. To gain a comprehensive understanding of the behavior of vortices in superconducting nanowires with small widths, it is important to investigate the favorable geometry of vortex configurations under static conditions (i.e., in the absence of an applied current) and their relationship to the dynamic case (i.e., when an applied current is present). Understanding how a vortex lattice is affected by the interaction with the edge confining force and other dynamic forces is crucial when considering SNs for applications mentioned above, especially EM radiation emitters. Investigating the dynamic dissipative states under strong confinement in the 1D-2D crossover regime can provide insights into the behavior of vortices as they cross superconducting nanostripes under various conditions, such as the width of the stripe, the magnetic field, and the intensity of the applied current. This information is critical to both the fast information transfer and the frequency of emitted radiation by moving vortices. Such studies can reveal how vortices move across the stripe under different conditions and provide additional information on the possible vortex velocity under confinement [46, 47]. Therefore, it is crucial to scrutinize how confinement in superconducting nanostripes affects the vortex configurations and dynamics.

In Chapter I, a chronological overview of superconductivity will be presented, including summaries of the theoretical descriptions for superconductivity, such as the London model, Ginzburg-Landau theory, and BCS theory. The chapter will also cover different types of superconducting materials and provide an overview of their applications in electronics and other fields.

In Chapter II, the generalized time-dependent Ginzburg-Landau (gTDGL) framework will be described, including its uses and validity in nanoscale superconductors. This theory serves as the basis for the results obtained in this thesis and remains an essential tool for the study of superconductors today.

In Chapter III, the confinement of vortices in thin, narrow superconducting nanostripes under static equilibrium conditions will be discussed, using the static case of the generalized time-dependent Ginzburg-Landau equations. The chapter will cover the basics of vortices, including an overview of the criteria for vortex entry, with a focus on the supervelocity. The organization of vortex rows will also be examined, and a vortex row phase diagram as a function of the applied magnetic field, H, for a given width w of the nanostripe will be presented. The critical supervelocity at the edge of the stripe associated with vortex entry will be investigated and shown to be larger for narrower stripes, which corresponds to values found in [39] for wider superconducting nanostripes. The magnetic field dependence of the average number of present vortices will also be analyzed to reveal strong confinement effects. Finally, the reconfiguration from the vortex rows to the vortex lattice with increasing width will be discussed, offering a criterion to define the quasi 1D-to-2D transition, where the nanostripe effectively becomes a nanofilm.

Chapter IV delves into the effects of confinement in the dynamic state. Simulations of voltage-current (V-J) characteristics in SNs demonstrate transitions among different resistive regimes, including Meissner, flux-flow, flux-flow instability, and normal regimes. However, such V-J curves exhibiting similar features to simulations have only been experimentally measured for wider structures, as reported in [48, 49]. The commensurate behavior of the critical current with changes in the magnetic field is also explored. It is shown that the local minima values in $J_{c1}(H)$ (the onset of dissipation) are related to the row transitions displayed in the vortex-row phase diagram. Additionally, the amplification of critical current values through the pinning of vortices is discussed. For stripes with an average vortex area of less than $80\xi^2$ (ξ being the coherence length), vortices cross the SN periodically and continuously under the flux-flow regime, causing modulations of the voltage drop that can be detected experimentally. This process results in the emission of electromagnetic radiation [42], and the power spectra of this radiation can be obtained by performing a fast Fourier transformation of the voltage drop as a function of time [50]. The average vortex velocity obtained from these measurements can be used to discuss the washboard frequencies [43, 42], which can reach up to tens of kilometers per second for thin niobium SNs [49]. Assuming a sufficient vortex density, the transitions of vortex row crossings can vary between quasi-synchronous, synchronous, and asynchronous regimes, which is determined by the interplay of forces acting on the vortices. Synchronised crossings are particularly desirable for small-band electromagnetic emitters in the GHz or THz range. For typical thin niobium SNs [25], modulation frequencies range in the microwave regime, between 1-100GHz. The chapter also covers the dynamics of vortex crossings in viscous condensates, where the rearrangement of the vortex lattice occurs in the presence of defects and high viscosity. At low viscosity, vortex channels can facilitate synchronised vortex crossings, but in the presence of defects that lead to highly viscous condensates, strong distortions can occur in the vortex channels.

Chapter V focuses on the response of superconductors to thermal fluctuations. It includes a brief discussion on how the dynamic behavior can be affected by changes in the material's thermal properties. The chapter then demonstrates how heating can drive the superconductor into the normal state through the creation of a hot belt. Hot superconducting bands can be useful for controlling synchronous vortex crossings, but it is important for the bands to remain narrow in relation to characteristic lengths, such as the coherence length. The mechanism of photon detection in single photon detectors is discussed, including simulations performed on realistic detectors coupled to a shunt resistor. The response of a detector is then examined in terms of delay time, timing jitter, and current crowding caused by the meandering geometry of the typical detector. The intrinsic detection efficiency is summarized as the probability of a detection event on the main component, the superconducting transport current-carrying meandering nanostripe. Finally, the thesis concludes with a summary of the main points.

Chapter 1

Phenomenology and Theoretical Approach to Low Dimensional Superconductivity

1.1 Chronological overview of superconductivity

In 1908, Heike Kamerlingh Onnes ushered in a new era of low temperature physics through the liquefaction of Helium, ultimately leading to the discovery of superconductivity [51]. Three years later, in 1911, Onnes spearheaded a small group of physicists at Leiden Physics Laboratory to observe the phenomenon of superconductivity for the first time [52]. Among these researchers, Gilles Holst and Gerrit Jan Flim, both protégés of Onnes, endeavored to investigate the electrical properties of pure mercury at sub-zero temperatures of 4.2K. As the temperature of the sample was gradually reduced to 4.2K, a dramatic decline in electrical resistance was observed (see figure 1.1). In response to this finding, the researchers meticulously varied the temperature and observed that the behavior persisted, providing unequivocal confirmation of their discovery. Notably, upon cooling the sample to a temperature of 3K, Holst recorded a resistivity decrease by a factor of 10^7 compared to the room temperature value. These experiments ultimately led to the postulation that a material undergoes a sudden change in state below a critical temperature T_c, where electrical resistance vanishes and electric current flows without any dissipation of energy via Joule heating. This profound behavior was identified as the first signature of superconductivity.

The second hallmark of superconductivity was identified twenty-two years later, in 1933, by Walther Meissner and Robert Ochsenfeld at Berlin [53]. They conducted an experiment to evaluate the magnetic field amidst two cylindrical pieces of single-crystal tin. Upon cooling the tin below T_c into a superconducting state and applying a small magnetic field, they discovered that the magnetic field between the two pieces increased. This magnetic field, known as the Meissner-Ochsenfeld effect (as illustrated in figure 1.2(a)), was expelled from the bulk of the superconductor. This expulsion arises from the generation of currents within the superconductor, which subsequently generate a magnetic field that is equal in magnitude and

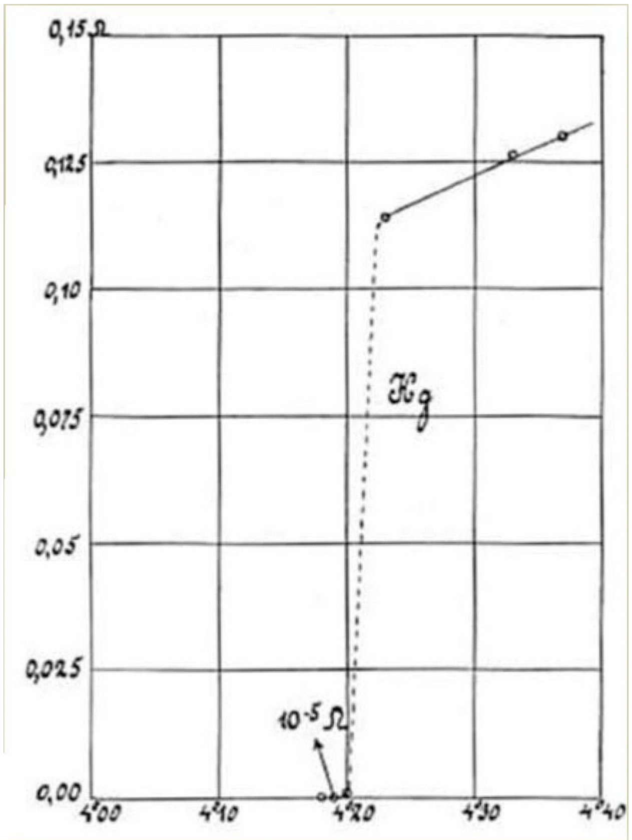

Figure 1.1: Resistivity as a function of temperature for mercury was obtained by K. Onnes when he discovered superconductivity for the first time in 1911 [52].

opposite in direction to the external magnetic field, effectively nullifying the magnetic fields within the bulk of the superconductor. It was observed that the state of perfect diamagnetism persisted until a specific threshold value of the applied magnetic field was reached, beyond which magnetic flux could penetrate the material, depleting its superconducting state. This observation led to the consideration of superconductivity as a second-order phase transition, prompting a thermodynamic approach to explain this phenomenon [54].

In 1935, the London brothers, Fritz and Heinz, formulated a phenomenological theory of superconductivity that explained the Meissner effect exhibited by the superconducting state [55]. Furthermore, the theory predicted that magnetic flux in superconductors would be quantized with a value of $\Phi = \frac{h}{e}$. This prediction was later confirmed in 1961, albeit with a correction $\Phi_0 = \frac{h}{2e}$, signifying that the charge of a superconductor was twice that of an electron [56].

In the year 1950, a significant advancement in the realm of superconductivity theory was made with the development of the phenomenological theory by Vitaly Ginzburg and Lev Landau. This groundbreaking theory characterizes superconductivity as a second-order phase transition, where the order parameter Ψ plays a pivotal role [57]. The Ginzburg-

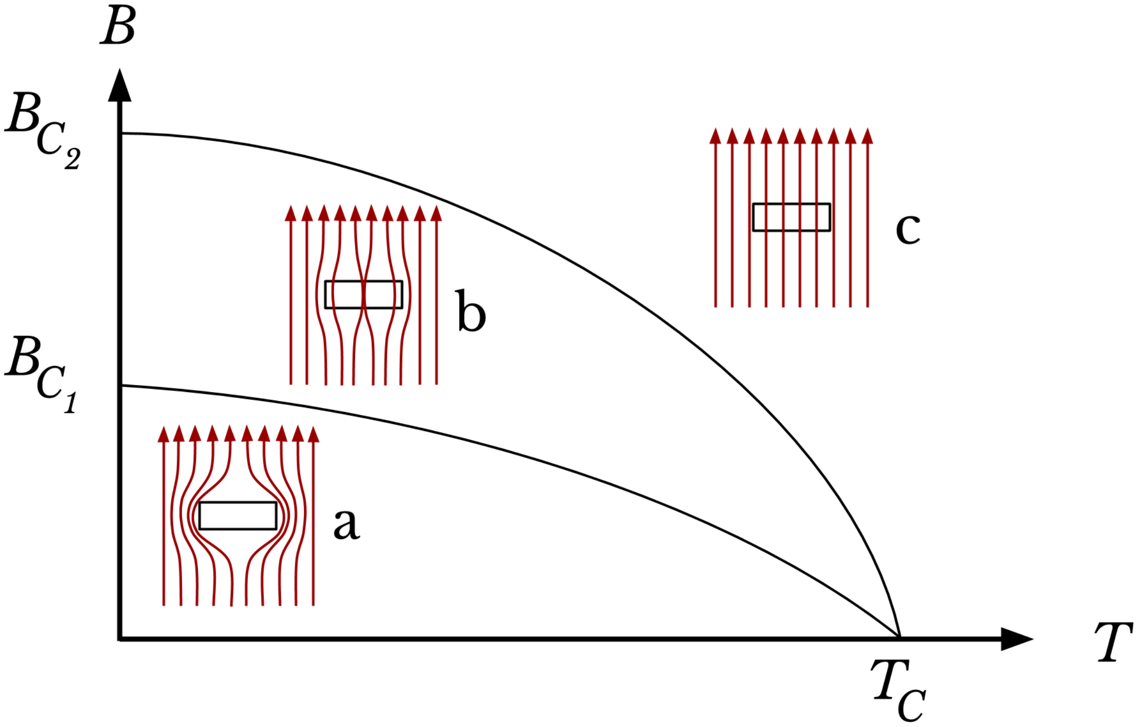

Figure 1.2: Superconducting behaviour for magnetic flux B as a function of absolute temperature T. Critical magnetic flux densities B_{C1} and B_{C2} and critical temperature T_c are indicated on the axes. In region-a, the lower section of the graph, Type-I and Type-II superconductors both exhibit the Meissner effect. Region-b shows type-II superconductivity or the mixed state, where magnetic flux penetrates the superconductor, leading to the nucleation of vortices. At strong magnetic fields greater than B_{C2} superconductivity is destroyed and the material becomes normal, indicated by region-c.

Landau theory is applicable for temperatures that are in close proximity to the critical temperature T_c, which conforms with Landau's theory of phase transitions. This theory elucidates the superconducting state around T_c through a complex order parameter, which serves as a solution to the Ginzburg-Landau equations. These equations bear semblance to the quantum mechanical Schrödinger equation, but they are thermodynamic in nature.

Alexei Abrikosov significantly advanced the field of superconductivity theory by proposing the existence of a new category of superconductors known as type-II. Unlike type-I superconductors that exhibit a positive energy related to the normal-superconducting boundary in the presence of a magnetic field, type-II superconductors display a negative energy. Consequently, type-II superconductors exhibit penetration of the magnetic field, leading to the formation of normal state domains, as portrayed in figure 1.2(b).

Richard Feynman's investigation of vortices in superfluids [58] inspired Alexei Abrikosov

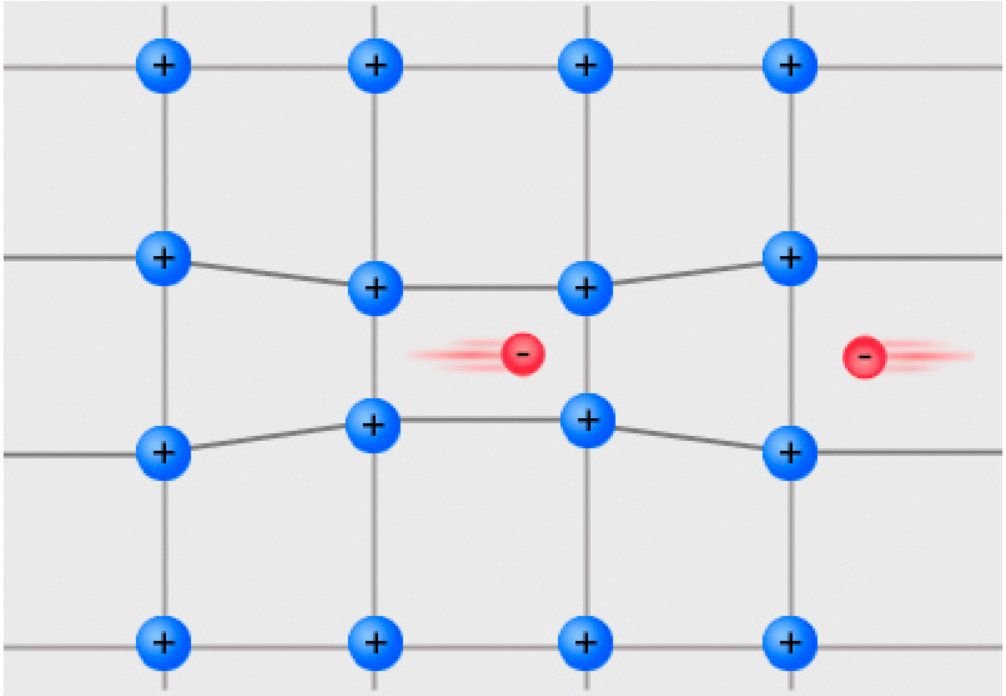

Figure 1.3: Negatively charged electrons (red) forming Cooper pairs via the weak attraction provided by the positively charged distorted-phonon lattice (blue).

to discover, in 1955, that magnetic flux penetration transpires in quantized flux lines, resulting in vortices that arrange themselves in a triangular lattice [59]. This seminal discovery in the field of superconductivity led to Abrikosov being awarded the Nobel Prize in Physics in 2003. In 1950, Herbert Frölich predicted, via theoretical means, that the critical temperature T_c decreases as the proportion of more massive isotopes is increased. This phenomenon is commonly referred to as the "isotope effect" [60] and was experimentally verified by C.A. Reynolds in the same year [61]. The outcomes provided convincing evidence that superconductivity involves an electron-phonon interaction.

The next significant advancement in the theory of superconductivity was made by John Bardeen, Leon Cooper, and Robert Schrieffer with the development of the BCS theory in 1957 [62]. The trio was later awarded the Nobel Prize in Physics in 1972 for their groundbreaking quantum mechanical explanation of superconductivity. The BCS theory posits a Fermi electron sea that is coupled to a lattice of phonons via a feeble attraction (see figure 1.3), which results in the formation of Cooper pairs, the superconducting charge carriers. In 1956, L. Cooper showed that Fermi electrons become unstable when subjected to a weak attractive force, which leads to the formation of pairs of two electrons [63]. The BCS theory utilizes quantum mechanics to describe superconductivity, where Cooper pairs (effectual Bosons) occupy the ground state and are separated by an energy gap in the energy spectrum from low energy excited states.

In 1959, Lev Gor'kov, a protégé of Landau, demonstrated that the BCS theory reduces to the Ginzburg-Landau formalism at temperatures close to T_c, establishing a link between the phenomenological and microscopic approaches [64]. In 1962, Brian Josephson discovered the phenomenon of Cooper pair quantum tunnelling, where Cooper pairs tunnel across the barrier between two superconducting materials, which became known as the "Josephson effect" [65]. For his contribution to tunnelling phenomena in superconductors, he was awarded the Nobel Prize in 1973. Although the highly-regarded BCS theory theoretically predicted a critical temperature limit of approximately 35K, the discovery of a new type of superconducting material led to a breakthrough in this area.

In 1986, Karl Müller and Johannes Bednorz reported the fabrication of a lanthanum barium copper oxide (LaBaCuO) superconductor with a high critical temperature of 30K [66], marking the discovery of a new class of high-temperature superconductors. The initial publication was met with scepticism until the results were independently reproduced by a Japanese group in 1987 [67] and a Chinese group in the same year [68]. This breakthrough ignited a revolution in the field of high-temperature superconductivity, with a plethora of new materials exhibiting higher T_c values being discovered at an unprecedented rate. Notably, a lanthanum compound with a T_c close to 40K was discovered under normal conditions in 1987 [69], and 52K under high pressure [70]. Soon after, an yttrium-barium superconducting compound was discovered with a T_c of 93K, followed by the discovery of BiSrCaCuO with a remarkable T_c of 110K [71]. Further details on the various superconducting materials will be covered in the subsequent section.

1.2 Theoretical descriptions of superconductivity

In this section, we will delve into the phenomenological theories that have been developed to explain some of the observed features of superconductivity. The first theory was put forth by Fritz and Heinz London in 1935, known as the London theory of superconductivity. The London equations provide a relationship between the superconducting current and the electromagnetic fields acting in the system. While Ohm's law is the most basic relation in typical conductors, the London equations serve as the superconducting analog. This theory explains the Meissner effect and the relation between supercurrent density $\mathbf{J}$ and voltage U, which are not considered in the theory of normal metals/conductors.

Next, we will introduce the phenomenological Ginzburg-Landau (GL) theory, which is fundamental to the work performed in this thesis. In 1950, Vitaly Ginzburg and Lev Landau presented their theory of superconductivity, taking a non-local mean-field approach. The GL theory considers the electronic phase transition from normal to superconducting as a second-order phase transition, where a complex function Ψ represents the order parameter.

1.2.1 London model

In the London model, we begin with the consideration of the electric field $\mathbf{E}$ and magnetic field $\mathbf{B}$ to explain the superconducting currents without any dissipation, such that $\frac{\delta \mathbf{B}}{\delta t} = 0$, and the expulsion of magnetic field from the interior of the superconductor, such that $\mathbf{B} = 0$. These conditions are represented by the following equations:

$$\mathbf{E} = \frac{\delta}{\delta t}\left(\frac{m^*}{cn_s e^{*2}}\mathbf{J}_s\right), \tag{1.1}$$

$$\mathbf{B} = -\nabla \times \left(\frac{4\pi m^*}{n_s e^{*2}}\mathbf{J}_s\right), \tag{1.2}$$

where m^*, e^*, and n_s are the effective electron mass, effective charge and density of Cooper pairs respectively.

Equation 1.1 describes the characteristic feature of perfect conductivity in superconductors, showing that any electric field applied to the material will accelerate the superconducting electrons, which differs from Ohm's law in normal conductors, where the electron velocity is constant. This equation describes perfect superconductivity in the presence of any stationary field. However, to account for the Meissner effect, which is the expulsion of the magnetic field from the interior of the superconductor, we need to impose a restriction on the magnetic field such that $\mathbf{B} = 0$. This condition is accounted for by the second London equation, as given by equation 1.2. Starting from the principles of Ampere's law ($\nabla \times \mathbf{B} = \mu_0 \mathbf{J}$) and flux conservation ($\nabla \cdot \mathbf{B} = 0$), we can combine them with equation 1.2 of the London model to derive a differential equation that describes the penetration of the magnetic field into the superconductor. The resulting equation is given as

$$\nabla^2 \mathbf{B} = \frac{\mathbf{B}}{\lambda^2}, \tag{1.3}$$

where λ is known as the London penetration depth. This equation shows that the magnetic field decays exponentially from the surface towards the interior of the material over a length scale given by the penetration depth. The London penetration depth itself is determined by the effective electron mass, the density of Cooper pairs, and the effective charge and is expressed as

$$\lambda = \sqrt{\frac{m^*}{\mu_0 n_s e^{*2}}}. \tag{1.4}$$

The Meissner effect is primarily governed by the combination of equations 1.3 and 1.4. To express equations 1.1 and 1.2 more concisely, we can use the vector potential $\mathbf{A}$, as suggested by Fritz London:

$$\mathbf{J}_s = -\frac{cn_s e^{*2}}{4\pi m^*}\mathbf{A}. \tag{1.5}$$

However, this expression is not gauge invariant and must be accompanied by the London gauge condition $\nabla \cdot \mathbf{A} = 0$. This theory was the first attempt at describing the newly discovered phenomenon, although it lacked microscopic description. Nonetheless, it accurately describes the behavior of dirty superconductors with a short mean free path l. Moreover, this theory predicted the quantization of magnetic flux inside the superconductor, which was crucial in later understanding the existence of point-like objects in the form of quantized flux lines in type-II superconducting materials.

1.2.2 Ginzburg-Landau

The Ginzburg-Landau theory employs a powerful tool in the form of a complex-valued quasi-classical wave function Ψ to act as the order parameter, which describes the phase transition from the normal state ($\Psi = 0$) to the superconducting state ($\Psi \neq 0$) when there is no external magnetic field $\mathbf{H}$ [57]. The density of superconducting electrons is related to the magnitude of the complex order parameter by $|\Psi(\mathbf{r})|^2 = n_s/2$. Ginzburg and Landau constructed a free energy functional based on the theory of second-order phase transitions developed by Landau and Lifshitz, expressed in terms of the complex order parameter Ψ. One consequence of employing a theory of phase transitions, such as the Ginzburg-Landau theory, is that its validity is limited to the vicinity of the phase transition point, which is commonly defined as the critical temperature T_c. When an external magnetic field H is applied, the Gibbs free energy density functional proposed by Ginzburg and Landau takes the following form [72, 73]:

$$G_s = G_n + \alpha|\Psi|^2 + \frac{\beta}{2}|\Psi|^4 + \frac{1}{2m^*}\left|(-i\hbar\nabla - \frac{2e^*}{c}\mathbf{A})\Psi\right|^2 - \frac{(\mathbf{h}+\mathbf{H})^2}{8\pi}, \tag{1.6}$$

where G_s and G_N represent the free energy densities of the superconducting and normal states, respectively. The effective mass of Cooper pairs is denoted by $m^* = 2m$, and $\mathbf{h}$ represents the local magnetic field. The first two terms of the expression account for the energy cost of a nonzero order parameter and its density, respectively, while the third term represents the self-interaction of the order parameter. The fourth term is the kinetic energy of the Cooper pairs, while the final term represents the energy cost of the magnetic field that interacts with the superconducting material. The material parameters α and β are closely related to the critical temperature T_c. Specifically, α is proportional to $T - T_c$ and approaches zero as T approaches T_c, while β has a constant value β_0 that is always positive. Below T_c, α becomes negative. When we minimize the free energy density functional in Equation 1.6 with respect to the order parameter Ψ and the vector potential $\mathbf{A}$, we obtain a system of coupled nonlinear differential equations [73]:

$$\alpha\Psi + \beta|\Psi|^2\Psi + \frac{1}{2m^*}\left(-i\hbar\nabla - \frac{2e^*}{c}\mathbf{A}\right)^2\Psi = 0, \tag{1.7}$$

$$\mathbf{J} = \frac{ihe^*}{m^*}(\Psi^*\nabla\Psi - \Psi\nabla\Psi^*) - \frac{4e^{*2}}{m^*c}|\Psi|^2\mathbf{A}, \tag{1.8}$$

where the current density $\mathbf{J}$ can be expressed as

$$\mathbf{J} = \frac{c}{4\pi}\nabla \times \nabla \times \mathbf{A}. \tag{1.9}$$

Using the aforementioned equations, one can calculate the spatial distribution of the order parameter and current densities. Notably, Equation 1.7 describing the order parameter distribution has a similar form to the Schrödinger equation for a particle with mass $2m$, charge $2e$, energy $-\alpha$, and wavefunction $\Psi(\mathbf{r})$ in a potential $\beta|\Psi|^2$. The temperature dependence of α and β is derived from the theory of second-order phase transitions. It is proposed that the parameters α and β have the following temperature dependencies [74]:

$$\alpha(T) = -\alpha_0 \frac{T_c^2 - T^2}{T_c^2 + T^2}, \tag{1.10}$$

$$\beta(T) = \beta_0 \frac{T_c^4}{(T_c^2 + T^2)^2}. \tag{1.11}$$

As the temperature approaches the critical temperature ($T \longrightarrow T_c$), equations 1.10 and 1.11 assume the form $\alpha(T) \simeq -\alpha_0(1 - \frac{T}{T_c})$ and $\beta(T) \propto \beta_0$, respectively. These functions were obtained by Ginzburg and Landau through an expansion of the free energy functional.

As discussed in a subsequent section, the Ginzburg-Landau equations can be derived using a variational method. These equations serve as the foundation for constructing a time-dependent Ginzburg-Landau theory, which is the primary tool used for obtaining results from numerical simulations of superconducting nanostripe structures. This theory is exceptionally versatile, as it is rooted in second-order phase transitions and can be adapted to a wide range of physical systems. One such system is magnetism, where the magnetic susceptibility, which exhibits a discontinuous change, is the second-order derivative of the free energy with respect to the magnetic field.

1.2.3 Microscopic BCS theory

In 1957, Bardeen, Cooper and Schrieffer proposed the BCS theory, which is a successful quantum mechanical description of superconductivity [62]. This theory employs second order quantization using mean field theory to solve a many-body problem by considering the coupling between electrons and the ionic lattice, which results in the formation of Cooper pairs [63]. The BCS equations yield the ground-state properties of the superconducting condensate, and predict the existence of a superconducting energy gap that separates the superconducting ground state from the excited normal states. Remarkably, the energy gap and critical temperature are related by the universal expression $\Delta(T = 0) = 1.764\ k_B T_c$, where k_B is the Boltzmann constant. The BCS theory aimed to elucidate how normal electrons with energies just above the Fermi energy can form pairs in the presence of a weak attractive potential. When negatively charged electrons pass over the positively charged ionic lattice, the lattice is momentarily distorted, leading to a concentration of positive charge that acts as an attractive potential on the electrons, causing them to form Cooper pairs. These pairs are effective Bosons and have the property that an "infinite" number of them can occupy the same energy state. This leads to a condensation of the Cooper pairs to the ground state, which is energetically favorable. For the formation of electron pairs, the physical criteria require that the pair's energy be above the Fermi energy E_F, their momentum must be equal and opposite, and their spins must be opposite. When these criteria are met, and there is an attractive potential, the sea of electrons will correlate, and Cooper pairs will form, leading to superconductivity. The interaction of electrons with the ionic lattice is fundamental to conventional superconductivity, where the attractive interaction occurs between electrons and phonons in the lattice. When two electrons satisfy the pairing criteria, their velocities exceed the lattice vibrations. As they move through the lattice, they cause a temporary polarization where positive charge accumulates. The polarization relaxation times are much longer than the time it takes for another electron to be caught in the wake of the first one, forming a Cooper pair. The pair's spatial correlation extends over the microscopic coherence length ξ_0. Using this explanation for the formation of a Cooper pair, a many-body system of electrons was considered, applying the mean-field approximation for a homogeneous superconductor. Bardeen, Cooper, and Schrieffer demonstrated how fermionic electrons condense into a bosonic state with zero total spin, stabilized by the emergence of a superconducting energy gap. The presence of such a gap eliminates scattering between superconducting electrons and the metallic lattice, resulting in dissipationless transport currents (super-currents).

In the pursuit of understanding superconductivity, Lev Gor'kov demonstrated the equivalence of the Ginzburg-Landau order parameter to the quantum mechanical single wave function Ψ [64]. Gor'kov utilized the mapping of BCS microscopic theory to the Ginzburg-Landau theory and derived an analogous equation. In the London temperature range near T_c, the vector potential $\mathbf{A}(\mathbf{r})$ and superconducting energy gap $\Delta(\mathbf{r})$ vary slowly over distances larger than the coherence length Λ, and thus the equations can be linearised. The Ginzburg-Landau equations are obtained by introducing a wave function proportional to $\Delta(\mathbf{r})$. Gor'kov's equations, derived from thermodynamic Green's functions, show the relationship between the current density $\mathbf{j}$, the order parameter $\Psi(\mathbf{r})$, and the vector potential $\mathbf{A}(\mathbf{r})$. The equations, as presented in the original paper, are

$$\left\{\frac{1}{2m^*}\left(\nabla - ie^*\mathbf{A}(\mathbf{r})\right)^2 + \frac{1}{\lambda}\left[\frac{T_c - T}{T_c} - \frac{2}{N}\left|\Psi(\mathbf{r})\right|^2\right]\right\}\Psi(\mathbf{r}) = 0 \tag{1.12}$$

$$\mathbf{j}(\mathbf{r}) = -\frac{ie^*}{2m^*}\left(\Psi^*\nabla\Psi - \Psi\nabla\Psi^*\right) - \frac{e^{*2}}{m^*c}\mathbf{A}\left|\Psi\right|^2. \tag{1.13}$$

Indeed, the relationship between the Ginzburg-Landau and BCS theories is crucial because the microscopic theory of superconductivity provides the most accurate description of conventional superconductivity based on the principles of quantum mechanics. As shown by Gor'kov, in the regime close to the critical temperature, the mapping of BCS microscopic theory to the Ginzburg-Landau theory is valid, and the GL-equations arise under these conditions. Therefore, the Ginzburg-Landau theory can be considered as a macroscopic theory that captures the essential features of superconductivity, while the BCS theory provides a microscopic picture of the underlying physics.

1.3 The two types of superconductors

To deepen our comprehension of the distinctions between various superconductors, we must scrutinize their response to magnetic fields from external sources. Type-I and type-II superconductors display contrasting behavior as a result of differences in their surface energies at the boundary between the superconducting and normal states, which can be evaluated utilizing the GL parameter $\kappa = \lambda/\xi$ [59]. Here, λ refers to the magnetic penetration depth, and ξ indicates the superconducting coherence length.

When κ is less than $1/\sqrt{2}$, we classify the superconductor as type-I. In contrast, when κ exceeds $1/\sqrt{2}$, we identify the superconductor as type-II. These two categories of superconductors exhibit distinct magnetic field behaviors due to differences in their surface energies at the boundary between the superconducting and normal states.

A type-II superconductor possesses a negative surface energy that favors the establishment of superconducting-normal boundaries with flux penetration in the form of vortices carrying a solitary superconducting flux quantum $\Phi_0 = h/2e = 2.07 \cdot 10^{-15}\mathrm{Tm}^2$. On the other hand, a type-I superconductor, in the bulk limit, demonstrates the Meissner effect up to a critical thermodynamic field $H_c(T)$, expressed as $H_c(T) = \Phi_0/2\sqrt{2}\lambda(T)\xi(T)$. This is a state of perfect diamagnetism, in which all magnetic fields are expelled from the interior of the superconducting material up to $H_c(T)$. If stronger magnetic fields are applied, they will eliminate superconductivity, and the system will transition to a normal state.

Alternatively, type-II superconductors exhibit perfect diamagnetism up to a first critical field, H_{c1}, which is given as $H_{c1}(T) = [\Phi_0/4\pi\lambda^2(T)]\ln\kappa$. As we increase the external magnetic field H beyond the lower critical field H_{c1} but below the upper critical field H_{c2}, vortices start to penetrate the superconductor leading to a mixed state. However, when H reaches the upper critical field H_{c2}, the cores of individual vortices overlap, making it impossible to distinguish them. Mathematically, we express this critical field as $H_{c2}(T) = \frac{\Phi_0}{2\pi\xi(T)^2}$, where $\xi(T)$ represents the superconducting coherence length at temperature T.

At even higher magnetic fields, beyond H_{c2} but below the third critical field H_{c3}, superconductivity exists only at the thin edge of the sample of thickness $\xi(T)$, and the interior of the sample is in the normal state. For a type-II bulk superconductor with a perpendicular magnetic field, the third critical field H_{c3} is roughly 1.69 times the value of the upper critical field H_{c2} [72].

We can distinguish between different states of a superconductor by its magnetization, which is given by $\mathbf{M} = \frac{\mathbf{B}-\mathbf{H}}{4\pi}$, where $\mathbf{B}$ is the magnetic inductance averaged over the entire sample. In the Meissner state, where all magnetic flux is expelled, i.e., $B = 0$, the magnetization is $M = -H/4\pi$. In the mixed state, where $H > H_{c1}$, increasing the magnetic field results in a smooth decrease of the absolute value of magnetization $|M|$ until it reaches zero at H_{c2}.

1.4 Vortices in type-II superconductors

1.4.1 Magnetic flux quantisation

From the second GL equation (equation 1.8), we can derive the quantisation condition for magnetic flux. This equation is given by

$$\mathbf{J} = \frac{e^*\hbar}{m^*}|\Psi|^2\nabla\theta - \frac{2e^{*2}}{m^*c}|\Psi|^2\mathbf{A}, \tag{1.14}$$

where θ is the phase in $\Psi = |\Psi|e^{i\theta}$. Taking the line integral of this equation around a closed line, we obtain

$$\oint \mathbf{J} \cdot d\mathbf{l} = \frac{e^*}{m^*}|\Psi|^2 \oint (\hbar\nabla\theta - \frac{e^*}{c}\mathbf{A}) \cdot d\mathbf{l}. \tag{1.15}$$

Using Stoke's theorem and the definition of the vector potential $\mathbf{A}$, $\oint \mathbf{A} \cdot d\mathbf{l} = \int (\nabla \times \mathbf{A}) \cdot d\mathbf{S} = \int \mathbf{h} \cdot d\mathbf{S} = \Phi$, we obtain the expression

$$\frac{m^*c}{2e^{*2}|\Psi|^2} \oint \mathbf{J} \cdot d\mathbf{l} + \frac{e^*}{c}\Phi = \oint \hbar\nabla\theta \cdot d\mathbf{l}. \tag{1.16}$$

Since the complex superconducting order parameter is single-valued, it requires that the phase must change by integer multiples of 2π in a closed circuit. This leads to the expression

$$\frac{m^*c}{2e^{*2}|\Psi|^2} \oint \mathbf{J} \cdot d\mathbf{l} + \Phi = n\frac{hc}{e^*} = n\Phi_0, \tag{1.17}$$

which states that the sum of the enclosed flux Φ and the line integral of $\mathbf{J}$ is quantized.

1.4.2 Isolated and interacting vortices

Isolated vortices

If we apply an external magnetic field H greater than the first critical field H_{c1} to a type-II superconductor, we will observe the penetration of vortices into the sample. These vortices are individual flux tubes that possess a normal-state core having a radius of ξ within which the superconducting order parameter reduces to zero. The local magnetic field $h(\mathbf{r})$ is maximum at the center of the vortex and decreases over a distance of λ due to the induced supercurrents that screen the magnetic field. When the spacing between vortices is larger than λ, they do not overlap or interact, and each vortex can be treated as an isolated entity. In the extreme type-II superconductors, where the parameter $\kappa = \lambda/\xi \gg 1$, the order parameter can be considered constant except within the vortex core. As a result, for $r > \xi$, the distribution of the order parameters and currents can be calculated using the simplified London equations. Within the framework of the London equations, to account for the normal core fluxoid from equation 1.17, the London equation (1.2) takes the form

$$\frac{4\pi\lambda^2}{c}\nabla \times \mathbf{J} + \mathbf{h} = \mathbf{z}\Phi_0\delta(r), \tag{1.18}$$

where $\mathbf{z}$ is a unit vector along the vortex line, and $\delta(r)$ is a δ-function in the center of the vortex core. By combining Maxwell's equation $\nabla \times \mathbf{h} = 4\pi/c\mathbf{J}$ with equation 1.18, we can obtain the expression

$$\lambda^2\nabla^2\mathbf{h} + \mathbf{h} = \mathbf{z}\Phi_0\delta(r), \tag{1.19}$$

which has an exact solution that describes the local magnetic field as a function of radial distance from the core:

$$h(r) = \frac{\Phi_0}{2\pi\lambda^2} K_0(r/\lambda), \tag{1.20}$$

where K_0 is the zero-order Bessel function. The derivative of equation 1.20 provides the local current flowing around the vortex core, which can be expressed as

$$J(r) = \frac{c\Phi_0}{4\pi^2\lambda^2} K_1(r/\lambda), \tag{1.21}$$

where K_1 is the first-order Bessel function. The current diverges with a $1/r$ dependence and decreases exponentially at large distances.

The free energy per unit length of a vortex can be calculated by accounting for the contributions from the field and kinetic energy of the currents. The resulting expression is

$$\epsilon = \left(\frac{\Phi_0}{4\pi\lambda}\right)^2 (\ln(\lambda/\xi) + \epsilon_0), \tag{1.22}$$

where $\epsilon_0 = 0.12$ is the small contribution originating from the vortex core. This equation is a quadratic function of Φ_0, and therefore, it is energetically favorable to form single quantized vortices as opposed to multi-quanta vortices.

Interacting vortices

In the high-kappa limit, we can analyze the interaction between two vortices in the following manner. Consider two parallel flux lines positioned at r_1 and r_2, respectively. The total magnetic field can be expressed as a sum of the magnetic fields from vortex (1) and (2), $\mathbf{h} = \mathbf{h}_1 + \mathbf{h}_2$, and is given by the following differential equation:

$$\lambda^2\nabla^2\mathbf{h} + \mathbf{h} = \mathbf{z}\Phi_0 \left[\delta(\mathbf{r} - \mathbf{r}_1) + (\mathbf{r} - \mathbf{r}_2)\right], \tag{1.23}$$

where λ represents the magnetic penetration depth, $\mathbf{z}$ is a unit vector perpendicular to the plane of the vortices, and Φ_0 is the magnetic flux quantum. The resulting increase in free energy per unit length is expressed as:

$$F_{12} = \frac{\Phi_0 h_1(r_2)}{4\pi} = \left(\frac{\Phi_0^2}{8\pi^2\lambda^2}\right) K_0\left(\frac{r_1 - r_2}{\lambda}\right), \tag{1.24}$$

where K_0 is the modified Bessel function of the second kind. The change in energy due to the interaction between the vortices is given by:

$$\Delta F = \frac{\Phi_0}{8\pi}\left[h_1(r_1) + h_2(r_2) + h_1(r_2) + h_2(r_1)\right] = \frac{\Phi_0}{4\pi} h_1(r_1) + \frac{\Phi_0}{4\pi} h_1(r_2). \tag{1.25}$$

The interaction between vortices can be either repulsive or attractive depending on the polarity of the magnetic spins. If the spins are the same, the interaction is repulsive; if they

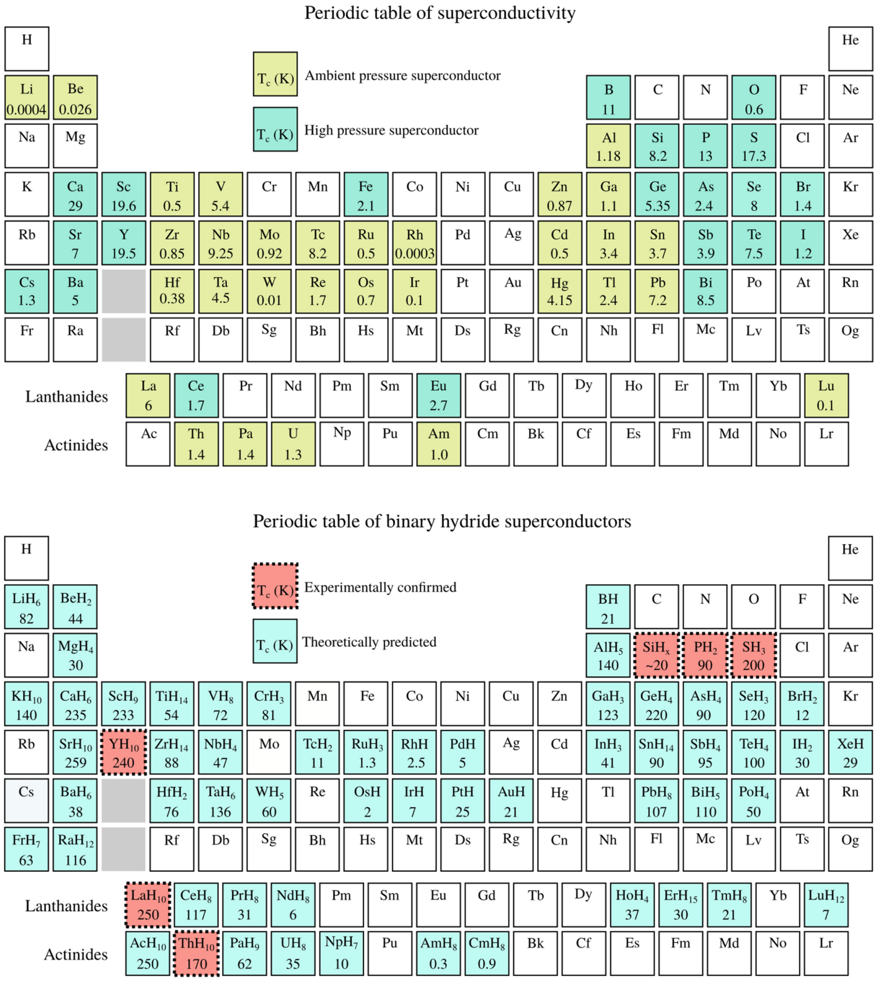

Figure 1.4: Top: Superconducting elemental solids and their corresponding experimental critical temperature (T_c). Bottom: Periodic table of superconducting binary hydrides (0–300 GPa). Theoretical predictions are indicated in blue and experimental results showing in red [75].

are opposite, the interaction is attractive. The force per unit length experienced by a single vortex can be obtained by deriving the interaction energy F_{12} and is given by:

$$f = j \times \frac{\Phi_0}{c}, \tag{1.26}$$

where j is the current density and c is the speed of light. When the vortices are far apart compared to λ, the interaction is weak. However, when the vortices are close (compared to λ), the interaction is significant and can perturb the system.

1.5 Superconducting material summary

The discussion thus far has centered on superconductivity in bulk samples, which are characterized by macroscopic dimensions. However, it is important to note that superconducting properties can vary as the dimensions of the sample are reduced, with the most pronounced effects being observed at the nanoscale. The effective penetration depth or Pearl length, $\Lambda = \lambda^2/d$, depends on the film thickness d, and therefore the effective Ginzburg-Landau parameter, $\kappa_{eff} = \Lambda/\xi$. So a type-I superconducting thin film can undergo a transition to a type-II superconductor when $\kappa_{eff} \geq 1/\sqrt{2}$, leading to a significant alteration in its response to an applied magnetic field.

Despite their excellent conductivity, materials such as copper, gold, and silver are not superconductors. This is due primarily to the deep energetic band structure of these materials, which lacks an energy gap between the ground state and the first excited states necessary for the formation of Cooper pairs.

In contrast, the emergence of superconductivity in conventional elemental superconductors arises from the formation of Cooper pairs due to phonon lattice vibrations, as described by the BCS theory. These superconductors are characterized by s-wave pairing, with zero net spin and momentum. Superconductivity can also arise from different mechanisms and under specific conditions, as noted by Buckel and Kleiner [76].

The discovery of superconductivity has yielded a vast array of materials and compounds, each with unique properties and characteristics. Figure 1.4 provides a periodic table of elements and their corresponding critical temperature, along with any applicable high pressure requirements. Additionally, the figure depicts an elemental table of binary hydride superconductors, highlighting the chemical formula and the required number of hydrogen atoms for each hydride.

Figure 1.5 offers a timeline of the discovery of superconducting materials, beginning with the discovery of elemental metals such as mercury, lead, and niobium in the early 1900s [52, 77]. The discovery of superconducting alloys followed in the mid-twentieth century, with the discovery of heavy fermionic superconductors in the early 1980s [78], high temperature cuprates in 1987 [66], and superconducting Buckminsterfullerenes in the early 1990s [79]. Carbon allotropes, such as carbon nanotubes, were discovered in the early 2000s and exhibited superconductivity [80]. In 2006, iron-pnictides were discovered, with some displaying high critical temperatures (T_c) [81]. Notably, binary hydrides under high pressure currently hold the record for the highest critical temperatures. However, most recently, hydrogen-sulfide (H_2S) achieved a room temperature superconducting $T_c = 288$K at a pressure of 270GPa, setting a new record for the highest critical temperature to date [82].

While elemental metals were the first materials to exhibit superconductivity, alloys and compounds now comprise the vast majority of known superconducting materials.

Cuprates

The cuprates, a family of high-temperature superconductors, consist of materials with alternating layers of CuO_2 and ions such as lanthanum, barium, yttrium, and strontium

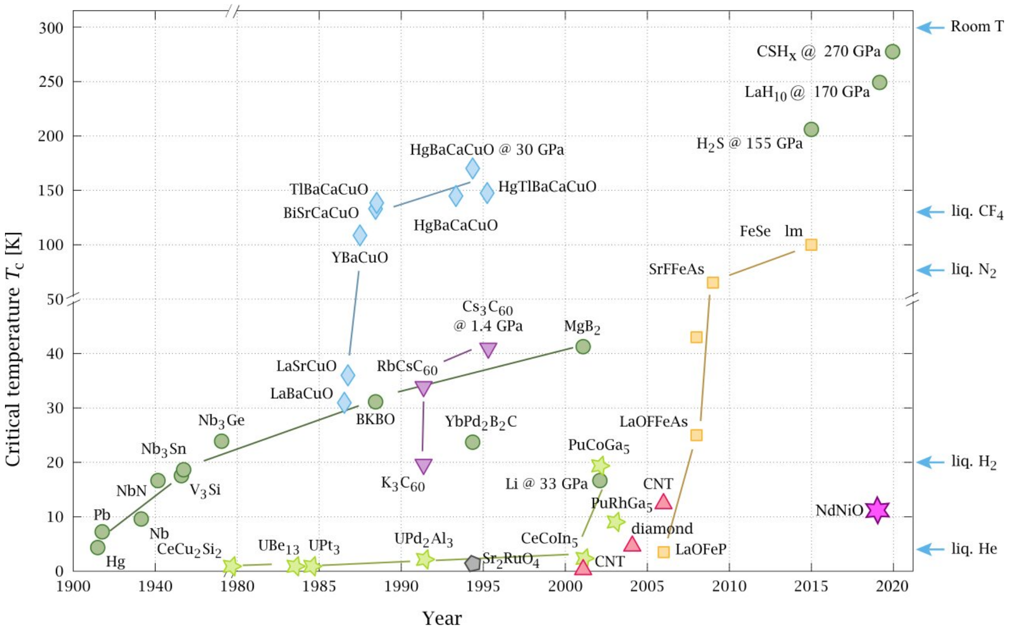

Figure 1.5: Chronology for the discovery of superconducting materials and the corresponding critical temperatures. The different superconducting materials are indicated by: BCS superconductors (green circles), cuprates (blue diamonds), iron pnictides (yellow squares), heavy fermionic (light green star), Buckminsterfullerene (inverted purple triangles), carbon-allotropes (red triangle), nickel-based (pink star) [83].

[66, 84, 85]. These ionic layers serve as charge reservoirs that dope the copper-oxide planes with either electrons or holes, leading to superconductivity only in the CuO_2 planes, and not in the ionic layers. As a result, the superconductivity in cuprates is two-dimensional, with weak coupling between CuO layers. Due to the anisotropy in normal and superconducting properties, there is much higher conductivity parallel to the CuO_2 layer than in the perpendicular direction.

The mechanism behind the superconductivity in cuprates remains unknown and is an active area of research. However, several proposals have been put forward to explain this phenomenon.

Fullerene

Buckminsterfullerenes are fascinating carbon structures that exhibit unique geometric and physical properties. These compounds consist of 60 carbon atoms arranged in a geodesic dome-like structure and are part of a family of carbon structures called fullerenes. The first man-made buckminsterfullerene was synthesized in 1984 by Eric Rohlfing, Donald Cox, and Andrew Kaldor, and since then, these structures have been the subject of intense research due to their ability to trap doping atoms and exhibit superconducting behavior at high temperatures.

Interestingly, the name "Fullerenes" was coined after Buckminster Fuller, who filed a patent for the use of geodesic forms in 1954. However, the first geodesic structures were created by Walther Bauersfeld shortly after World War I. The crystal structure of buckminsterfullerenes allows for the trapping of atoms, which can become fullerides and exhibit superconducting properties at high temperatures. In 1991, the first superconducting fulleride, K_3C_{60}, was discovered, ushering in a new era of research into these fascinating carbon structures.

Iron pnictides

Iron-based superconductors (IBSCs) are a fascinating class of materials that have captured the attention of researchers since their discovery in 2006 [81]. These compounds consist of layers of iron bonded to a pnictide, separated by layers of a lanthanide. The similarity in structure to the cuprate superconductors has led to comparisons between the two, as well as to the suggestion that the pairing mechanism in IBSCs may also be unconventional.

One of the key features of IBSCs is their high critical temperature, which is the temperature below which they exhibit superconductivity. This property is strongly influenced by the amount of electron or hole doping present in the material [81, 86]. Another advantage of IBSCs is their resistance to impurities and grain boundaries, which can cause problems in other types of superconductors. In addition, they display very high critical magnetic fields, making them suitable for use in applications that require high magnetic fields, such as magnetic resonance imaging (MRI) machines [87].

IBSCs have been used in various superconducting applications, with particular success in the production of superconducting wires. Recent research has shown that the critical currents achieved in IBSC wires have reached commercial levels, and in fact, they can exceed these levels in the presence of high magnetic fields [88]. This makes IBSC wires a promising candidate for use in power transmission, magnetic levitation, and other high-current applications.

In summary, IBSCs are a rapidly evolving field with many exciting possibilities for superconducting applications. Ongoing research is needed to fully understand the underlying physics and to further develop these materials for practical use.

Magnesium diboride

Magnesium diboride (MgB_2) is an interesting material that was first synthesized and confirmed in 1954 [89]. However, it was only in 2001 that a Japanese group discovered that MgB_2 exhibits superconductivity [90], and that the superconductivity arises from the BCS mechanism involving electron-phonon interactions. Interestingly, the superconductivity arises due to the mixing of multiple energy bands, which leads to the opening of two different superconducting energy gaps (2 meV and 7.5 meV) on different parts of the Fermi surface making it a two-band superconductor [91]. Although MgB_2 is a type-II superconductor, it exhibits intermediate behavior between type-I and type-II [92], and has a high critical magnetic field of 30 T when doped with carbon [93]. Overall, MgB_2 is a promising material for various superconducting applications, including magnets and wires, due to its relatively high critical temperature (not as high as cuprates) and magnetic field, and unique properties.

Additional superconducting materials

It is important to note that there are many other superconducting materials beyond those discussed above, which are also of great interest. For example, metal hydrogen systems have been shown to exhibit superconductivity with a critical temperature around 10K, and the hydrogen can be replaced with the heavier isotope deuterium [94, 95, 96]. Ceasium-based heavy fermionic superconductors, discovered by Frank Steglich in 1978, exhibit non-conventional superconductivity [78]. Organic superconductors, first realized in 1979, demonstrate critical temperatures between 0.5-10K, and the mechanism for condensation is not yet fully understood [97, 98, 99].

Moreover, superconductivity has also been theorized to exist in astronomical objects such as neutron stars, with rapid cooling being attributed to possible superconductivity [100]. Black holes have also been suggested to have a superconducting region, where simple gravitational theory provides a holographic dual description of a superconductor [101, 102, 103].

In the field of nanoscale applications, state-of-the-art superconducting electronics are commonly fabricated from materials such as Nb, NbN, NbTiN, TiN, Al, and MoRe. While other alloys have shown promising results, they require rigorous processing techniques to produce, such as $YBa_2Cu_3O_{7-x}$ [104].

Thanks to the diversity of superconducting materials with unique and useful properties, many applications of superconductivity have been developed or proposed. These applications will be discussed in the following section.

1.6 Superconducting applications and fabrication

Indeed, the use of superconductivity in magnet-related applications has greatly advanced technological advancements in several fields. The maglev trains mentioned use superconducting electromagnets generating their magnetic field through the Meissner effect, where a superconductor expels magnetic flux from its interior, creating a magnetic field above it, which levitates the train. By eliminating friction between the train and the tracks, the maglev trains have achieved unparalleled speeds of $600\mathrm{km\,h^{-1}}$, providing an energy-efficient and high-speed transport option [105].

Superconducting magnets are used in MRI machines to generate a strong, uniform magnetic field that interacts with the magnetic moments of atomic nuclei in the human body. By manipulating this magnetic field using gradient coils and radiofrequency pulses, MRI machines can produce detailed images of the body's internal structures with exceptional clarity and resolution. The use of superconducting magnets in MRI has greatly improved the quality and speed of medical imaging, allowing for earlier and more accurate diagnosis of a wide range of conditions.

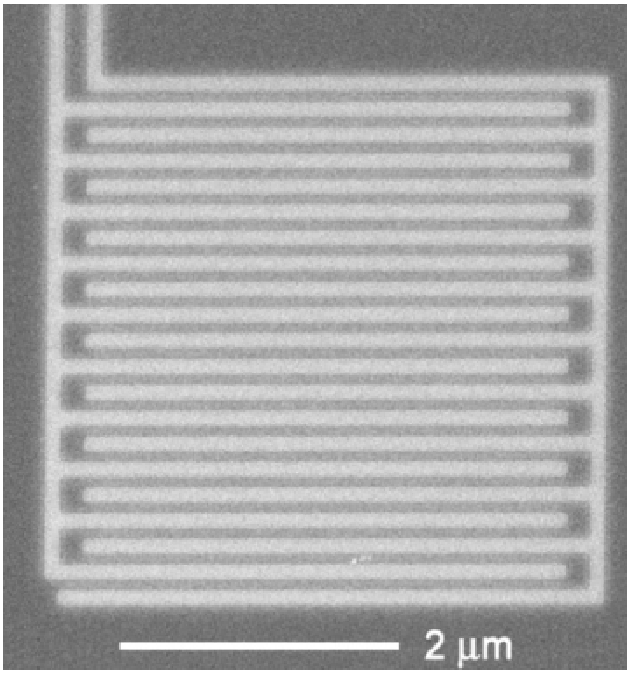

Figure 1.6: Scanning electron microscopy of a niobium SNSPD of area 16 µm^2. The dark area is the niobium and the white area is a sapphire substrate [109].

Similarly, in NMR machines, superconducting magnets are used to generate a strong, stable magnetic field that allows for the precise measurement of the magnetic properties of molecules and materials. This technique is widely used in chemistry, physics, and materials science for studying the structure and properties of materials at the atomic scale. The use of superconducting magnets in NMR has enabled researchers to make breakthrough discoveries in fields such as drug development, materials science, and protein structure determination.

Overall, the integration of superconducting magnets in medical and scientific instruments has led to significant advancements in both fields, allowing researchers and medical professionals to study and diagnose complex systems with greater precision and accuracy, and for the development of treatments [106, 107, 108]. Superconducting magnets play a crucial role in the operation of particle accelerators like the Large Hadron Collider (LHC) at CERN, as well as in magnetic confinement in nuclear fusion reactors such as tokamaks [110]. These magnets are essential for beam steering and stability, and their superconducting properties enable them to produce strong and stable magnetic fields. Similarly, rail guns use superconducting coils to generate strong electromagnetic forces that can propel projectiles at speeds of up to 3km s^{-1} [111].

Superconducting wires, both macroscopic and microscopic, are commonly used to transmit electrical energy with minimal power loss [112, 113]. However, even high temperature superconductors, such as iron pnictides, are limited to utilization at temperatures significantly lower than room temperature. The development of a superconducting material that can operate at or above room temperature would represent a significant breakthrough, as it would allow for the transmission of electrical energy through the power grid with minimal energy lost due to Joule heating. This is an area of ongoing research and development, and many scientists and engineers are working towards the realization of this goal.

The most sensitive magnetometers to date are superconducting quantum interference devices (SQUIDs), which were first invented in 1964 [114] shortly after the fabrication of a Josephson junction [115, 65]. SQUIDs are capable of achieving field resolutions as high as 10^{-17}T [116], and since their invention, significant progress has been made in reducing flux noise. This progress has been made possible through the miniaturization of SQUIDs to micrometer and even nanometer scale, thanks to improvements in thin film fabrication techniques [117].

Superconductivity has also been instrumental in the development of quantum computation, with the invention of superconducting qubits. In 2015, a group successfully implemented a fully controllable 1D array of 9 qubits [118], and in 2019, Google demonstrated for the first time quantum supremacy (i.e., solving non-classical problems in feasible times) using a chip with 53 qubits [119]. There are three basic superconducting qubit archetypes: phase qubits, charge qubits, and flux qubits [120]. Each of these qubits relies on a Josephson junction with energy E_J but is used for different purposes. For example, flux qubits are used in d-wave quantum annealers that solve optimization problems based on an Ising Hamiltonian [121].

Superconductivity continues to be a hot topic of research, offering a system that can be manipulated for exotic applications like gravimeters [122, 123], and constantly evolving in search of new and improved applications.

Superconducting electronic components must be fabricated on scales comparable to the coherence length, ξ, and the penetration depth, λ, which presents challenges during fabrication. Nano-fabrication methods are required to exploit the advantages of ultra-thin superconducting structures, such as kinetic inductance, which is important for single photon detectors, and the isolation of single quantum magnetic flux, which is integral for superconducting qubits.

Various fabrication methods are used to realize superconducting structures, including photolithography [124], electron beam lithography [125], and focused ion beam lithography [126], which often employs direct writing techniques [127, 49, 128]. However, even with state-of-the-art techniques, the final devices are still subject to surface and edge defects that can introduce undesired effects and behaviors in the system. Therefore, it is desirable to improve the aforementioned processes or propose new methods to make such devices commercially viable, where the desired behavior is reproducible.

In conclusion, nano-fabrication methods are necessary to exploit the advantages of ultra-thin superconducting structures, but even with state-of-the-art techniques, surface and edge defects can introduce undesired effects and behaviors in the system. It is therefore desirable to improve existing processes or propose new methods to make such devices commercially viable, where the desired behavior is reproducible.

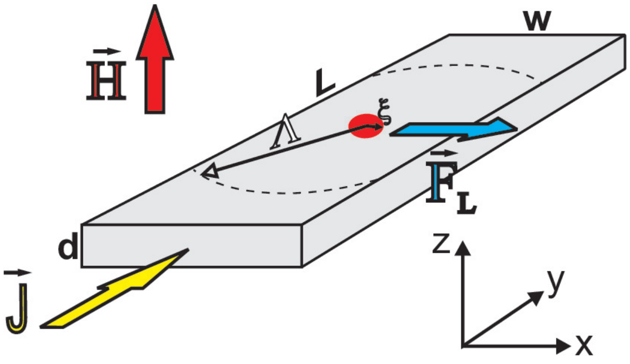

Figure 1.7: Schematic illustration of a superconducting nanostripe having width w, length L and thickness d, along the x, y and z directions, respectively, in a homogeneous out-of-plane applied magnetic field $\mathbf{H}$. The stripe contains an example of a single vortex, with a normal core of radius $\sim \xi$, and distribution of magnetic field around it characterized by $\Lambda = \lambda^2/d$. When an applied current density $\mathbf{J}$ is present the vortex will experience Lorentz-type force $\mathbf{F}_L$.

1.7 Superconducting nanostripes

This thesis focuses on characterizing and identifying superconducting phenomena occurring in thin and narrow superconducting nanostripes. An example of a superconducting nanostripe can be seen in Figure 1.7, with a length L, width w, and thickness d. When a magnetic field H is applied perpendicular to the stripe and its magnitude is sufficient, magnetic flux can penetrate the stripe in the form of a vortex with a normal core of radius ξ and a magnetic field penetration depth of λ. The minium magnetic field required to penetrate the nanostripe with a single magnetic flux quanta must be greater than the lower critical field ($H > H_{C1}$), and also sufficient enough to overcome the strongly confining edge barriers. Superconducting nanostripes are fundamental components in many microscopic superconducting electronics, such as SQUIDs, superconducting kinetic inductance detectors [129], superconducting nanowire single photon detectors (SNSPDs) [130, 3, 1], bolometers [7], and electromagnetic emitters in gigahertz and terahertz regimes [42, 43].

Some of these technologies capitalize on the dissipative state, specifically the phenomena of vortex crossings, such as EM emitters. Other technologies utilize the presence of such vortices. For example, Hall-bar shaped nanostripes could be used for information technology purposes, where vortices carry the relevant information [10].

A SNSPD (superconducting nanowire single photon detector) is a device that typically consists of a long, meandering superconducting nanowire designed to increase the detection efficiency by covering a larger surface area. An example of a SNSPD is shown in Figure 1.6. The geometry of a SNSPD is similar to that of a nanowire, but with corners where the current density is different from that in the main body of the nanostripe [131, 132].

At the nanoscale, the fabrication of such small devices requires special techniques [133, 134], such as focused ion beam lithography [135, 126], or the use of self-assembled "diblock co-polymer" templates [136]. These techniques allow for precise control over the dimensions of the device, which is crucial for achieving the desired properties and performance.

To properly understand the behavior of superconducting nanostripes with small widths, it is important to consider the impact of defects and inhomogeneities in the material. When the defects are smaller than the coherence length, the material is in the "dirty" limit where the inelastic relaxation length is smaller than the coherence length. The inelastic scattering length is defined as $L_{in} = \sqrt{D\tau_{in}}$, where D is the diffusion constant and τ_{in} is the relaxation time of the non-equilibrium quasi particles due to inelastic electron-phonon or electron-electron interactions. This length determines the scale over which the superconducting condensate behaves viscously, and is smaller than the coherence length in the "dirty" limit, where the material contains small defects that are smaller than the coherence length. The aforementioned viscosity introduced as a result affects the behavior of vortices crossing the stripe in the dissipative state compared to a clean material [45]. In addition, defects at the edges or a reduction in lateral dimensions lead to an increase in current density, causing changes in the way vortices cross the stripe compared to a uniform geometry [47, 137, 138].

In the presence of an applied magnetic field and current, there are several interactions to consider, including vortex-vortex, edge barrier, and Lorentz force interactions. These interactions can lead to different dynamic states that may or may not be desirable for various applications. For example, the presence of vortices and their crossings is exploited in some technologies, such as electromagnetic emitters and Hall-bar shaped nanostripes for information technology purposes where vortices carry the relevant information [10].

To understand the effects of confinement forces on the dynamic state of superconducting nanostripes with small widths, this thesis will employ numerical simulations. These simulations will provide insight into how the small width of the nanostripe impacts the behavior of vortices and other dynamic phenomena, which is important for the design and optimization of superconducting nanostripes for various applications.

Chapter 2

The Generalised Time-Dependent and Stationary Ginzburg-Landau Framework

2.1 The generalised time-dependent Ginzburg-Landau (gTDGL) framework

This chapter is devoted to the generalized time-dependent Ginzburg-Landau (gTDGL) model of superconductivity. One of the notable advantages of utilizing this time-dependent model is its capability to elucidate the dynamic behavior and relaxation processes in dirty-thin superconductors. The phenomenological gTDGL framework can be derived from the thermodynamic Gibbs free energy functional, which will be explicated in this chapter. This theory serves as the cornerstone of this thesis and has been implemented by the author to acquire the presented results.

2.1.1 Validity of the gTDGL formalism

The original Ginzburg-Landau model provides a phenomenological description of superconductivity but lacks the capability to describe dynamic responses to system perturbations or transition processes. The theory also does not incorporate a description of relaxation processes. In an attempt to address this limitation, Lev Landau and Markovich Khalatnikov introduced the concept of a relaxation time for the order parameter, known as the LK theory [139, 140]. This theory was further refined by Albert Schmid, who extended the LK theory with a gauge-invariant description, resulting in the time-dependent Ginzburg-Landau model of superconductivity [141, 142].

It is noteworthy that Schmid's microscopic validity of the GL and TDGL models applies only to gapless superconductors [143]. Consequently, a further extension of the model was necessary to describe superconductors with an energy gap. This was accomplished by Lorenz

Kramer and Richard Watts-Tobin, who introduced a microscopic parameter to describe the energy gap, leading to the development of the generalised time-dependent Ginzburg-Landau (gTDGL) model [144, 145].

The gTDGL model is considered to be one of the most powerful methods for studying dynamic behavior in superconductivity. The following theory has been utilized in this thesis to perform studies of superconductivity.

2.1.2 Free energy functional and order parameter relaxation time

The emergence of a superconducting state is a consequence of a thermodynamic phase transition, which occurs when the temperature of the material falls below a critical temperature, leading to a transition from the normal state of electrons to a superconducting state. During a phase transition, the symmetry of the system changes, and the normal state, which is characterized by higher symmetry, changes to a state of lower symmetry in the superconducting phase.

In the description of the thermodynamic properties of a lower symmetric state, the Helmholtz free energy F is a suitable choice [146]. The theory of phase transitions is valid in the vicinity of the transition point, which, for superconductivity, is the critical temperature T_c. In the proximity of T_c, the free energy can be expressed as a sum of terms that include the complex order parameter Δ, which describes the symmetry of the system. In the superconducting state, the order parameter Δ is non-zero, while in the normal state, it is equal to zero.

Superconductivity belongs to the group of second-order phase transitions when there is no externally applied magnetic field. As a second-order phase transition, the order parameter must be continuous around the critical temperature and rapidly drop to zero at T_c. In this case, the second derivative of the free energy with respect to temperature is proportional to the heat capacity and has a discontinuity at the critical temperature. As is customary with phase transitions, the free energy is obtained by a Taylor expansion in terms of the order parameter Δ and must have a minimum in the function to avoid large diverging values. A typical Taylor expansion in terms of the order parameter would yield a general form of

$$F = c_0 + c_1|\Delta| + c_2|\Delta|^2 + c_3|\Delta|^3 + c_4|\Delta|^4 + o(|\Delta|^5), \tag{2.1}$$

where $c_0 = F_0$ is the free energy of the normal state, and the other coefficients (c_i, $i = 1, 2, 3, ...$) are material-specific parameters. When considering second order phase transitions, the system can be effectively described with an expansion up to the fourth power, and material-specific coefficients impose restrictions on other coefficients. For example, a non-zero order parameter that is invariant to all symmetries is not possible, and thus $c_1 = 0$, and $c_3 = 0$ as we are not considering a first order phase transition. The remaining two coefficients are $c_2 = \alpha$ and $c_4 = \beta/2$, leading to a function of the form

$$F = F_N + \alpha|\Delta|^2 + \frac{\beta}{2}|\Delta|^4, \tag{2.2}$$

which has a similar form to equation 1.6. Here, $|\Delta|$ is analogous to Ψ, but contains information about the superconducting gap, which will be introduced later.

In the presence of an externally applied magnetic field $\mathbf{B}_e$, the Gibbs free energy functional characterizes the superconducting state at thermodynamic equilibrium. This functional is given by the following expression:

$$G_S^{(eq)} = G_N + \int_V \left[\alpha|\Delta|^2 + \frac{\beta}{2}|\Delta|^4\right] dV + \int_V \gamma|\left(-i\hbar\nabla - e^*\mathbf{A}\right)\Delta|^2 dV + \int_V \frac{(\nabla \times \mathbf{A} - \mathbf{B}_e)^2}{2\mu_0} dV. \tag{2.3}$$

Here, G_N is the free energy of the normal state, Δ is the order parameter, and $\mathbf{A}$ is the vector potential. The second term in the expression represents the condensation energy associated with the spatial variation of the order parameter, while the third term describes the gauge-invariant kinetic energy. The fourth term quantifies the energy required to screen the external magnetic field.

The stationary case of the GL equations can be obtained from this free energy functional, but the time-dependent case requires an additional term $G_S^{(relax)}$, which accounts for the relaxation processes in the superconductor. The total free energy is then given by:

$$G_S = G_S^{(eq)} + G_S^{(relax)}. \tag{2.4}$$

It is generally preferred to introduce the relaxation term into the GL equations rather than directly into the free energy. While the relaxation term can be quite complex, it is the variational terms that contain the most significant descriptions.

The variation of the relaxation term with respect to the complex conjugate of the order parameter Δ^* is given by:

$$\partial G_S^{(relax)}|_{\Delta^*} = \int_V \left[\tau\left(\frac{\partial\Delta}{\partial\tau} + i\frac{e^*}{\hbar}\varphi\Delta\right)\right]\delta\Delta^* dV. \tag{2.5}$$

Similarly, the variation of the relaxation term with respect to the vector potential $\mathbf{A}$ is given by:

$$\partial G_S^{(relax)}|_{\mathbf{A}} = \int_V \left[\sigma_n\left(\frac{\partial\mathbf{A}}{\partial t} + \nabla\varphi\right)\delta\mathbf{A}\right] dV. \tag{2.6}$$

Here, τ represents the relaxation time, φ is the electrostatic potential that preserves gauge invariance under temporal variation (as per Schmid and Schön [141]), and σ_n is the normal state conductance.

It is worth noting that equation 2.6 actually contains information about the normal current density, as integration over volume has been omitted in the variation with respect to vector potential.

Generalised time-dependent Ginzburg-Landau equation and the general boundary condition

The time-dependent Ginzburg-Landau (TDGL) formalism is a powerful tool to investigate the dynamics of superconductors. To account for dirty superconductors with a finite gap, a generalised version of the theory was derived from microscopic principles [145]. This extension requires the Gibbs free energy associated with relaxation to contain a complex quantity for the relaxation time. The expression for the relaxation time in dirty superconductors is given by

$$\widetilde{\tau} = \frac{u\tau_{GL}N(0)}{\sqrt{1+\left(\frac{2\tau_i}{\hbar}|\Delta|\right)^2}}\left[1+\frac{(\frac{2\tau_i}{\sqrt{2}\hbar})^2\frac{\partial|\Delta|^2}{\partial t}\Delta}{\frac{\partial\Delta}{\partial t}+i\frac{e^*}{\hbar}\varphi\Delta}\right], \tag{2.7}$$

where τ_{GL} is the Ginzburg-Landau relaxation time of the order parameter, $N(0)$ is the density of states, $u = 5.79$ is a dimensionless ratio for relaxation times for the magnitude and phase of the order parameter, τ_i is the electron-phonon scattering time, and Δ is the superconducting order parameter. The expression for the relaxation time contains a dependence on the magnitude and phase of the order parameter. The presence of electron-phonon scattering introduces a type of viscosity in the superconducting condensate of Cooper pairs, adding an extra degree of complexity to the dynamics.

The relation $\Gamma = \frac{2\tau_i}{\hbar}\Delta$ appears in the equation for the relaxation time and accounts for the presence of the superconducting gap and finite scattering times. This relation can be used as a control parameter to change the effective viscosity of the condensate.

When deriving the gTDGL equations, the first step is to perform variation with respect to both Δ and $\mathbf{A}$. First variation with respect to Δ is performed on equation 2.4, which has the form

$$\begin{aligned}\partial G_S|_{\Delta^*} = \int_V &\left[\frac{\tau_{GL}N(0)\left[\frac{\partial\Delta}{\partial t}+i\frac{e^*}{\hbar}\varphi\Delta+\left(\frac{2\tau_i}{\sqrt{2}\hbar}\right)^2\frac{\partial|\Delta|^2}{\partial t}\Delta\right]u}{\sqrt{1+\left(\frac{2\tau_i}{\hbar}|\Delta|\right)^2}}\right]\delta\Delta^* dV \\ &+\partial G_S^{(eq)}|_{\Delta^*} = 0,\end{aligned} \tag{2.8}$$

where the the equilibrium term of the free energy is expressed as

$$\begin{aligned}\partial G_S|_{\Delta^*}^{(eq)} = &\int_V \left\{\alpha\Delta\delta\Delta^*+\beta|\Delta|^2\Delta\delta\Delta^*\right\}dV \\ &+\int_V \left\{\gamma\left[\left(-i\hbar\nabla-e^*\mathbf{A}\right)\Delta\right]\left[\left(i\hbar\nabla-e*\mathbf{A}\right)\delta\Delta^*\right]\right\}dV.\end{aligned} \tag{2.9}$$

The above equation can be rearranged algebraically such that

$$\begin{aligned}\partial G_S|_{\Delta^*}^{(eq)} = &\int_V \left[\left(\alpha+\beta|\Delta|^2\right)\Delta-\gamma\left(\hbar\nabla-ie^*\mathbf{A}\right)^2\Delta\right]\delta\Delta^* dV \\ &+\int_V \left\{i\hbar\gamma\nabla\left[\delta\Delta^*\left(-i\hbar\nabla\Delta-e^*\mathbf{A}\Delta\right)\right]\right\}dV.\end{aligned} \tag{2.10}$$

Gauss's theorem ($\int_V \nabla \cdot \mathbf{M} dV = \oint \mathbf{n} \cdot \mathbf{M} dS$) can then be applied to the second term in equation 2.10, yielding the equation

$$\partial G_S|_{\Delta^*}^{(eq)} = \int_V \left[\left(\alpha + \beta|\Delta|^2\right)\Delta - \gamma \left(\hbar\nabla - ie^*\mathbf{A}\right)^2 \Delta \right] \delta\Delta^* dV \\ + \oint_S \mathbf{n} \cdot \left(-i\hbar\nabla\Delta - e^*\mathbf{A}\Delta\right) \delta\Delta^* dS \tag{2.11}$$

The last term in the above equation relates to the supercurrent flowing out of the superconducting volume perpendicular to the surface, which is not physically true, in fact

$$\oint_S \mathbf{n} \cdot \left(-i\hbar\nabla\Delta - e^*\mathbf{A}\Delta\right) \delta\Delta^* dS = 0,$$

and so that term is equal to zero. The gTDGL can then be obtained with substitution of equation 2.11 into 2.8, expressed as

$$\tau_{GL} N(0) \frac{u}{\sqrt{\left(1 + \frac{2\tau_i}{\hbar}|\Delta|\right)^2}} \left[\frac{\partial\Delta}{\partial t} + i\frac{e^*}{\hbar}\varphi\Delta + \left(\frac{2\tau_i}{\sqrt{2}\hbar}\right)^2 \frac{\partial|\Delta|^2}{\partial t}\Delta \right] \\ = -\left(\alpha + \beta|\Delta|^2\right)\Delta + \gamma\left(\hbar\nabla - ie^*\mathbf{A}\right)^2\Delta \tag{2.12}$$

The generalised boundary condition for equation 2.12 was proposed by De Gennes [72] as

$$\mathbf{n} \cdot \left(-i\hbar\nabla - e^*\mathbf{A}\right)\Delta|_{boundary} = \frac{i}{b}\Delta|_{boundary}, \tag{2.13}$$

where the parameter b is the extrapolation length and represents the length at which the order parameter would decay to zero if the gradient of decay at the superconducting surface remained constant.

When considering different types of interfaces with superconductors, the behavior of the order parameter near the interface is an important quantity to consider. For a superconducting-insulator (SI) boundary, the order parameter drops abruptly to zero, which means that the extrapolation length b goes to infinity. On the other hand, for a superconducting-normal (SN) boundary, the proximity effect [147] can result in a small amount of Cooper pairs tunneling into the normal metal, thereby suppressing superconductivity close to the boundary. In this case, b is positive and large-finite.

For a superconducting-superconducting (SS') boundary, it is common practice to assign a negative and finite value to b for the superconductor with a lower T_c. Finally, in the case of a superconducting-ferromagnetic boundary, the order parameter quickly vanishes from the interface, and the extrapolation length tends to zero ($b \longrightarrow 0$).

2.1.3 Superconducting current, total current and conservation

To obtain the second TDGL equation the same type of variation of the free energy functional is performed, but now with respect to the vector potential ($\delta\mathbf{A}$), this reads

$$\partial G_S|_{\mathbf{A}} = \partial G_S^{(eq)}|_{\mathbf{A}} + \partial G_S^{(relax)}|_{\mathbf{A}} = 0, \tag{2.14}$$

where the relaxation term is provided in equation 2.6. By applying $\delta\mathbf{A}$ to equation 2.3 the following relation is obtained

$$
\begin{aligned}
\partial G_S^{(eq)}|_{\mathbf{A}} = \frac{1}{\mu_0}\int_V & \left[(\nabla \times \mathbf{A} - \mathbf{B}_e) \cdot \nabla \times \delta\mathbf{A}\right] dV \\
&+ \int_V \left[\gamma \left(e^* \delta\mathbf{A}\Delta^*\right) \cdot \left(i\hbar\nabla + e^*\mathbf{A}\right)\Delta\right] dV \\
&- \int_V \gamma \left[\left(e^* \delta\mathbf{A}\Delta\right) \cdot \left(i\hbar\nabla - e^*\mathbf{A}\right)\Delta^*\right] dV. \qquad (2.15)
\end{aligned}
$$

This equation can be modified through substitution using the vector identity $\nabla \cdot (\mathbf{M} \times \mathbf{N}) = \mathbf{N} \cdot \nabla \times \mathbf{M} - \mathbf{M} \cdot \nabla \times \mathbf{N}$. Given that $\mathbf{N} = \nabla \times \mathbf{A} - \mathbf{B_e}$ and $\mathbf{M} = \delta\mathbf{A}$ and algebraic rearrangement the equation reads

$$
\begin{aligned}
\partial G_S^{(eq)}|_{\mathbf{A}} = \frac{1}{\mu_0}\int_V & \left\{\delta\mathbf{A} \cdot \nabla \times \nabla \times \mathbf{A} + \nabla \cdot \left[\delta\mathbf{A} \times (\nabla \times \mathbf{A} - \mathbf{B}_e)\right]\right\} dV \\
&+ \int_V \left[\gamma \left(e^* \delta\mathbf{A}\Delta^*\right) \cdot \left(i\hbar\nabla + e^*\mathbf{A}\right)\Delta\right] dV \\
&- \int_V \gamma \left[\left(e^* \delta\mathbf{A}\Delta\right) \cdot \left(i\hbar\nabla - e^*\mathbf{A}\right)\Delta^*\right] dV. \qquad (2.16)
\end{aligned}
$$

Here, Gauss's theorem can be used once again, where

$$
\oint_S \left[\delta\mathbf{A} \times (\nabla \times \mathbf{A} - \mathbf{B}_e)\right] \cdot d\mathbf{S} = \int_V \left\{\nabla \cdot \left[\delta\mathbf{A} \times (\nabla \times \mathbf{A} - \mathbf{B}_e)\right]\right\} dV,
$$

with the condition that this only has physical relevance for the surface $\mathbf{S}$ bounding the superconductor. However, at the boundary $\nabla \times \mathbf{A} = \mathbf{B}_e$, so this term is equal to zero. Now by combining both relaxation and stationary terms the following equation is obtained

$$
\begin{aligned}
\partial G_S|_{\mathbf{A}} = \frac{1}{\mu_0}\int_V & \left(\nabla \times \nabla \times \mathbf{A}\right) \cdot \delta\mathbf{A} dV \\
&+ \int_V \left(\sigma_n \nabla\varphi + \sigma_n \frac{\partial\mathbf{A}}{\partial t}\right) \cdot \delta\mathbf{A} dV \\
&- \int_V \left[2e^*\hbar\gamma \left(\frac{\Delta^*\nabla\Delta - \Delta\nabla\Delta^*}{2i} - \frac{e^*}{\hbar}|\Delta|^2\mathbf{A}\right)\right] \cdot \delta\mathbf{A} dV = 0. \qquad (2.17)
\end{aligned}
$$

This relation suggests that for a given $\delta\mathbf{A}$ the sum of the integrals must be zero for it to hold true. Therefore, the following relation can be proposed

$$
\begin{aligned}
\frac{1}{\mu_0}\left(\nabla \times \nabla \times \mathbf{A}\right) = -\sigma_n & \left(\nabla\varphi + \frac{\partial\mathbf{A}}{\partial t}\right) \\
&+ 2e^*\hbar\gamma \left(\mathfrak{F}\left\{\Delta^*\nabla\Delta\right\} - \frac{e^*}{\hbar}|\Delta|^2\mathbf{A}\right), \qquad (2.18)
\end{aligned}
$$

where each term corresponds to a value of current density. Recalling Ampere's law, the left hand side term is the total current density $\mathbf{J}$ and can be expressed as

$$\mathbf{J} = \frac{1}{\mu_0} \left(\nabla \times \nabla \times \mathbf{A} \right). \tag{2.19}$$

The two terms on the right hand side are the normal current density $\mathbf{J}_n$ and the supercurrent density $\mathbf{J}_s$, which are expressed respectively as

$$\mathbf{J}_n = -\sigma_n \left(\nabla\varphi + \frac{\partial \mathbf{A}}{\partial t} \right) \tag{2.20}$$

and

$$\mathbf{J}_s = 2e^*\hbar\gamma|\Delta|^2 \left(\nabla\theta - \frac{e^*}{\hbar}\mathbf{A} \right), \tag{2.21}$$

where the relation $\Delta = |\Delta|e^{i\theta}$ has been used.

Introduction of the relaxation terms has revealed a third independent variable (with Δ and $\mathbf{A}$), the electrostatic potential φ. To account for this the conservation of current must be included, which reads

$$\nabla \cdot \mathbf{J} = \nabla \cdot (\mathbf{J}_s + \mathbf{J}_n) = \frac{\partial \rho}{\partial t}. \tag{2.22}$$

When the superconductor is close to critical temperature any time-variation of charge accumulation ($\rho \propto \frac{e^*}{\hbar}\varphi - \frac{\partial\theta}{\partial t}$) can be ignored such that $\frac{\partial\theta}{\partial t} \longrightarrow 0$. This leads to the important relation between normal and super current density of

$$-\nabla \cdot \mathbf{J}_n = \nabla \cdot \mathbf{J}_s, \tag{2.23}$$

which has the physical meaning that normal current injected into the superconductor transforms into superconducting current.

At this point a set of gTDGL equations have been obtained which are able to describe the superconducting dynamics when the system is exposed to either an external magnetic field and/or and electric field. The three equations are equations 2.12, 2.18 and 2.23, accounting for the independent variables $(\Delta, \mathbf{A}, \varphi)$, which are invariant under a gauge transformation. Such that, $\Delta \longrightarrow \Delta e^{i\Omega}$, $\mathbf{A} \longrightarrow \mathbf{A} + \frac{e^*}{\hbar}\nabla\Omega$, and $\varphi \longrightarrow \varphi - \frac{\hbar}{e^*}\frac{\partial\Omega}{\partial t}$ when $\Omega(\mathbf{r}.t)$ is a function that varies slowly temporally with respect to the Ginzburg-Landau time τ_{GL}.

Stationary GL equations

The stationary GL formalism was briefly mentioned previously, and here we explain how it reduces to the stationary case. When an external direct current (DC) is applied to a superconductor in an equilibrium state, if the magnitude of the current is less than a critical current that could cause persistent oscillations in the superconductor, then after some time a new equilibrium state would be achieved. As long as external excitations from magnetic fields and applied current are small enough to avoid a transition to the normal state or oscillatory vortex motion, the state would reach a new stationary state, permitting the use of the stationary GL equations. In the stationary case, time derivatives and electrostatic potential are neglected, and the pair of GL equations read:

$$\gamma\left(\hbar\nabla - ie^*\mathbf{A}\right)^2\Delta = \alpha\Delta + \beta|\Delta|^2\Delta, \tag{2.24}$$

$$\frac{1}{\mu_0}\left(\nabla\times\nabla\times\mathbf{A}\right) = 2e^*\hbar\gamma|\Delta|^2\left(\nabla\theta - \frac{e^*}{\hbar}\mathbf{A}\right). \tag{2.25}$$

These equations still require the boundary condition given in equation 2.13. The stationary equations provide important results regarding different superconducting states, such as ground and excited states. However, for a dynamic case, the TDGL equations are required. When using the GL equations to study superconductors numerically, the stationary approach is less computationally demanding compared to the TDGL case. As a result, larger systems can be investigated more easily when considering stationary phenomena. It is worth mentioning that the stationary GL framework has been successfully used to study the qualitative behavior of the first critical current J_{C1} by using a "computational trick" [148].

The microscopic origin of characteristic quantities

Considering the GL-theory was established from a phenomenological aspect, it was important to the theory that microscopic explanations of the characteristic quantities were provided. As mentioned, the generalised-TDGL equations for "dirty" superconductors were provided by Watts-Tobin and Kramer [144], which is one of the most complete frameworks for studying the behaviour of superconductors. The proposed gTDGL are given as

$$\begin{aligned}&\frac{N(0)\pi\hbar}{8k_BTu}\frac{u}{\sqrt{1+\left(\frac{2\tau_i|\Delta|}{\hbar}\right)^2}}\left[\frac{\partial\Delta}{\partial t} + i\frac{e^*}{\hbar}\varphi\Delta + \left(\frac{2\tau_i}{\sqrt{2}\hbar}\right)^2\frac{\partial|\Delta|^2}{\partial t}\Delta\right]\\ &= \frac{N(0)\pi\hbar D}{8k_BT}\left(\nabla - i\frac{e^*}{\hbar}\mathbf{A}\right)^2\Delta + \left(N(0)f(T) - g(T)\frac{N(0)\pi^2}{16uk_B^2T^2}|\Delta|^2\right)\Delta,\end{aligned} \tag{2.26}$$

$$\frac{1}{\mu_0}\nabla\times\nabla\times\mathbf{A} = \sigma_n\left[\frac{\pi}{2k_BTe^*}|\Delta|^2\left(\nabla\theta - \frac{e^*}{\hbar}\mathbf{A}\right) - \frac{\partial\mathbf{A}}{\partial t} - \nabla\varphi\right], \tag{2.27}$$

$$\begin{aligned}-\nabla\cdot\mathbf{J}_n &= \nabla\cdot\left[\sigma_n\left(\frac{\partial\mathbf{A}}{\partial t} + \nabla\varphi\right)\right]\\ &= \nabla\cdot\mathbf{J}_s = \nabla\cdot\left[\frac{\sigma_n\pi}{2k_BTe^*}|\Delta|^2\left(\nabla\theta - \frac{e^*}{\hbar}\mathbf{A}\right)\right],\end{aligned} \tag{2.28}$$

where $f(T)$ and $g(T)$ are the temperature dependence kernels, and D is the diffusion parameter. A microscopic description of the normal state conductivity reads

$$\sigma_n = \frac{{e^*}^2DN(0)}{2}. \tag{2.29}$$

The GL theory is derived respecting the theory of second order phase transitions, in the above set of equations the temperature T can be substituted for T_c, expect for the temperature kernels which preserve the generic thermal dependence. Within the gTDGL model the most accurate temperature dependence is given by the following functions [74]

$$f(T) = \frac{T_c^2 - T^2}{T_c^2 + T^2},$$

and

$$g(T) = \frac{T_c^4}{(T_c^2 + T^2)^2}.$$

The microscopic expressions for the set of phenomenological material specific parameters present in the GL equations are given by

$$\alpha = -N(0)f(T) = -\alpha(0)f(T), \tag{2.30}$$

$$\beta = g(T)\frac{N(0)\pi^2}{16uk_B^2T_c^2} = \beta(0)g(T), \tag{2.31}$$

$$\gamma = \frac{N(0)\pi D}{8k_BT_c\hbar}, \tag{2.32}$$

$$\tau_{GL} = \frac{\pi\hbar}{8k_BT_c(1 - T/T_c)u} = \frac{\tau_{GL}(0)}{(1 - T/T_c)}. \tag{2.33}$$

With the equations for α, β and γ it's now possible to define the important characteristic length scales of the coherence length ξ and the penetration depth λ. The order parameter varies over length scales comparable to the coherence length, which is defined as $\xi = \sqrt{-\frac{\gamma\hbar^2}{\alpha}}$. It can be seen that ξ is temperature dependent (present in α), and is affected by impurities in the material which changes the value of the diffusion parameter D (present in γ). There are two limits in which D is expressed differently [149]. Firstly, in the dirty limit $D = v_F\ell$ (v_F is the Fermi velocity, and ℓ the elastic scattering mean free path), which can be assumed when Cooper pairs interact with impurities that are on length scales smaller than the BCS coherence length $\xi_0 > \ell$. In the clean limit, when impurities are much larger than ξ_0, $D = \frac{\pi\hbar v_F^2}{12uk_BT_c}$, so the effective coherence length can take the forms

$$\xi(T) = \begin{cases} \sqrt{\frac{\hbar\pi v_F l}{8k_BT_cf(T)}} = 0.855\sqrt{\frac{\xi_0 l}{f(T)}}, & dirty \\ \sqrt{\frac{\hbar^2\pi^2v_F^2}{96uk_B^2T_c^2f(T)}} = 0.74\frac{\xi_0}{\sqrt{f(T)}}, & clean \end{cases} = \frac{\xi(0)}{\sqrt{f(T)}}. \tag{2.34}$$

The penetration depth λ associated with the spatial variation of the magnetic field inside the superconductor can be expressed as $\lambda = \sqrt{-\frac{\beta}{2\mu_0 e^{*2}\alpha\gamma}}$, according to GL theory. The penetration depth depends on α, β, and γ, so is both temperature and impurity dependent, taking the forms

$$\lambda(T) = \begin{cases} \sqrt{\frac{\pi\hbar g(T)}{4uk_BT_c\mu_0 e^{*2}N(0)v_F l f(T)}} = \frac{\lambda(0)}{\sqrt{2}}\sqrt{\frac{\xi_0 g(T)}{1.33 l f(T)}}, & dirty \\ \sqrt{\frac{3g(T)}{\mu_0 e^{*2}N(0)v_F^2 f(T)}} \qquad\qquad = \frac{\lambda(0)}{\sqrt{2}}\sqrt{\frac{g(T)}{f(T)}}, & clean \end{cases}. \tag{2.35}$$

It's important to mention the connection between Δ and Ψ. As initially proposed in the work of Ginzburg and Landau, the order parameter was represented with Ψ, and was intuitively believed to represent some kind of wave function, which was confirmed by Gor'kov in his microscopic derivation of the GL theory considering $T \longrightarrow T_c$ [64]. The superconducting energy gap is related to the order parameter with the following expression

$$\Psi = \Delta\sqrt{2m^*\gamma}. \tag{2.36}$$

The complete set of equations describing the gTDGL model can be written in terms of Ψ as

$$\begin{aligned} \tau_{GL}N(0)\frac{u}{\sqrt{1+(\Gamma|\Psi|)^2}}\left[\frac{\partial\Psi}{\partial t} + i\frac{e^*}{\hbar}\varphi\Psi + \left(\frac{\Gamma}{\sqrt{2}}\right)^2\frac{\partial|\Psi|^2}{\partial t}\Psi\right] \\ = -(a+b|\Psi|^2)\Psi + \frac{\hbar^2}{2m^*}(\nabla - ie^*\mathbf{A})^2\Psi, \end{aligned} \tag{2.37}$$

$$\frac{1}{\mu_0}\nabla\times\nabla\times\mathbf{A} = \frac{e^*\hbar}{m^*}|\Psi|^2\left(\nabla\theta - \frac{e^*}{\hbar}\mathbf{A}\right) - \sigma_n\left(\frac{\partial\mathbf{A}}{\partial t} + \nabla\varphi\right), \tag{2.38}$$

$$\nabla\cdot\left[\sigma_n\left(\frac{\partial\mathbf{A}}{\partial t} + \nabla\varphi\right)\right] = \nabla\cdot\left[\frac{e^*\hbar}{m^*}|\Psi|^2\left(\nabla\theta - \frac{e^*}{\hbar}\mathbf{A}\right)\right], \tag{2.39}$$

where the material dependent parameters are $a = \frac{\alpha}{2m^*\gamma}$, $b = \frac{\beta}{4m^{*2}\gamma^2}$, and $\Gamma = \frac{2\tau_i}{\hbar\sqrt{2m^*\gamma}}$. The equations are a comprehensive description of the behaviour of superconductors, but can still be modified further as will be shown later.

Coupling of thermal balance equation into the gTDGL model

As we delve deeper into the study of superconductors, it becomes increasingly important to consider the effects of heating mechanisms on their behavior. The thermal balance equation can be coupled to the generalized time-dependent Ginzburg-Landau (gTDGL) model to account for such effects. It should be noted that the thermally dependent material parameters α and β, as well as the characteristic lengths ξ and λ, are already present in the gTDGL equations. This means that thermal fluctuations can have a significant impact on the behavior of the superconductor, potentially even driving it into the normal state.

One example of the effects of heating on superconductors can be seen in the dissipative state, where vortices can cross the stripe and Joule heating occurs, causing local temperatures to increase. If thermal quenching is not sufficient, the temperature of the superconductor can rise above T_c, leading to a transition to the normal state. Another example is the superconducting single photon detector, where incoming photons are absorbed and produce hot spots. Understanding the behavior of this device, which relies on a thermal process, requires inclusion of the heat balance equation in the gTDGL equations.

To account for the thermal effects on the superconductor, we can couple the thermal balance equation to the gTDGL equations. In the dynamic state, we are interested in the local spatial and temporal changes in temperature, which can be calculated assuming $T = T(\mathbf{r}, t)$. The general form of the thermal balance equation allows us to account for the effects of heating on the superconductor's behavior.

The general form of the thermal balance equation is [150]

$$C\frac{\partial T}{\partial t} = k\nabla^2 T - \frac{h}{d}(T - T_0) + P_{th}(\mathbf{r}, t), \tag{2.40}$$

where C is the heat capacity, h is the heat transfer coefficient, k is the heat conductivity, d is the thickness of the material, and T_0 is the bath temperature. The term $P_{th}(\mathbf{r}, t)$ corresponds to an external thermal potential that contains information about the heating process from sources such as single photon impacts, laser irradiation and other possible local heating mechanisms. The simplest form corresponds to Joule heating in the superconductor where of $P_{th}(\mathbf{r}, t) = \mathbf{J}_n^2/\sigma_n$. Even though the thermal balance equation is not native to the gTDGL theory, the equations can still be coupled via the thermal potential considering the Joule heating from the normal current density $\mathbf{J}_n$. This results with an extended version of the gTDGL model that now includes the effects of heating, corresponding to the set of equations 2.26, 2.27, 2.28 and 2.40. These equations can realistically predict the behaviour of superconductors under an applied magnetic field and applied current, whilst considering the consequences of heating within the system. Due to the thermal balance equation not originating directly from the gTDGL theory, the thermal coefficients C, k, and h do not have a microscopic description, and must be found another way. The heat capacity can be estimated from the condensation energy density of the superconductor [151], expressed as

$$C = -T\frac{\partial^2}{\partial T^2}\left[\alpha(T)|\Delta|^2 + \frac{\beta(T)}{2}|\Delta|^4\right]. \tag{2.41}$$

When considering a wide range of temperatures, $\alpha \propto [1 - (T/T_c)^2][1 + (T/T_c)^2]^{-1}$ and $\beta \propto [1 + (T/T_c)^2]^{-2}$, and the heat capacity can be expressed as $C = C_n + \frac{2\alpha(0)^2}{\beta(0)T_c^4}T(3T^2 - T_c^2)$. Around T_c, the heat conductivity can be expressed using the Wiedemann-Franz law [152]

$$k = \sigma_n T_c \frac{4\pi^2 k_B^2}{3e^{*2}}, \tag{2.42}$$

however, a more complex description may be needed considering the system. The thermal balance equation contains a few important characteristic quantities. Firstly, the thermal healing length $\Lambda_h = \sqrt{\frac{kd}{h}}$, which represents the scale of how temperature varies in the sample. The heat is removed from the system over a time scale $\backsim \frac{Cd}{h}$, if heating mechanisms occur over a shorter time scale the system can be driven into the normal state. The diffusion of heat is represented by the ratio $\frac{k}{C}$. In reality superconductors are coupled to other systems like substrates, the heating coefficients k and C can be modified to account for this. The effective heat capacity becomes $C_{eff} = C + d_sC_s/d$ and the effective heat conductivity $k_{eff} = k_+d_sk_s/d$, where the subscript s is used for the substrate.

Dimensionless extended-gTDGL equations

In general the extended gTDGL model is solved numerically, so the approach of solving the equations must consider the range of order of magnitude between different quantities such as length scales, characteristic times, and current densities $(10^{-15} - 10^{20})$. To solve the problem of numerical rounding errors during mathematical operations the quantities in the equations are modified to a dimensionless form. The dimensionless form of the extended gTDGL equations are as expressed as

$$\begin{aligned}\frac{u}{\sqrt{1+\widetilde{\Gamma}^2|\chi|^2}}\left[\frac{\partial\chi}{\partial\widetilde{t}} + i\widetilde{V}\chi + \frac{\widetilde{\Gamma}^2}{2}\frac{\partial|\chi|^2}{\partial\widetilde{t}}\chi\right]&\\ = (\widetilde{\nabla} - i\mathbf{Q})^2\chi + (f - g|\chi|^2)\chi,& \qquad (2.43)\end{aligned}$$

$$\kappa\widetilde{\nabla}\times\widetilde{\nabla}\times\mathbf{Q} = |\chi|^2\left(\widetilde{\nabla}\theta - \mathbf{Q}\right) - \frac{\partial\mathbf{Q}}{\partial\widetilde{t}} - \widetilde{\nabla}\widetilde{V}, \qquad (2.44)$$

$$\widetilde{\nabla}\cdot\left(\frac{\partial\mathbf{Q}}{\partial\widetilde{t}} - \widetilde{\nabla}\widetilde{V}\right) = \widetilde{\nabla}\left[|\chi|^2\left(\widetilde{\nabla}\theta - \mathbf{Q}\right)\right], \qquad (2.45)$$

$$\widetilde{c}\frac{\partial\widetilde{T}}{\partial\widetilde{t}} = \widetilde{k}\widetilde{\nabla}^2\widetilde{T} - \widetilde{h}\left(\widetilde{T} - \widetilde{T}_0\right) + \left(\frac{\partial\mathbf{Q}}{\partial\widetilde{t}} - \widetilde{\nabla}\widetilde{V}\right)^2. \qquad (2.46)$$

The dimensionless quantities present in the equation have all been scaled to characteristic quantities of the system. The dimensionless order parameter χ is expressed in units of the bulk GL energy gap at zero temperature $\Delta_{GL}(0) = \frac{4\sqrt{u}k_BT_c}{\pi}$, such that $\chi = \Psi/\Delta_{GL}(0)$. Units of distance are re-scaled by the coherence length at zero temperature $\xi(0) = \sqrt{\frac{\pi\hbar D}{8k_BT_c}}$, such that $\widetilde{\mathbf{r}} = \mathbf{r}/\xi(0)$ and $\widetilde{\nabla} = \xi(0)\nabla$. Units of temperature are re-scaled by T_c, with dimensionless quantity $\widetilde{T} = T/T_c$. The temperature dependence kernels f and g are by definition are dimensionless. The Ginzburg-Landau relaxation time at zero temperature is $\tau_{GL}(0) = \frac{\pi\hbar}{8k_BT_c}$, which is used to re-scale units of time to give $\widetilde{t} = t/\tau_{GL}(0)$, and derivatives in time become $\frac{\partial}{\partial\widetilde{t}} = \frac{\partial}{\partial t/\tau_{GL}(0)}$. The dimensionless magnetic field, $\widetilde{\mathbf{B}} = \mathbf{B}/B_{C2}(0)$ is re-scaled by the upper critical field at zero temperature commonly expressed as $B_{C2}(0) = \frac{\phi_0}{2\pi\xi(0)^2}$, and the dimensionless vector potential is given as $\mathbf{Q} = \mathbf{A}/B_{C2}(0)\xi(0)$. The dimensionless electrostatic potential $\widetilde{V}$ is expressed in units of $\phi_{GL}(0) = \frac{\hbar}{e^*\tau_{GL}(0)}$, which reads $\widetilde{V} = V/\phi_{GL}(0)$. The Ginzburg-Landau current density at zero temperature is expressed as $J_{GL}(0) = \frac{\sigma_n\phi(0)}{\xi(0)}$, which re-scales the current as $\widetilde{\mathbf{J}} = \mathbf{J}/J_{GL}(0)$. The parameter Γ is re-scaled such that the dimensionless quantity is $\widetilde{\Gamma} = \Gamma(\frac{2\tau_i \Delta_{GL}(0)}{\hbar})^{-1}$. The dimensionless expression for the heat coefficients are: $\widetilde{c} = CT_c\sigma_n/\tau_{GL}(0)J^2_{GL}(0)$, $\widetilde{h} = hT_c\sigma_n/J^2_{GL}(0)d$, and $\widetilde{k} = kT_c\sigma_n/J^2_{GL}(0)\xi^2(0)$.

Validity of the extended gTDGL equations and the high-κ regime

The gTDGL equations were initially derived by Watts-Tobin and Kramer in the dirty limit using the local equilibrium approximation (LEA). This resulted in a set of validity criteria that must be met for the equations to be accurate. Specifically, the co-dependent variables Δ, $\mathbf{A}$, and φ must vary slowly with respect to the inelastic scattering times τ_i, and they must also vary over length scales larger than the inelastic diffusion length, $L_i = \sqrt{D\tau_i}$. In the context of gTDGL theory, these criteria can be expressed in terms of the characteristic parameters for time length, namely τ_{GL} and ξ, resulting in the validity criteria $\tau_{GL} \gg \tau_i$ and $\xi \gg L_i$.

The Ginzburg-Landau parameter $\kappa = \frac{\lambda}{\xi}$ is a measure of how magnetic fields penetrate a superconductor, where type-II superconductivity ($\kappa > 1/\sqrt{2}$) results in a mixed state of normal and superconducting regions. In the case of a thin film of any superconducting material, where the thickness is smaller than the coherence length and penetration depth ($d < \xi, \lambda$), the distribution of current is uniform through its depth, which affects the response to the magnetic field. To account for this, an effective GL parameter, $\kappa^* = \kappa\lambda/d$, is proposed [153].

It is worth noting that in the 2D regime where the dimension of the superconductor is reduced and the high-κ regime is reached, any superconducting material effectively behaves as a type-II superconductor. In this regime, the external magnetic field penetrates the superconductor uniformly, and the response from the applied field is negligible, resulting in the omission of equation 2.27 from the proposed gTDGL equations.

The extended gTDGL model is a valuable tool for accurately describing the behavior of superconductors under the influence of both an external magnetic field and transport current. However, a significant challenge arises when considering the impact of the transport current, which naturally induces an electric field that is a function of both the electrostatic scalar potential and the magnetic vector potential. Unfortunately, the extended gTDGL model does not provide an explicit description of the electric field, making it difficult to determine how the transport current affects the vector potential and electrostatics. One potential solution to this problem is to assume specific gauges and implement them into the set of equations, as proposed in Fleckinger et al. (1995). For example, when the zero electrostatic potential gauge is used and $\varphi = 0$, equation 2.45 can be ignored.

In the high-κ regime, where the magnetic field has a uniform distribution over the superconductor, one can adopt the Coulomb gauge where $\nabla \cdot \mathbf{A} = 0$. In this case, for a magnetic field applied perpendicular to the superconductor, the vector potential can be defined using either the symmetric gauge $\mathbf{A} = (-yB_z/2, xB_z/2, 0)$ or the Landau gauge $\mathbf{A} = (yB_z, 0, 0)$, both of which satisfy the Coulomb gauge. When using the Coulomb gauge, equation 2.44 can be omitted from calculations.

To numerically solve the set of equations, discretisation methods are typically used, which involve dividing the system into a finite number of discrete points and approximating the equations at these points. The numerical grid and methods used can significantly impact the accuracy of the results obtained. Further details on numerical approaches can be found in the Appendix.

Inhomogeneity in the extended gTDGL model

The extended gTDGL equations have been expressed in dimensionless units, in such a way that the material properties and universal constants form the dimensionless variables. At the microscopic level, at which the studies are concerned, inhomogeneities on the scale of ξ can strongly affect the behaviour of the superconductor, so it is important that these can be included in numerical simulations. Within the set of equations pertaining to the extended gTDGL equations (equations 2.26, 2.27, 2.28, 2.40), the following material properties appear: T_c, τ_i, $N(0)$, σ_n, D, c, k, and h. When considering inhomogeneities these parameters can be spatially dependent, and possibly even vary with time and with temperature. To accommodate such dependency material parameters could be expressed as

$$T_c(\mathbf{r},t) = T_c^{(0)} p_{T_c}(\mathbf{r},t),$$

$$N(0)(\mathbf{r},t) = N(0)^{(0)} p_{N(0)}(\mathbf{r},t),$$

$$\tau_i(\mathbf{r},t) = \tau_i^{(0)} p_{\tau_i}(\mathbf{r},t),$$

$$D(\mathbf{r},t) = D^{(0)} p_D(\mathbf{r},t),$$

$$\sigma_n(\mathbf{r},t) = \sigma_n^{(0)} p_{\sigma_n}(\mathbf{r},t),$$

$$c[T(\mathbf{r},t)] = c^{(0)} p_c(\mathbf{r},t),$$

$$k[T(\mathbf{r},t)] = k^{(0)} p_k(\mathbf{r},t),$$

$$h[T(\mathbf{r},t)] = h^{(0)} p_h(\mathbf{r},t),$$

where $T_c^{(0)}$, $N(0)^{(0)}$, $\tau_i^{(0)}$, $D^{(0)}$, $\sigma_n^{(0)}$, $c^{(0)}$, $k(0)$, and $h^{(0)}$ are the reference values for each variable. Whilst the variables $p_{T_c}(\mathbf{r},t)$, $p_{N(0)}(\mathbf{r},t)$, $p_{\tau_i}(\mathbf{r},t)$, $p_D(\mathbf{r},t)$, $p_{\sigma_n}(\mathbf{r},t)$, $p_{\sigma_n}(\mathbf{r},t)$, $p_c(\mathbf{r},t)$, $p_k(\mathbf{r},t)$, and $p_h(\mathbf{r},t)$ are the functions describing the spatial and time dependencies.

Chapter 3

Consequences of Confined Vortex Configurations in Superconducting Nanostripes

When a magnetic field is applied to a bulk type-II superconductor, the superconductor initially shields the field by inducing circulating Meissner currents at its edges. However, at the lower critical field H_{c1}, the magnetic field becomes strong enough to penetrate the material in discrete units of magnetic flux quanta Φ_0. This leads to the formation of vortices, which have a radius on the order of the coherence length ξ and exhibit a winding in phase θ of the order parameter. At the center of the vortex, there is a singularity where the order parameter tends to zero ($\Delta(\mathbf{r} = 0) \longrightarrow 0$). The Meissner effect continues to shield the quantized flux by inducing an opposing magnetic field, which creates energetic barriers referred to as Bean-Livingston edge barriers [154, 155]. These barriers create a potential that prevents vortices from entering as the applied magnetic field H is increased and from exiting as H is decreased [156]. In superconducting nanostripes with narrow geometries, where the widths are on the order of ξ, the edge barrier has a significant impact on the system in terms of vortex interactions and the magnetic field required for the initial penetration of vortices into the nanostripe. In this thesis, when referring to H_{c1} in superconducting nanostripes, we are specifically addressing the minimum magnetic field at which a single flux quantum can penetrate the nanostripe. It should be noted that this differs from the behavior observed in bulk samples, which will be demonstrated in our work. In this chapter our novel results relate to the vortex row phase diagram (fig.3.5), the vortex density as a function of H (fig.3.7), and the reconfiguration of vortex rows (fig.3.8). The remainder of the results in this chapter cover well known existing theory

In this chapter, we have conducted numerical simulations on a type of superconducting nanostripes (SN) in the high-κ, as illustrated in figure 1.7. These SN dimensions are characterized by a n infinite lengths L simulates using periodic boundary conditions, widths (w), and thicknesses (d) that greatly surpass the coherence length (ξ) and the magnetic field penetration depth (λ) of the superconducting state. When the magnetic field (H) is sufficiently strong, vortices emerge within the sample, featuring a normal core with a radius of ξ and a magnetic field penetration extent of approximately λ. In the particular thin samples we are studying, the effective penetration depth $\Lambda = \lambda^2/d$ significantly exceeds the dimensions of the SN, causing the magnetic response of the superconductor to be negligibly small compared to the applied magnetic field. In the SGL approach we self-consistently solve the coupled equations

$$(-i\nabla - \mathbf{A})^2 \Delta = \Delta \left(1 - |\Delta|^2\right), \tag{3.1}$$

$$\vec{J} = -\kappa^2 \nabla^2 \mathbf{A} = \frac{1}{2i} \left(\Delta^* \nabla \Delta - \Delta \nabla \Delta^*\right) - |\Delta|^2 \mathbf{A} \tag{3.2}$$

where Δ is the superconducting order parameter, $\mathbf{A}$ is the vector potential, and $\kappa = \Lambda/\xi$ is the effective Ginzburg-Landau parameter. We work with dimensionless units, where length is given in units of the temperature-dependent coherence length $\xi(T) = \xi$, the vector potential $\mathbf{A}$ in units of $c\hbar/2e\xi$, magnetic field $\vec{H}$ in units of the bulk upper critical field $H_{c2} = c\hbar/2e\xi^2$, current in units of the GL current $J_{GL} = c\Phi_0/(8\pi^2\lambda^2\xi)$, and the order parameter Δ is normalized to its value in absence of applied field or sourced current (Δ_0). We impose the Neumann boundary condition at the superconductor-insulator boundary at the lateral edges of the SN

$$\vec{n} \cdot (-i\nabla - \mathbf{A}) \Delta|_{boundary} = 0. \tag{3.3}$$

Along the length of the SN (x-axis) we enforce periodic boundary conditions for $\mathbf{A}$ and Δ, of the form [157]

$$\mathbf{A}(x_0 + L_x) = \mathbf{A}(x) + \nabla \chi_f(x) \tag{3.4}$$

$$\Delta(x_0 + L_x) = \Delta(x) \exp\left[i \frac{2e}{\hbar c} \chi_f(x)\right], \tag{3.5}$$

where $\nabla\chi_f$ respects the gauge used for the magnetic field. To introduce perturbations that induce vortex penetration at the edges of the stripe, a random force term $\tilde{f}(\mathbf{r}, t)$ is introduced to equation (3.1), as suggested in [37, 158]. Equations (3.1) and (3.2) are solved numerically on a discretized Cartesian grid according to Ref. [158], using the finite-difference method and the link-variable approach [37], iteratively until convergence within a prespecified error is achieved. Then the supercurrent is calculated from the value of the order parameter and the vector potential (nearly entirely provided by the external magnetic field). The unit cell length is $L = 32\xi$, which is sufficient to capture the physics of interest in this work. Preliminary simulations were performed with different unit cell lengths, these revealed with unit cell lengths $> 30\xi$ the results were consistent.

3.1 Vortex basics

Figure 3.1 shows an example of a vortex of an excited superconducting state in a finite-length nanostripe of width $w = 6\xi$ when the applied magnetic field is equal to H_{c1}, which is the

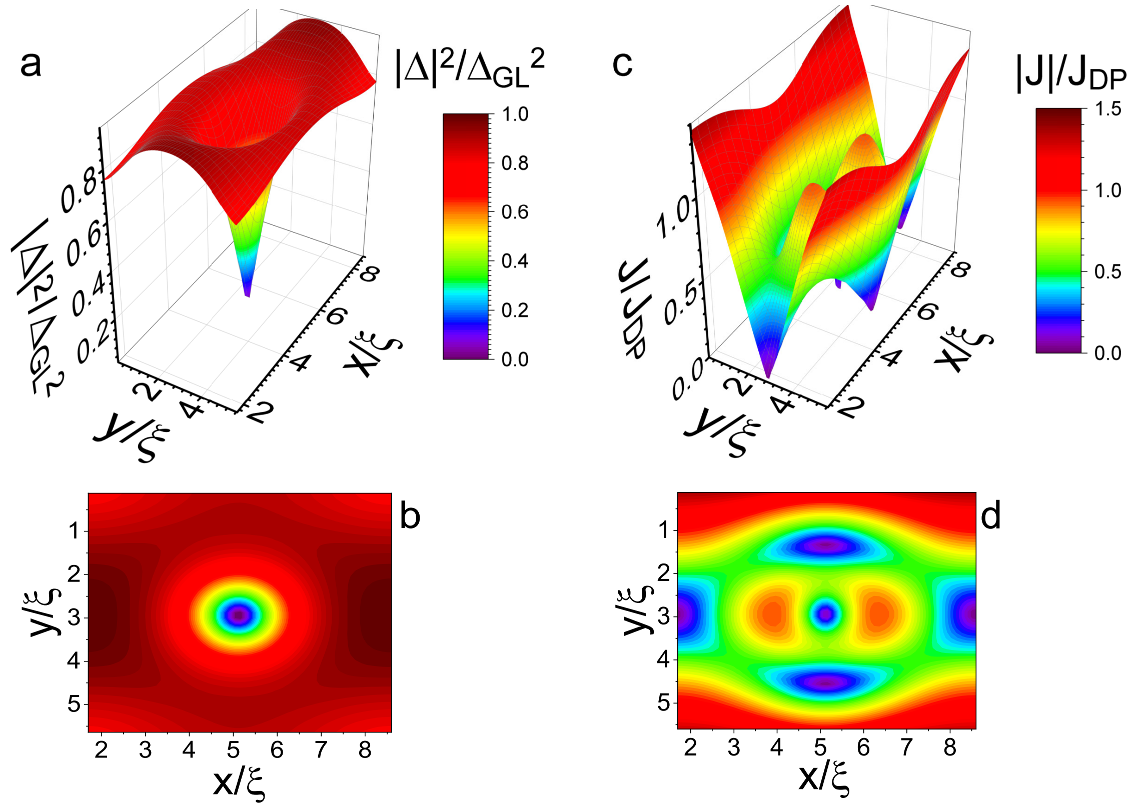

Figure 3.1: Spatial distributions of the superconducting order parameter, $|\Delta|^2$, and the magnitude of the supercurrent density, $|J|$, of a vortex in a long stripe of width $\mathrm{w} = 6\xi$, at an applied magnetic field of $H = H_{c1} = 0.39H_{c2}$. Panel-a shows $|\Delta|^2$ in units of $|\Delta_{GL}|^2$, and panel-b is a 2D-plot of panel-a. Panel-c shows $|J|$ in units of J_{DP}, and panel-d is a 2D-plot of panel-c.

field at which the nanostripe transitions from the exclusive Meissner state to the mixed state with flux penetration by continuously increasing the magnetic field. As the magnetic field is increased from zero, there is a Meissner response at the edges of the nanostripe to shield the superconductor from the external field. When magnetic flux penetrates the material, the superconducting state continues to shield the magnetic field, both at the edges and vortices.

The Meissner field is a result of the supercurrent induced to shield itself from the applied magnetic field. Figure 3.2 shows the current density induced across the width of the nanostripe at the location of vortex penetration, at increasing applied magnetic fields, for nanostripes of widths $w = 6\xi$, $w = 12\xi$, and $w = 18\xi$. The maximum magnitude of the supercurrent density at the edge (J_{edge}) increases with the applied magnetic field (flowing in opposite directions on opposing sides) until a local maximum is reached at $H \simeq 0.25H_{c2}$. Then, it starts decreasing towards a minimum at $H = 0.38H_{c2}$, which is still in the fully Meissner state. At $H = 0.39H_{c2}$, the stripe transitions to the mixed state, and there is a jump in the magnitude of J_{edge} due to the redistribution of current to shield the flux penetration in the sample center.

Similar behavior is observed in stripes of widths $w = 12\xi$ and $w = 18\xi$, but the effect is less pronounced for wider stripes, and the maximum value of J_{edge} for a given field tends towards $1.0J_{DP}$. The smaller the width of the stripe, the higher the applied magnetic field required to transition to the mixed state with vortex penetration. As the magnetic field increases, energy is introduced into the superconductor, which excites electrons and suppresses the superconducting state.

When a superconductor is exposed to an external magnetic field, it responds by generating a Meissner field that shields the superconducting state. The strength of this Meissner field depends on the density of Cooper pairs, which decreases as the magnetic field increases. As a result, the supercurrent density at the edge of the superconductor exhibits local maxima and minima with increasing width due to the larger applied fields required to penetrate the stripe initially.

In figure 3.2, the edge current density (J_{edge}) normalized by the depairing current (J_{DP} - current density required to destroy Cooper pairs and thus superconductivity) for different strengths of the magnetic field. However, we observe that J_{DP} is exceeded over some distance from the edge for narrower stripes (6 and 12ξ) known to exhibit strong confining currents that surpass J_{DP} [44, 39, 34]. Hence, the vortex nucleation conditions do not depend on exceeding the Ginzburg-Landau depairing current density J_{DP} as it can be exceeded in narrow stripes.

3.2 Vortex entry criteria

In the context of superconducting nanostripes, the onset of additional vortex entry is governed by the supervelocity, $\Pi = |(\nabla\theta - \mathbf{A})|$, where θ is the phase of the superconducting order parameter and $\mathbf{A}$ is the vector potential associated with the magnetic field [38, 39, 159]. When the supervelocity at the edge of the nanostripe exceeds a critical value, a chain of vortices nucleates at the edge [39]. The spacing between these vortices, l, is inversely proportional to the difference between the supervelocity at the edge and the critical value, $\Delta\Pi = |\Pi_{edge} - \Pi_{cr}|$. The time for their entrance decreases with increasing $\Delta\Pi$ [39]. As vortices enter the nanostripe, they reduce the supervelocity at the edge until it once again reaches the critical value for the nucleation of a new vortex. This process results in serrations in the supervelocity profile, as shown in Figure 3.3-a. These serrations are associated with the entrance of quantized magnetic flux [39], and become more pronounced in narrower nanostripes.

In figure 3.3-a, we observe the supervelocity at the edge of the nanostripes (normalized by $\Pi_0 = J_{GL}/|\Delta_0|^2$) as a function of the applied magnetic field for different widths of the stripes. The simulations were performed by sweeping the magnetic field and continuing the simulation from the last superconducting state, which is not necessarily the ground state. By increasing the magnetic field in this way, we can find values of Π that correspond to the

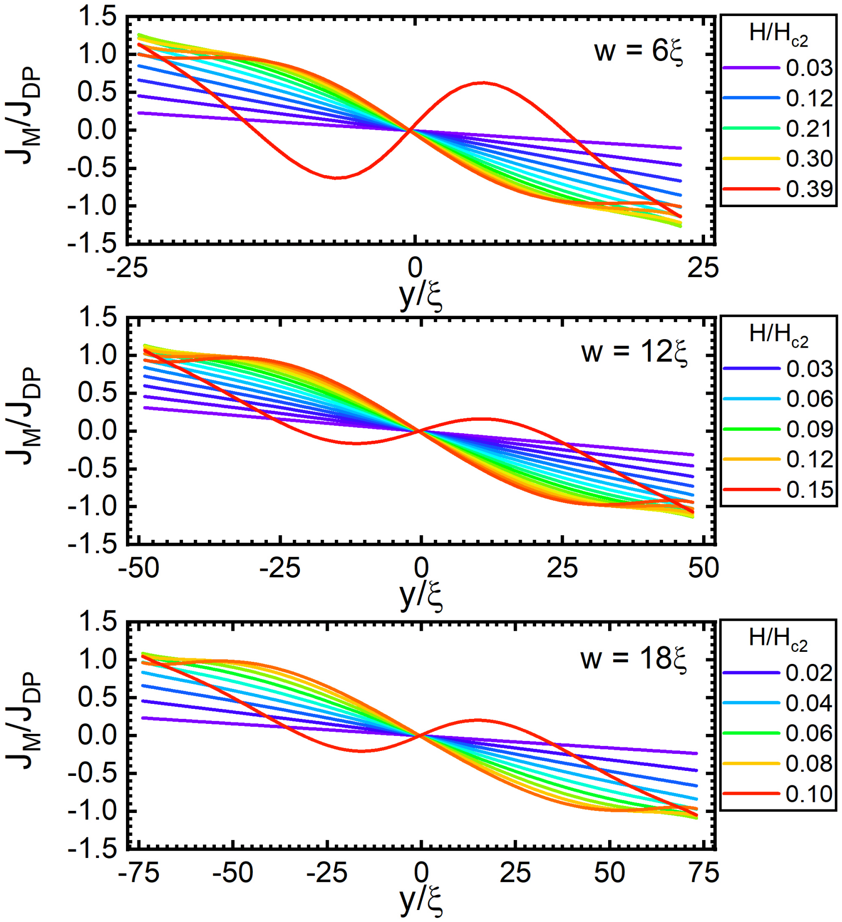

Figure 3.2: Edge Meissner current density across the width of different stripes with widths $w = 6$, 12, and 18ξ at increasing magnetic fields up to H_{c1}.

field of first vertex entry H_{c1} (not equal to H_{c1}, indicated by vertical lines) and subsequent vortex entrances.

The first maximum in the supervelocity, $\Pi_{edge}(H_{c1})$, changes significantly with the width of the nanostripe and is more pronounced at smaller widths. However, towards H_{c2}, the value of Π_{edge} converges to $\simeq 0.90\Pi_0$ for all widths, which is close to the value found when $\kappa \gg 1$ ([39] - figure 5).

In the work of [39], a combination of numerical and analytical studies were conducted to understand the criteria at which vortices enter the superconductor. They found that the controlling parameter was actually the supervelocity, rather than the current density at the edge. Solving the set of stationary GL equations for a thin nanostripe of width 25ξ with $\kappa = 2$, they observed a critical velocity for vortex entry of $\Pi_{critical} \simeq 1\Pi_0$. By direct solution of the GL equations, they found the value to be $0.97\Pi_0$. Through an analytical approach,

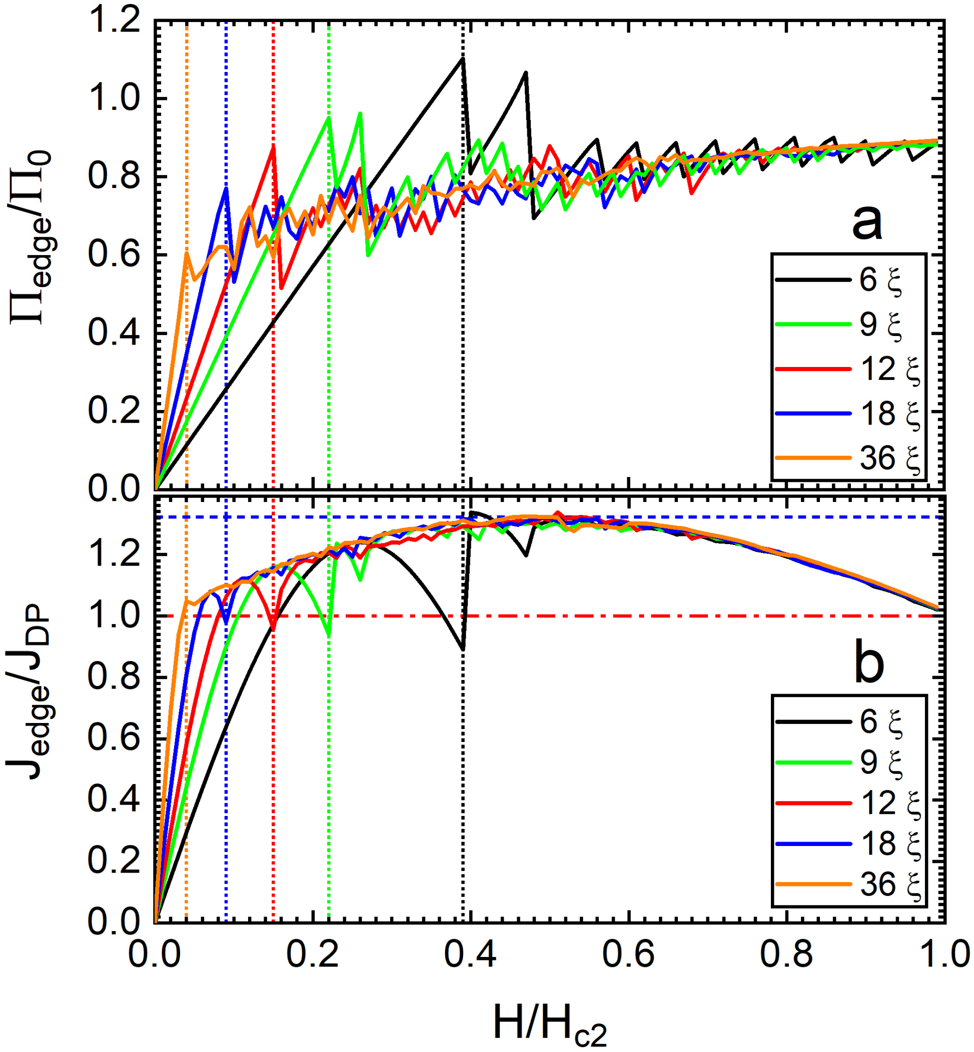

Figure 3.3: Panel a: Supervelocity at edge of stripe as a function of applied magnetic field for different widths of nanostripes (see legend). The first maximum in Π_{edge} corresponds to the critical value related to the field just before vortices first penetrate the stripe, i.e. H_{c1}. Panel b: Current density at the edge of the stripe as a function of the applied magnetic field for different widths. Horizontal lines correspond to the depairing current density $J_{DP} = 0.385 J_0$ (red dash-dot), and the maximum value occurring at $H \simeq 0.5 H_{c2}$ with a value of $J_{edge} \simeq 1.32 J_{DP}$ (blue dash).Vertical dotted lines indicate H_{c1} for the different widths (0.39, 0.22, 0.15, 0.09, $0.04 H_{c2}$). The magnetic field is continuously increased in increments of 0.01 H_{c2}.

they found a value of $\Pi_{critical} \simeq 0.78 \Pi_0$ at the entrance field of the first vortices. Using the same methods of calculation for $\kappa = 5$, they found more consistency in the values (0.80, 0.85,

$0.75\Pi_0$).

The figure shown in 3.3-b presents the variation of the current density J_{edge} at the edge of the stripe with the applied magnetic field. The vertical lines in the figure indicate the critical field H_{c1} for each stripe width. Interestingly, the current density J_{edge} is observed to exceed the depairing current J_{DP} even before the vortices enter the nanostripe from the edge, reaching a maximum value before decreasing to a local minimum associated with H_{c1}, after which vortex penetration occurs. The first maximum of the edge current density decreases with increasing stripe width, while the first local minimum increases for wider stripes. In both cases, the values tend towards the depairing current J_{DP}. When the magnetic field is increased beyond H_{c1}, the value of J_{edge} increases for each stripe width, reaching a maximum value of $J_{edge} \simeq 1.32 J_{DP}$ at a magnetic field of $0.5H_{c2}$. After this, J_{edge} decreases and reaches J_{DP} at H_{c2} for each stripe width. The results indicate that for wide nanostripes with widths greater than 36ξ, vortex penetration occurs when the edge current density is approximately equal to the depairing current, $J_{edge} \simeq J_{DP}$. Narrow nanostripes, on the other hand, exhibit a slight deviation towards lower values, but the deviation is no more than about $10 - 15\%$ for stripe widths $w \lesssim 6\xi$.

Figure 3.4 shows the supervelocity and supercurrent density at the edge of SNs, as a function of applied magnetic field, for different widths (w = 6, 12, and 18ξ), where here the superconducting states are ground states. As the states are ground states, it does not correspond to the critical criteria of stripes penetrating from the edge, but rather the values of $\Pi_{edge}(H)$ and $J_{edge}(H)$ for the state with lowest energy at a given magnetic field. The serrations observed in all curves, as previously mentioned are associated to the penetration of one or more vortices, and it is clear from the number of serrations that more vortices penetrate the wider stripes. For reference, in each plot for different width, a horizontal red-dotted line shows the value for the depairing current, J_{DP}.

Figure 3.4 reveals some interesting features, firstly Π_{edge} at H_{c1} is less than Π_{edge} at H_{c1}, which is to be expected as the mixed state can have lower free energy than the Meissner state [160]. Comparing $\Pi_{edge}(H)$ for widths $w = 12$ and 18ξ it can be seen that the gradient of Π_{edge} is steep for up to the transition of the second row ($n = 2$), after which the general gradient is small and converges around $\Pi_{edge} \simeq 0.72\Pi_0$ for stronger larger fields. A similar convergence was seen in figure 3.3, but here the stationary GL equations were used which neglects the contribution of the electric potential, and we are considering the ground state. Nevertheless, convergence of Π_{edge} for strong magnetic fields seems to occur for all widths considered.

It can be seen from figure 3.4 how Π changes with H for the superconducting ground states (at H). The plots show how Π_{edge} sharply increases for small values of H, and gradually increases as H is increased. The figure shows values up to $H = H_{c2}$, after which Π_{edge} rapidly decreases to zero, as does J_{edge}. On each plot are shown vertical reference lines for the transition fields of rows of vortices, where different behaviour of Π_{edge} is observed. Considering $w = 6\xi$, after the first vortex/row enters (n=1), Π_{edge} continues to increase in general, with the typical peaks in Π_{edge} associated to vortex entry increasing with H up to $\Pi \simeq 1\Pi_0$ at $H = 0.64H_{c2}$, after which the maxima saturate at $\Pi_{edge} \simeq 0.84\Pi_0$ for higher H.

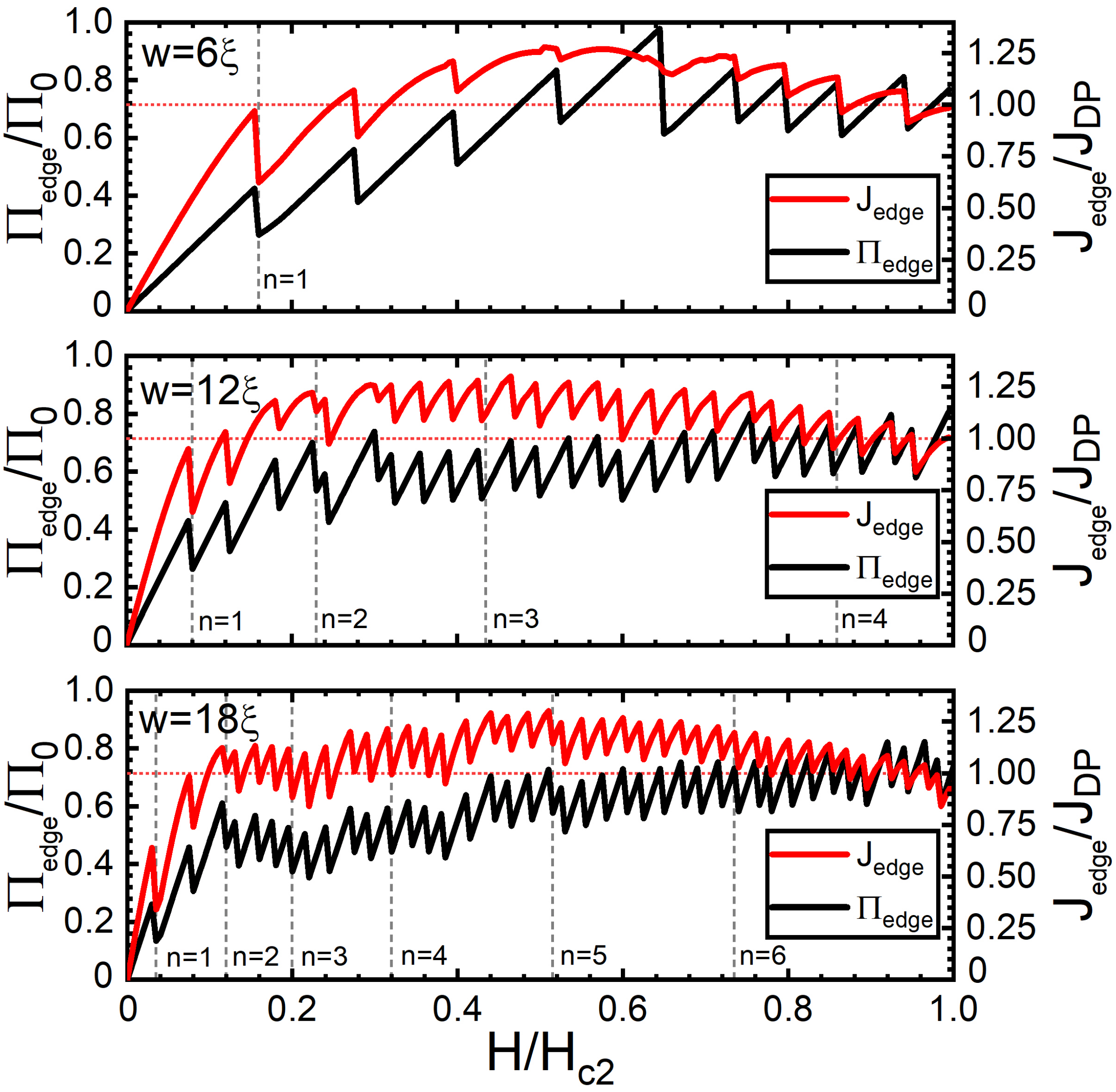

Figure 3.4: Ground state supervelocity and current density at the nanostripe's edge versus the applied magnetic field in the ground state for widths $w = 6$, 12, and 18ξ. The horizontal red dotted-line is a reference for the depairing current density, J_{DP}, and the grey vertical dashed-lines indicate the transitions to a state with an additional vortex row ($n \to n + 1$).

For $w = 12\xi$, between the transition of n=1 and n=2 rows, there continues the initial steep general increase of Π_{edge}, peaking at $\Pi_{edge} \simeq 0.70\Pi_0$, at which the peaks in Π_{edge} saturate at $\simeq 0.72\Pi_0$. There is no clear behaviour linked directly to the transition of new vortex rows. However, when $w = 18\xi$, the same general steep increase of Π_{edge} is observed, up to the transition of n =2 ($H \simeq 0.12H_{c2}$), at which point Π_{edge} tends to increase with H, saturating around $\Pi_{edge} \simeq 0.72\Pi_0$. The saturation observed evidences a maximum value of the supervelocity for ground states, where $\Pi_{edge} \simeq 0.72\Pi_0$. Simulations suggest that Π_{edge}^{max} increases for very narrow stripes ($w \lesssim 6\xi$) emphasising confinement, and weakly depends on H as previously observed [39]. Additionally, the values of the peaks in Π_{edge} associated to the nucleation of vortices increases rapidly with H at low H, then tends to saturate to a maximum value at large H.

3.3 Organisation of vortex rows

Due to vortex interactions with other vortices, and material boundaries, it is intuitive to assume there will be an arrangement of the vortex lattice to minimise the free energy in the system. Abrikosov famously predicted the existence of vortices and showed that in type-II superconductors, vortices would arrange in a square lattice, with lattice parameter $a_{\Box} = \sqrt{\frac{\Phi_0}{B}}$ [59]. However, it was experimentally proven that vortices arrange in a triangular lattice [161], and correction to the original derivation of Abrikosov showed the lattice parameter is $a_{\triangle} = 1.075\sqrt{\frac{\Phi_0}{B}}$. This type of triangular lattice occurs in superconductors where the dimensions are large enough that boundary effects can be ignored. Reducing the dimensionality of a superconductor can significantly change its behaviour, for example reducing it from 3D to 2D cross-over, effects such as a maximum in the critical current density can be observed [25]. Reducing the lateral dimensions affects the vortex pinning regime of narrow 2D superconductors, such that edge pinning effects dominate over bulk pinning [34, 156], emphasised in narrower stripes. Such pinning potentials produced by edge Meissner currents affects the static configurations of vortices [44], as seen in figure 3.5. A consequence of confinement forces and vortex interactions is the arrangement of vortices and organisation into a numbers of rows of vortices, depending on the width and applied magnetic field.

In figure 3.5 we present our novel result of a vortex row phase diagram produced using the SGL approach, showing the conditions for the formation of a number of vortex rows, n, as a function of H and w of the SN [44]. Each dashed curve in the diagram shown in figure 3.5, plotting the width of the SN versus H, represents the appearance of the n^{th} vortex row ($n = 1 - 5$) in the ground state of the system as magnetic field is increased. Examples of corresponding vortex configurations for a SN of $w = 12\xi$ for different H intensity are shown in figure 3.6, corresponding to the pinpointed dots (labelled a-h) in figure 3.5. To identify the threshold H for the transition to the vortex row configuration with a higher n, the ground states were first obtained for each SN at different H; then the spatial distribution of the superconducting order parameter $|\Delta|^2$ has been plotted (similar to figure 3.6) and carefully analysed, focusing on the geometrical interpretation of the vortex configuration. In the SGL approach adopted in these simulations, the SN was considered periodic along its length, with a unit cell of $L = 32\xi$. Several checks, carried out by extending the unit cell length till 80ξ, have confirmed all following results.

In a SN, the early theoretical works [165, 162] have shown that the magnetic field at which the surface barrier is suppressed and a single vortex can be stable in the SN is $H/H_{c2} = \pi^2\xi^2/2w^2$. The subsequent experimental observations of vortex penetration fields by Stan

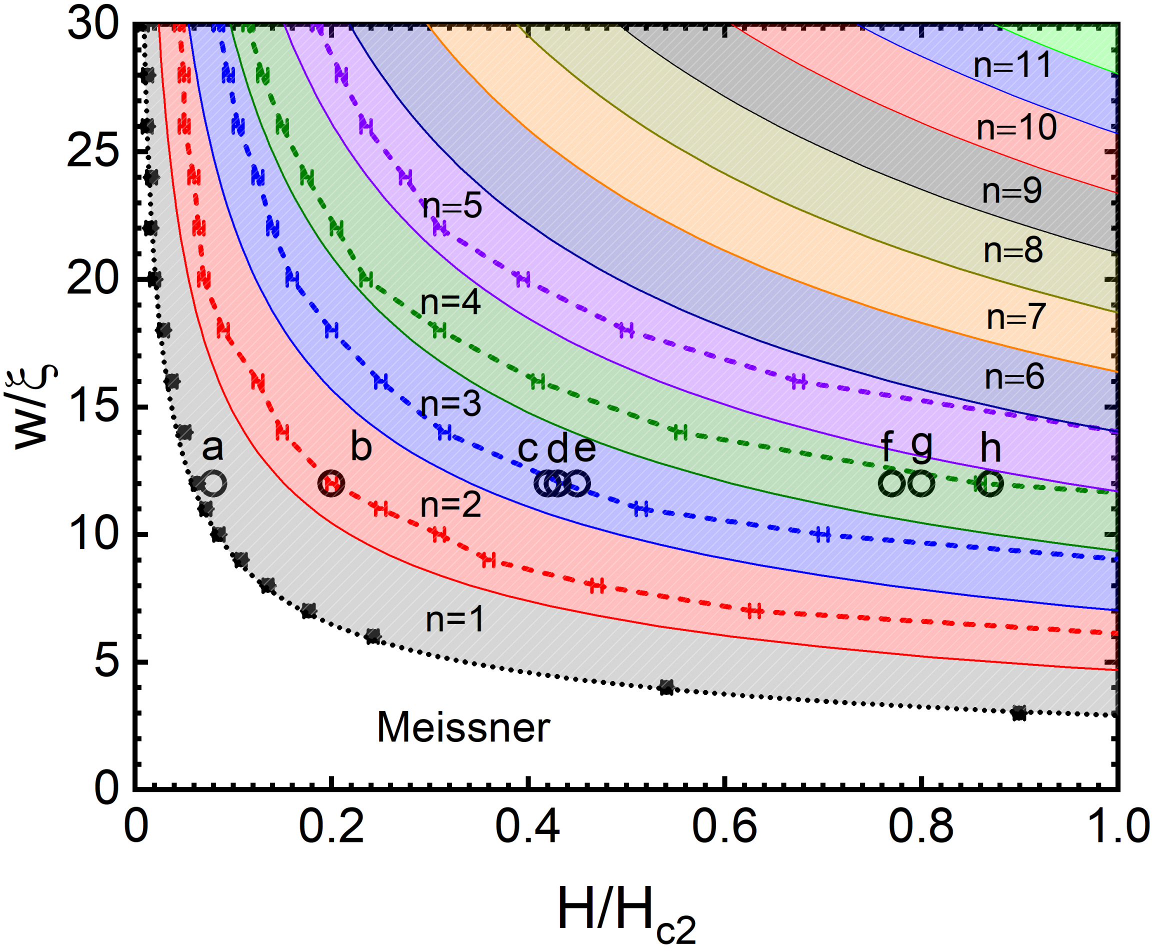

Figure 3.5: Equilibrium vortex-row phase diagram, plotting the SN width (in units of ξ) as a function of the applied magnetic field intensity (in units of H_{c2}), for different numbers of formed vortex rows (n). Simulations have been done using the SGL approach with periodic boundary conditions along the length, with unit cell length of $L = 32\xi$. The dashed lines denote the threshold for the formation of an additional vortex row (here shown up to $n = 5$). The coloured regions represent the approximated regions for $n > 1$, delimited by solid lines given by expression $H_{row}/H_{c2} = \frac{\pi n^2 \xi^2}{\sqrt{3} w^2}$. Circles, labeled $a - h$, relate to the vortex configurations shown in figure 3.6. Black dotted line corresponds to the analytical expression $H/H_{c2} = K \frac{\pi^2 \xi^2}{2w^2}$ [162], with $K = 1.7$ [163].

et al. [163] have shown a very good agreement with latter expression, up to a multiplying constant K. Our numerical data (black dots in figure 3.5) reconfirm that finding, as vortex penetration fields were found to nearly ideally match the same functional dependence on w, with a multiplying constant $K = 1.7$.

The approximate criteria for further reconfiguration of the vortex states and appearance of additional vortex rows can be obtained in the following way, considering a Abrikosov

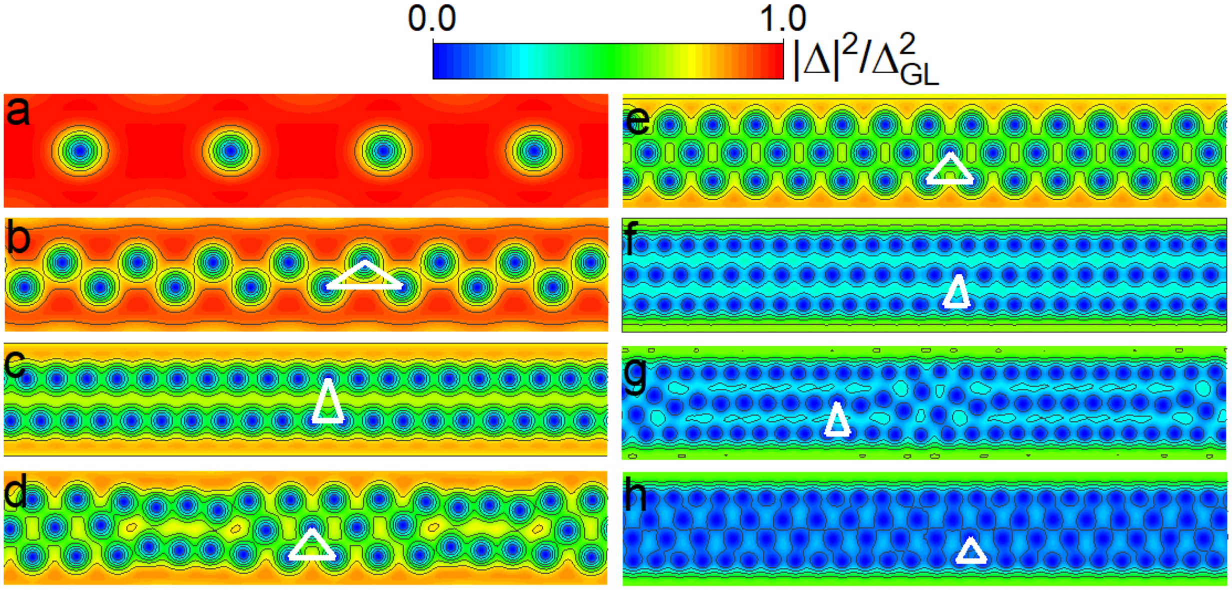

Figure 3.6: Calculated vortex configurations plotted as Cooper-pair density for the ground state of a SN of width $w = 12\xi$, in a periodic cell of $L = 64\xi$, at different applied H/H_{c2} values: (a) 0.08; (b) 0.20; (c) 0.42; (d) 0.43; (e) 0.45; (f) 0.77; (g) 0.80; (h) 0.87 (cf. figure 3.5). Panels (b), (d) and (g) depict the vortex states at the nucleation of a second, third and fourth row, respectively. Panels (c), (e) and (h) show the most lattice-like packing conditions for two, three and four vortex rows, respectively. White lines, connecting the cores of three neighbouring vortices, illustrate the deformation of the Abrikosov lattice [164] in the SN. Color bar denotes the values of the Cooper-pair density shown in the panels. Each depicted configuration is indicated in figure 3.5 with an open dot and is labelled accordingly.

triangular lattice, with the lattice parameter $a = 1.075\sqrt{\phi_0/H}$. The vortices are arranged in a body-centered hexagonal lattice, and so the Wigner-Seitz unit cell is hexagonal with a unit area per flux quantum of $A = \frac{\sqrt{3}}{2}a^2$. For a narrow SN, to accommodate n rows of vortices, the spacing, w_v, among vortex rows must obey the inequality $w_v \leq w/n$. Using the previous expression for the Abrikosov vortex density, we substitute $A = \frac{\sqrt{3}}{2}w_v^2 = \frac{\sqrt{3}w^2}{2n^2}$ to obtain the zeroth order approximation for the threshold magnetic field required for the formation of new rows, yielding $H_{row}/H_{c2} = \frac{\pi n^2 \xi^2}{\sqrt{3}w^2}$. Those approximate threshold H values are shown in figure 3.5 by the solid lines delimiting different coloured regions, indicating transitions among states with different number of vortex rows. In general, the behavior of threshold H found using SGL simulations agrees well with the formula prediction. The values were however mostly higher than the approximate ones, which is attributed to the role played by the edge barriers for vortex entry and exit (varying, depending on w and H). In addition, the rearrangement of the vortex lattice with every vortex penetration is not taken into account in latter basic analytical formula. Note that such effects of the vortex-vortex interactions and interactions with the edge Meissner currents (causing the confinement force), dominate the formation of the vortex configurations in narrow SNs and present the main point of interest in this work.

For a SN of $w = 12\xi$, figure 3.6 shows different vortex-row configurations, as formed in the ground state at different H values (marked by open dots in figure 3.5). After formation and growing of the first vortex row population (figure 3.6-a), increasing H, vortices rearrange into a closely packed "zig-zag" state (figure 3.6-b). This close packing is emphasised by a white triangle progressively deviating from the equilateral shape expected in the Abrikosov vortex lattice, with rise of H. Obviously, in this state the Meissner currents will exert a strong repulsive and confining force on the vortices from the SN edges (i.e. strong Bean-Livingston edge barrier [27]), resulting in a vortex spacing far smaller than the above rough analytical estimates (leading to the solid lines in figure 3.5).

Starting from the one row configuration (figure 3.6-a), raising H and n further, strengthens the relevance of the vortex-vortex interaction forces on the resulting vortex configuration, which will increase separation between the two rows (figure 3.6-c). At this point, it's observed that additional vortices in the SN cannot uniformly balance the aforementioned competing force in the entire SN, leading to a local rearrangement of the vortex lattice to three rows (figure 3.6-d). Only with further increasing field and having enough vortices in the SN the full three-row state is formed (figure 3.6-e; notice a nearly ideal triangular lattice formed). For the considered width of the SN, the state with 3 vortex rows persists to a much larger field due to quantum confinement, such that vortices very strongly overlap in a closely packed structure (figure 3.6-f). Nevertheless, in the vicinity of the bulk upper critical field a fourth row forms, first locally (figure 3.6-g) and eventually in the entire SN (figure 3.6-h), before superconductivity is destroyed. No further rows of vortices can form at higher field and the existing vortex rows increasingly overlap until the normal state is established.

The narrow stripe of $w = 12\xi$ showed deviations from the theoretical vortex-row transition fields H_{row} when ignoring edge confinement effects, originating from the Meissner edge barrier. Significant deviations of these fields for different width of stripes (figure 3.5) evidence significant effects caused by strong interactions between vortices and the edge Meissner barrier. It is interesting to notice how the unit cell of 3-vortices highlighted by the white triangle changes it's shape as the vortex density increases. When two rows form initially the edge barrier dominates and deforms the predicted equilateral triangle lattice from the stripe's edge, leading to an isosceles triangle. As the density of vortices increases in two rows the regular triangle is now deformed from the sides, which is due to an increases in vortex density and the vortex-vortex interactions. When the third row locally forms the isosceles-like triangle lattice relaxes back to a more equilateral triangle (figure 3.6-d). Slightly increasing the field, realising the new fully formed 3 rows, the triangular unit cell demonstrates an equilateral form (panel-e). Again, increasing the vortex density further leads to deformation of the equilateral triangular form to an isosceles, seen in panel-f. The transitions between rows of vortices and the arrangement in the lattice are strongly affected by competition of the two forces, vortex-vortex and edge current interactions. In fact as the magnetic field is increased the edge Meissner current also increases in order to shield the superconductor.

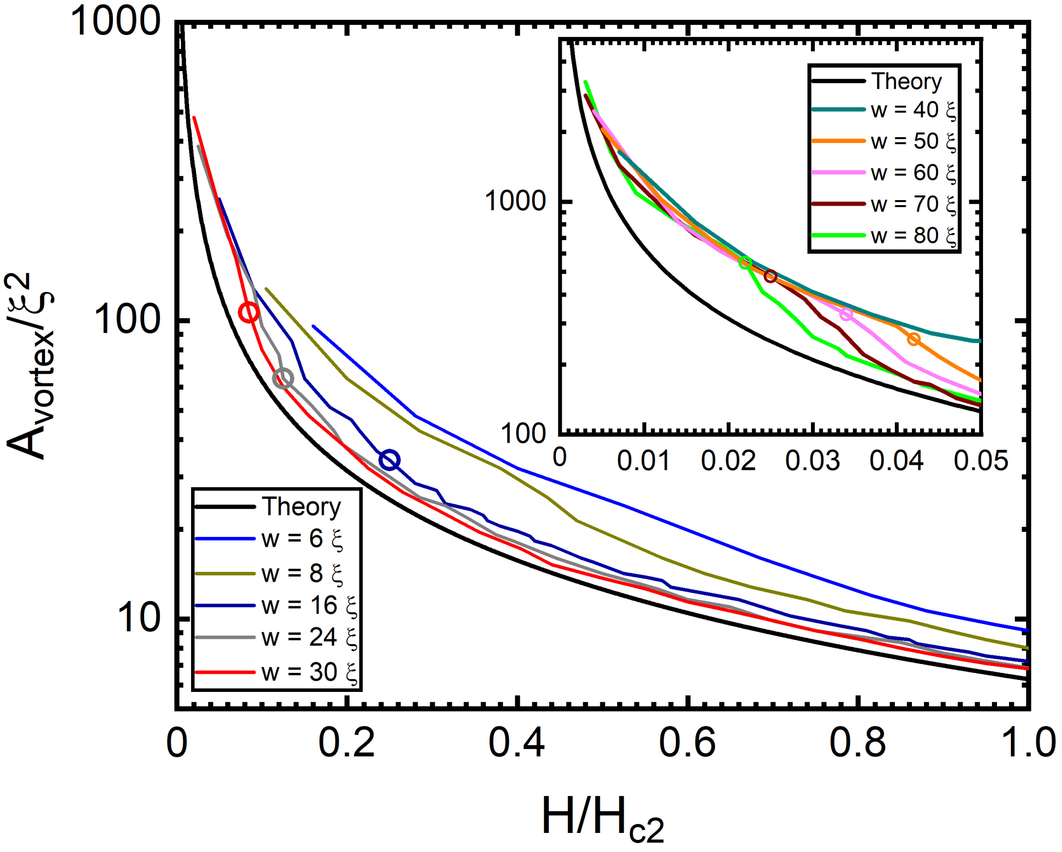

Figure 3.7: Area of the Wigner-Seitz unit cell containing a single vortex, as a function of the applied magnetic field, for SN of width $w = 6 - 30\xi$, and $w = 40 - 80\xi$ in the inset for small H values. The analytical expression for the Abrikosov vortex lattice (AVL) area, $\frac{A}{\xi^2} = 2\pi\frac{H_{c2}}{H}$, is plotted as a black line. Open dots in each curve indicate the H intensity for formation of the third vortex row, above which the curves progressively approach the AVL expression, upon increasing the w.

However, in type-II superconductors penetration of vortices decreases the strength of the Meissner field at the edge as vortices enter, as was discussed in relation to supervelocity in a previous section. As H is increased, the Meissner field is increased further, until the field is strong enough to penetrate with more vortices. Therefore, there are not only competing forces, but the forces are also affected by the penetration of additional magnetic flux lines. The described process is more significant for stripes with smaller widths which also manifests itself in the vortex density discussed next.

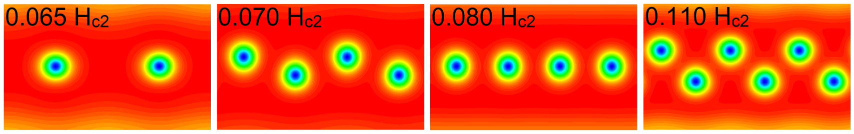

Figure 3.8: Spatial distribution of the superconducting order parameter for a SN of $w = 20\xi$, at increasing values of magnetic field, shown in each panel in units of H_{c2}. An example of the transition from a single row to a second row, followed by reconfiguration back to a single row due to strong confining effects as a result of the edge Meissner current.

3.4 Confinement and vortex density reduction

As the magnetic field is increased, vortices penetrate the stripes of different width, and vortex rows are formed, one can expect a gradual evolution from the quasi-1D row pattern into a 2D vortex lattice. To evaluate such transition the average area occupied by a single vortex in all the states can be found. The number of vortices present are counted, and divide by the stripe's area ($w \times L$) to obtain a value for the average area occupied by a single vortex, another novel result we present [44]. This is plotted in figure 3.7 as a function of applied magnetic field, in comparison to the expected behavior of the Abrikosov vortex lattice. The strongest confinement in narrowest nanostripes [33, 27] dominates the vortex-vortex interaction, leading to compression of vortices into fewer vortex rows and consequently larger average area per vortex in the stripes. This can be clearly seen in figure 3.7 for widths $w \leq 8\xi$. As the width of the stripe is made larger, the confining force from the edge current (at a given magnetic field) becomes less dominant with respect to the vortex-vortex interaction, resulting into progressively closer agreement with the expected behaviour of a triangular vortex lattice [164], a tendency clearly visible upon formation of the third vortex row (indicated by open dots in figure 3.7).

It must be emphasised that the transitions between rows of vortices and the final arrangement of vortices in the lattice are strongly affected by competition of the two forces, both dependent on applied magnetic field. As the magnetic field is increased the edge Meissner current also increases, up to the penetration of new vortices, while every new vortex changes the landscape of the vortex-vortex interactions in the stripe. As exemplified in our unique result shown in figure 3.8 for the case of $w = 20\xi$, this nontrivial balance of competing forces can lead to a re-entrant behavior in terms of the number of vortex rows formed [44]. Namely, in such cases, the zig-zag instability of the vortex row upon certain vortex density is reached can be "cured" by the increasing Meissner currents and lateral confinement growing with increasing magnetic field, before the additional penetrating vortices tip the scale in favor of vortex interactions and definite reconfiguration into a state with an additional vortex row. This re-entrant behavior has been observed for nearly all considered stripe widths in the range $w = 20 - 60\xi$. In such cases the first onset of the zig-zag instability identifies the $n \rightarrow n + 1$ transition in figure 3.5. It can also be claimed that this range of widths where such strong edge effects are detected marks the crossover from the quasi-1D to a 2D film-like behavior [44].

Chapter 4

Consequences of Synchronous Vortex Row Crossings in Current Carrying Nanostripes

When a transport current is applied across a thin and narrow superconducting film or stripe ($d << \lambda, \xi$) in the absence of an external magnetic field, the current is distributed uniformly across the stripe [156, 166]. The induced magnetic field scales with $1/\kappa^2$, as a result in extreme type-II superconducting narrow wires, this field is negligible. However, work on this induced field affects the critical current in the absence of magnetic field, was shown to scale with H_{c1}/λ [167, 168]. When $H > H_{c1}$, and vortices penetrates a SN, a small applied transport current will shift the vortices across the stripe from the Lorentz force experienced by the perpendicular penetrating magnetic flux ($\mathbf{J} \times \mathbf{B}$), and continue to be trapped by the edge pinning barrier [169] . At a critical current density, J_{c1}, the vortices have enough energy to cross the edges barriers [34]. Once J_{c1} is exceeded vortices continuously cross the stripe, and under certain conditions cross with a periodic fashion, creating detectable pulses in the voltage drop across the stripe [44] (see figure 4.3). In chapter we present a variety of results, some cover existing and well known concepts such as different resistive states of SNs and their characteristic V-J curve. The main focus here is the phenomena of synchronous vortex crossings and mainly the transition from asynchronous vortex crossings, which are novel results presented in this thesis and reported in [44].

Throughout this chapter the generalised time-dependent Ginzburg-Landau formalism (gTDGL) [170, 144] is used to study the dynamical properties of the superconducting condensate of a nanostripe in the high-κ limit (with order parameter $\Delta(\mathbf{r}, t)$), in the presence of an external magnetic field $\mathbf{H}$ (with vector potential $\mathbf{A}$) and sourced current density $\mathbf{J}$, given by

$$\begin{aligned}\tau_{GL} N(0) \frac{u}{\sqrt{1-(\Gamma|\Delta|)^2}} &\left[\frac{\delta\Delta}{\delta t} + i\tfrac{e^*}{\hbar}\varphi\Delta + \left(\frac{\Gamma}{\sqrt{2}}\right)^2 \frac{\delta|\Delta|^2}{\delta t}\Delta\right] \\ &= -\left(a+b|\Delta|^2\right)\Delta + \frac{\hbar^2}{2m^*}\left(\nabla - ie^*\mathbf{A}\right)^*\Delta,\end{aligned} \tag{4.1}$$

$$\nabla^2\varphi = \nabla\left[Im\left\{\Delta^*\left(\nabla - i\mathbf{A}\right)\Delta\right\}\right], \tag{4.2}$$

where $a = \frac{\alpha}{2m^*\gamma}$, $b = \frac{\beta}{4m^{*2}\gamma^2}$, and $\Gamma = \frac{2\tau_i}{\hbar\sqrt{2m^*\gamma}}$. The Ginzburg-Landau order parameter relaxation time is τ_{GL}; $N(0)$ is the density of states at the Fermi level; the parameter $u = 5.79$ in conventional superconductors; e^* is the effective charge; φ is the electrostatic potential; τ_i is the electron-phonon inelastic scattering time and α, β, γ are material parameters. Equation 4.1 is solved coupled with the equation for the electrostatic potential (eq.4.2), adopting a gauge $\nabla \cdot \mathbf{A} = 0$, using Neumann boundary conditions at all sample edges, except for the leads where sourced current is injected, where $\Delta = 0$ and $\nabla\varphi = \pm J$. This theory is derived for dirty gapless superconductors, where Cooper-pair breaking occurs due to strong inelastic electron-phonon scattering, and the physical quantities Δ and A must relax over a time-scale much longer than τ_i. The distance over which an electric field can penetrate into the superconductor, and the length over which relaxation processes occur is given by the characteristic inelastic diffusion length $L_i = \sqrt{D\tau_i}$, where D is the diffusion parameter proportional to the electronic mean-free path. In cases where $L_i << \xi$, our simulations require very fine grid spacing (reflecting in consequently smaller time step in the used implicit Crank–Nicolson method) to yield physically correct results. In general, superconducting materials at T close to the superconducting-to-normal transition temperature, T_c, satisfy the conditions for slow temporal and spatial variations ideally required for the applicability of the GL formalism. In the TDGL formalism, distances are given in units of $\xi(T) = \xi$; time in units of $\tau_{GL} = \frac{\pi\hbar}{8k_BT_c(1-T/T_c)u}$; temperature is in units of T_c; the order parameter Δ in units of $\Delta(0) = 4k_BT_cu^{1/2}(1 - T/T_c)^{1/2}/\pi$; φ in units of $\varphi_{GL} = \hbar/e^*\tau_{GL}$; vector potential A is scaled to $A_0 = H_{c2}\xi$ and current density to $J_0 = \sigma_n\varphi_0/\xi$. The simulations are performed irrespective of the temperature T/T_c, all physical quantities are scaled and normalised by reference quantities at a given temperature. Note that, even though the GL approach is formally valid close to T_c, experiments have shown the possibility to extend the GL predictions to a finite T range below T_c, see, e.g., ref. [25] and references therein. Moreover, in the simulations the heat generated by the Joule effect is lost on a time scale shorter than the inelastic scattering time, assuming that the heat transfer coefficient is large enough to allow a fast dissipation. The approach adopted is equivalent to include a solution of the thermal balance equation [46]. Our findings are valid at any temperature providing the coherence length is known at a given temperature.

4.1 Vortices in current-carrying narrow superconducting nanostripes

The TDGL approach allows to also simulate the voltage-current density (V-J) characteristics of SNs, presented in figure 4.1 for stripes with w = 6, 9, 12, 18ξ, under an applied magnetic field $H = 0.25H_{c2}$. Analysis of the V-J characteristics reveals a number of features related to different resistive regimes in each curve. At low J values, stationary vortices are shifted to a new position across the SN due to the Lorentz force produced by the sourced current, so the

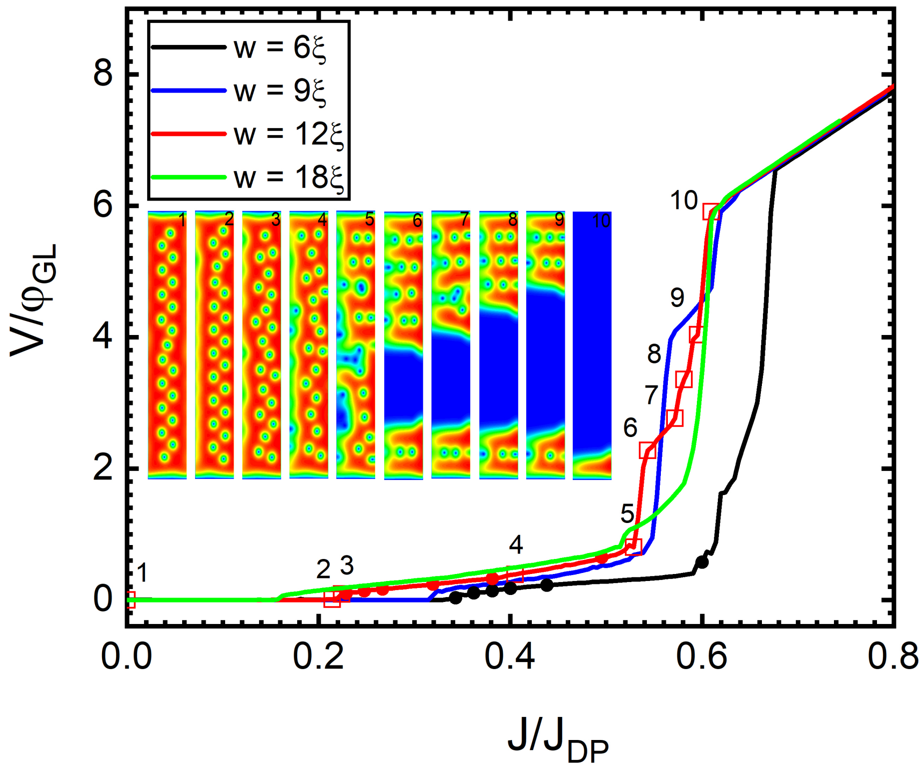

Figure 4.1: Normalised voltage drop as a function of the normalised current density, for SNs of width $w = 6$, 9, 12, and 18ξ, at magnetic field $H = 0.25H_{c2}$. The black and red dots (for $w = 6$ and 12ξ respectively) mark the values of current density at which analysis of the modulation frequency spectra is presented in figures 4.4 and 4.6. Inset: Snapshots of the Cooper-pair density for SN of $w = 12\xi$, numbered 1-10 from left to right, are indicated by open red squares.

resulting voltage drop and resistance remain zero. An example of such can be seen in figure 4.1 (for $w = 12\xi$) from the states labelled 1 and 2. When J_{c1} is reached, vortices cross the SN and their perpetuous motion leads to a finite resistivity value. Snapshots of this flux-flow regime can be seen from the states labelled 3 and 4 in figure 4.1. With further increasing J and in presence of vortex-vortex interaction forces, a SN in the dissipative state exhibits flux-flow instability, where vortex cores interact during dynamics and ordered lattice structure is lost during motion (state labelled 5 in figure 4.1). At even higher J, vortices align during motion, in a slip-streamed geometry (vortices tailgate, i.e. subsequent vortices crossing the SN, move in the wake of the previous vortex [45, 47]), before a Langer-Ambegaokar phase slip [171] occurs across the SN. The normal area covered by the phase slip grows laterally with further increasing J, and additional steps in the V-J curve appear with every slip-stream being merged with the growing phase-slip, as seen in the states labelled 6-10 in figure 4.1.

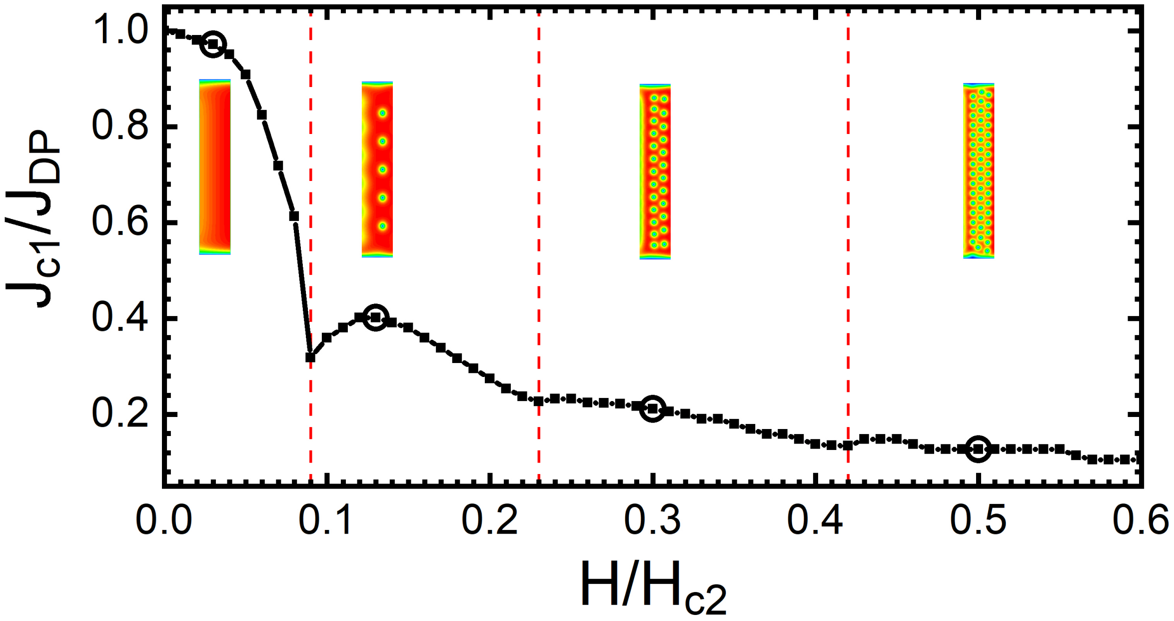

Figure 4.2: First critical current density normalised to $J_{DP} = 0.385J_{GL}$ as a function of the applied magnetic field normalised to H_{c2}, for a SN of width $w = 12\xi$, obtained using the TDGL approach. Vertical red lines mark the transition to 1, 2 and 3 vortex-row states, at a magnetic field of $H/H_{c2} = 0.09$, 0.23, 0.42, respectively. Insets illustrate the vortex row configurations at selected magnetic fields (marked by open dots) for sourced current density just below the critical one.

When J reaches roughly $0.65J_{DP}$, the SN transitions to a fully normal state, with linear ohmic behavior.

Similar V-J curves have been observed both numerically [159] and experimentally for Nb-C microstrips, fabricated using focused-ion-beam-induced deposition [49]. In real materials, the presence of disorder and defects changes the behavior described in this work. For example, edge defects are a favorable point for vortex entry as current crowding occurs in the local defect region leading to favored positions for vortex penetration. In addition, disorder on length scales larger than ξ may create bulk pinning regions [33]. On the other hand, small disordered regions (smaller than ξ) leads to increased inelastic scattering times, resulting in finite values of Γ. Hence, a viscous condensate will be formed, changing the dynamic behavior of vortices and introducing additional resistive states such as “vortex channels”. The appearance of such resistive states can be advantageous for EM emitters, providing synchronization of vortex rows which is discussed next in the case of negligible disorder and defects.

4.2 Critical current, pinning, and defects

Transport currents in thin and narrow superconducting nanostripes manifest from a complex interplay of surface and bulk pinning. Very narrow stripes exhibit strong pinning forces, determined almost predominantly from the surface barrier [137, 34, 32, 172, 173], whilst wider stripes experience bulk pinning forces [169, 174, 175, 176] due to vortices being trapped "deep" ($d \gg \xi$) inside the superconducting geometry. In the intermediate regime, the two types of pinning interact, which affects the behaviour of J_c with respect to the number of rows resulting from an external magnetic field. The critical current exhibits non-monotonic behaviour of J_c during the transition to higher rows of vortices as H is increased [34, 33] (see figure 4.2). The increase of $J_c(H)$ during the appearance of a disperse vortex row (spacing $a \gg \xi$) was predicted by Schmidt [177], shown numerically with TDGL simulations [34, 33, 44], and observed experimentally [178]. Vodolazov provided an explanation [34] to this behaviour by showing at $H > H_{c1}$, J_c increases and the resistance $R(H)$ decreases, until the intervortex distance becomes smaller than w. The increase followed by decrease of $J_c(H)$ at higher fields can be explained by the same mechanism, but during the transition to a new row of vortices the transverse intervortex distance increases. This can be seen with the example of a stripe width $w = 12\xi$ (see figures 4.2,3.6). It was shown [33] how an optimised distribution of defects can enhance critical current in typical mesoscopic superconducting stripes. The interplay of edge and bulk pinning forces also affect vortices in the static case, where the configuration of the vortex lattice organises into n-rows depending on w and n [44]. Additionally, it was observed a transition from $n = 1 \to 2 \to 1 \to 2$ rows of vortices [44] (see figure 3.8), for width $w \simeq$ 20-60ξ, as a result of the competition between edge and bulk pinning.

Flux pinning [179] involves the trapping of a vortex as a result of the energetically costly normal core preferring positions where superconductivity is already suppressed. Stronger pinning means a higher critical current can be applied, at a given magnetic field, before vortices start moving and cause energy dissipation. Carefully engineered artificial pinning landscapes, such as artificial magnetic structures [180] and antidots [181], provide strong confining forces, amplifying J_c. Even the inclusion of a magnetic strip on top of a superconducting strip, magnetized in a specified direction enhances J_{c1} [182]. The work of ref. [181] discusses the critical current as a function of the magnetic field for a superconducting film containing an array of antidots (holes/insulator). The magnetic field is given in units of H_1, which is the minimum field value at which each hole contains 1 vortex, occurring when the pinning landscape is commensurate with the vortex lattice, producing an increase in J_c. In fact, there is an amplification of J_c at each integer multiple of H_1, where sub-lattices of vortices at pinned at interstitial positions, and detected experimentally [183].

Defects at the nanoscale are common, as fabrication processes often realise specimens with edge defects in the form of protrusions/indentations [49, 184], non-uniform edges [185, 186], surface defects [33], inclusions and grain boundaries [187, 188]. In general defects are detrimental to typical functionality of superconducting nanostripes, inducing flux flow instability such as vortex jets [185], but in some cases can enhance critical current [33]. Therefore, when considering narrow superconducting stripes for their enhanced critical current, it is important to consider the unavoidable defects, and their impact on the desired superconducting properties.

4.3 Vortex-lattice crossings

In the dynamic phase when vortices cross a narrow superconducting nanostripe a disturbance occurs in the electric and magnetic field, as a result electromagnetic radiation radiates into free space, with harmonics of the washboard frequency, $\nu_0 = v/a$ (v is velocity and a is the lattice spacing in the direction of motion) [42], up to the superconducting gap energy ($\Delta/\hbar$). The washboard frequency was first observed in IV characteristics of a superconducting aluminium film [189], and with similar observations made in high T_c-superconductors [190, 191]. It was shown how the frequency distribution of the radiated intensity exhibits a maximum at microwave frequencies around $\nu \simeq v/\lambda$, and how coherent motion of a lattice leads to constructive interference and strengthening the radiated power per vortex by a large factor [192]. Interestingly when a nanoscale meandering stripe is exposed to an external magnetic field and a sufficient applied transport current ($H > H_{c1}$, $J > J_{c1}$), vortices cross the consecutive stripes (as part of the meandering structure), emitting EM radiation with frequencies of 100's MHz [193]. In similar work, lattice of vortices crossing a superlattice of Mo/Si emitted detectable radiation with frequency up to 50GHz [43]. In the above studies it is readily noted that synchronised vortex crossing amplify the emitted radiation. The following section includes an investigation into how vortices cross narrow nanostripes, where transitions between quasi-synchronous, synchronous and asynchronous regimes occur.

4.3.1 Synchronous vortex-row crossings

In a thin and narrow superconducting geometry the vortices that cross must compete with strong effects at the edge of the stripe, influencing the behaviour of their crossing, as has been evidenced in this thesis. Figure 4.3 shows $V(\tau)$ across the stripe with $w = 6\xi$, at $H = 0.25H_{c2}$, for different J, along with the spatial distribution of the superconducting order parameter, using the TDGL approach [44]. Each panel shows modulation in $V(\tau)$ as a result of vortex crossings, with their corresponding spectra of frequencies shown in figure 4.4, obtained via FFT of $V(\tau)$. As vortices cross the stripe, modulations in the voltage drop across the stripe occur. The specific modulations depend heavily on the synchronisation of vortex crossings, which affects the spectrum of frequencies present in such modulations. In figures 4.3-4.6 we show the voltage as a function of time, $V(\tau)$, at different sourced currents, and their corresponding spectra of frequencies (obtained by FFT of $V(\tau)$) for stripes of width 6ξ and 12ξ, both with an applied magnetic field of $0.25H_{c2}$. The TDGL approach has been used to find the ground states for each stripe at $H = 0.25H_{c2}$, then the current is swept from 0 up to $J \simeq J_{DP}$ in steps of $dJ = 0.026J_{DP}$. At each current step the simulation has been left to run for a long enough time that a dynamic equilibrium has been reached ($\tau = 5 \times 10^3\tau_{GL}$), at which point the acquisition of data is recorded. The voltage drop as a function of time,

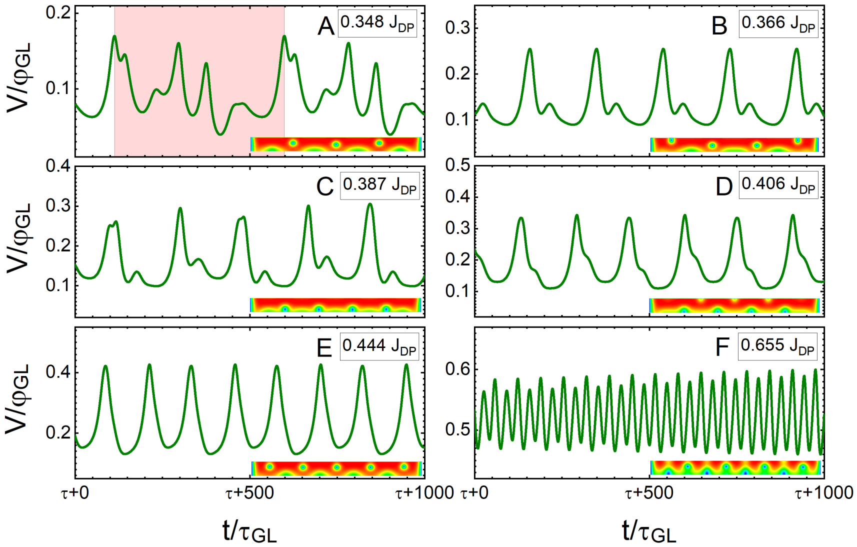

Figure 4.3: Normalised voltage drop as a function of time (normalised to τ_{GL}), for a SN of $w = 6\xi$ under a magnetic field of $H = 0.25H_{c2}$ sourced with different current densities of: (A) $0.348J_{DP}$, (B) $0.366J_{DP}$, (C) $0.387J_{DP}$, (D) $0.406J_{DP}$, (E) $0.444J_{DP}$, and (F) $0.655J_{DP}$. Each panel contains an illustrative snapshot of the spatial distribution of the Cooper-pair density during the dynamics. Red vertical segment in (A) shows the periodicity of the spectrum.

along with the spatial distribution of the superconducting order parameter at each time step are used to produce figures 4.3 and 4.5. In the dissipatitive state, as vortices move across the stripe there is an increase in the voltage across the stripe, with maxima corresponding to the exit of a vortex (where supercurrent density is highest). This leads to the modulation of $V(\tau)$, seen in figures 4.3 and 4.5. Firstly we consider the stripe of width $w = 6\xi$, figure 4.3-panel A shows $V(\tau)$ for the sourced current density of $J = 0.348J_{DP}$, which is the lowest current value that will cause vortices to cross the stripe.

The plot shows several features due to asynchronous vortex crossings, but a repeating sequence with a period of 486 τ_{GL}. Even though the vortices are not crossing in synchronised rows, there is some quasi-synchronised behaviour manifesting in the repetition of vortex crossing. As J is increased from $0.384J_{DP}$ to $0.406J_{DP}$ (panels A-D) the modulations in the voltage evolves, and the number of modulations caused by quasi-synchronous crossings reduces. At $J = 0.444J_{DP}$ (Panel E) there is only one mode that repeats periodically, which continues up to $J = 0.655J_{DP}$ (panel F), where there is only one significant single peak in the spectra. This is due to the strong Lorentz force at high current density which dominates the vortex-vortex and edge barrier interactions. However, the vortex-vortex and edge barrier interactions play a role in maintaining the vortex lattice structure.

The relative spectra of frequencies for the $V(\tau)$ plots can be seen in figure 4.4 in panels A-F. The repetition of vortex crossings with their particular configurations leads to peaks at specific frequencies. As the current density is increased the spectra show the evolution to a single repeating peak in the voltage. This can be seen by observing that the primary frequency component in each spectra becomes increasingly dominant. When $J = 0.348J_{DP}$ where the repeating quasi-synchronous crossing have a period of $\tau = 486\tau_{GL}$, the associated frequency is $\nu = 0.0021\tau_{GL}^{-1}$. This mode has the greatest contribution, whilst higher modes are associated to the period between individual modulations and higher order harmonics. The spectra is indicative of the strongly quasi-synchronous (overall repetition with multiple different modulations) dynamics of the vortex crossing. As J increases the number of different modulations decreases and the crossings become more synchronised, which is seen in $V(\tau)$ and emphasised by the different spectra. At $J = 0.444J_{DP}$ (Panel E) there is one mode with large contribution that repeats periodically, and continues up to $J = 0.655J_{DP}$ with a fundamental mode with frequency $\nu \simeq 0.03\tau_{GL}^{-1}$ (panel F).

To provide some idea of realistic values, consider Niobium thin films studied by Pinto et al., assuming they are still valid for SN of Nb. For a Nb film of thickness $d = 20$ nm the coherence length at zero temperature is $\xi(0) \simeq 8.0$nm [25], with Ginzburg-Landau time of $\tau_{GL}(0) \simeq 65$ fs. Considering modulations ranging between $\nu = 0.0021 - 0.03\tau_{GL}^{-1}$, for our niobium example this equates to $\nu = 1-50$GHz, which can be detected by conventional spectrum analysers. Such modulations have been observed experimentally in Mo/Si superlattices in the work of Dobrovolskiy [43, 193]. By fine tuning the geometry, faster vortex crossings could be envisaged and used as a terahertz radiation source, for a variety of applications [194], including clinical [195] and terahertz time-domain spectroscopy [196].

Similar behaviour can be seen from the stripe with $w = 12\xi$ under the same magnetic field of $H = 0.25H_{c2}$. Figure 4.5 shows the voltage drop across the stripe as a function of time. Panel A shows $V(t)$ at $J = 0.231J_{DP}$, when vortices start crossing the stripe causing dissipation. The vortices start crossing in a quasi-synchronous fashion at first (panel A), as was the case with the narrower stripe. However, the complete repeating sequence of vortex crossing occurs over a time $\tau \simeq 1500\tau_{GL}$, which is represented by the small contribution in it's relative spectrum (figure 4.6 panel A) of $\nu \simeq 0.0007\tau_{GL}^{-1}$. Whilst the largest contribution in the spectra corresponds to multiple vortex crossings repeating every $\tau \simeq 330\tau_{GL}$ with frequency $\nu = 0.003\tau_{GL}^{-1}$. When the current density increases from $J = 0.231J_{DP}$ to $0.327J_{DP}$ (panels A-D) vortex crossings evolve and become synchronised in the same fashion (similar to $w = 6\xi$). Where at $J = 0.327J_{DP}$ the fundamental mode has a frequency of $\nu = 0.006\tau_{GL}^{-1}$, which for the example of a thin niobium stripe is $\nu \simeq 9$GHz. However, when increasing the current density towards $J = 0.387J_{DP}$ (panel E) the onset of flux-flow instability occurs, becoming increasingly chaotic as current density is increased to $J = 0.504J_{DP}$ (panel F). At $J > 0.504J_{DP}$ a phase slip occurs and grows as current density is increases (figure 4.1, states labelled 6-10). Upon the transition to flux-flow instability the vortex crossing become asynchronous, which can be seen in $V(\tau)$ and is emphasised in the corresponding spectra where "small" line width contributions are absent, and instead there are noisy spectra. At

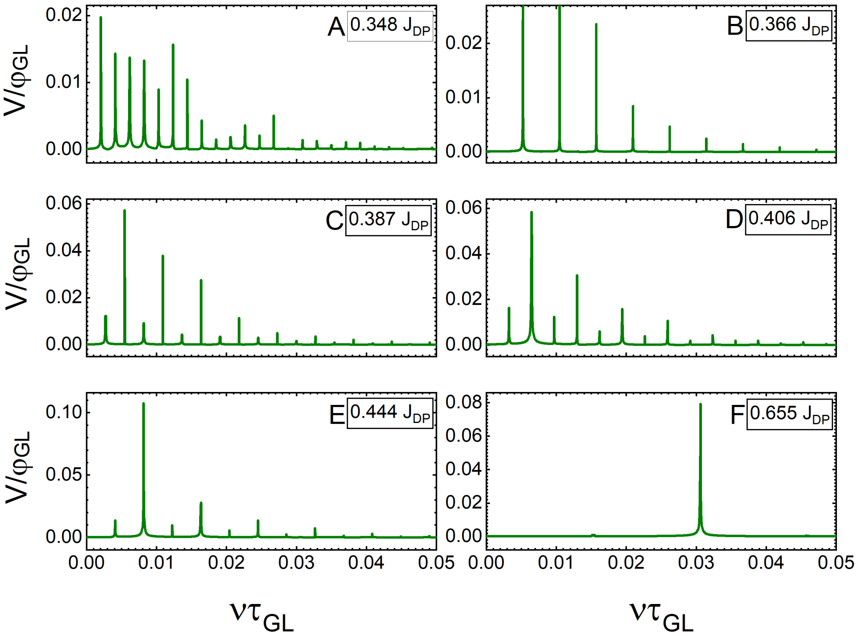

Figure 4.4: Spectra of modulation frequencies ν (normalised to τ_{GL}^{-1}) of the temporal voltage signals shown in figure 4.3.

$J = 0.387 J_{DP}$ there remains some coherency in the crossings, which leads to a broad peak in the spectrum (figure 4.6 panel E) around $\nu \simeq 0.007 \tau_{GL}^{-1}$. However, when J is increased further the crossing as completely asynchronous due to strong flux-flow instabilities, and this lead to a spectrum indicative of amplitude noise [44].

The spectra of frequency modulations shown in figure 4.6 for this stripe shows similar behaviour to that of the narrower stripe with $w = 6\xi$. At low current densities, when crossings are quasi-synchronous, we see larger contributions with many additional smaller peaks. As J increases and synchronicity improves and the smaller contributions associated to the quasi-synchronous behaviour disappear, whilst the frequency component with the largest contribution increases. We have seen similarities in both stripes as the current density is increased. In particular, both stripes begin the dissipatitive state with vortices that cross in a quasi-synchronous fashion as a result of vortex-vortex and edge barrier interactions dominating over the Lorentz force. Increasing the current density leads to strengthening of the Lorentz force, which gradually overpowers the prior mentioned vortex interactions, leading to the onset of synchronous crossings, in the form of complete vortex rows moving in unison. However, at larger J the smaller stripe continues to demonstrate synchronised crossings, whilst the wider stripe transitions to an asynchronous crossing [44].

The stripe with $w = 6\xi$ at $H = 0.25 H_{c2}$ (see figure 3.5) demonstrates a single row of

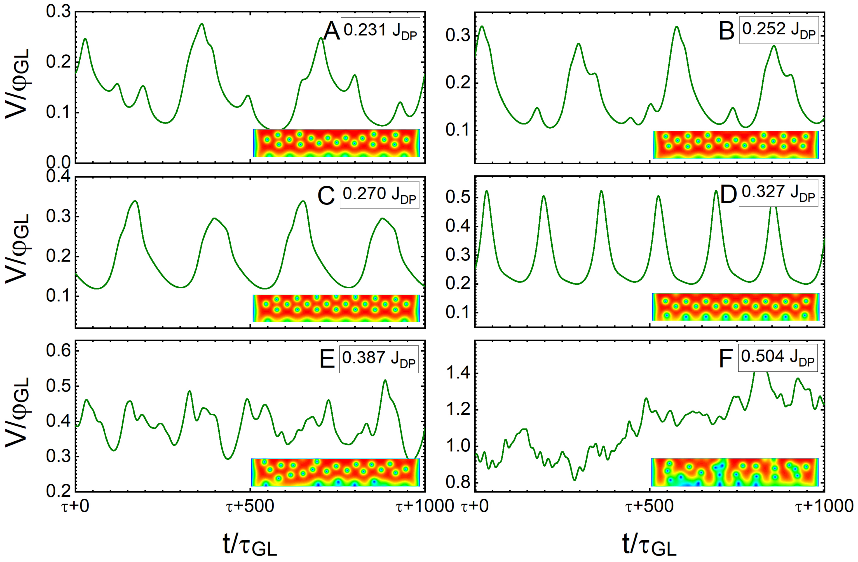

Figure 4.5: Normalised voltage drop as a function of time (normalised to τ_{GL}), for a SN of $w = 12\xi$ under a magnetic field of $H = 0.25H_{c2}$ sourced with different current densities: (A) $0.231J_{DP}$, (B) $0.252J_{DP}$, (C) $0.270J_{DP}$, (D) $0.327J_{DP}$, (E) $0.387J_{DP}$, and (F) $0.504J_{DP}$. Each panel contains an illustrative snapshot of the spatial distribution of the Cooper-pair density during the dynamics.

vortices in the static case, and a strong deviation from the theoretical limit of vortex density with area per vortex of $A \simeq 60\xi^2$ (see figure 3.7), due to the confinement forces (from the edge) dominating the vortex interactions. Whilst a SN with $w = 12\xi$ has a higher vortex density with area per vortex $A \simeq 40\xi^2$(see figure 3.7, leading to stronger vortex-vortex interactions, and under an additional Lorentz force begins flux-flow instability.

The speed of vortice can be obtained numerically by identifying a local minima and tracking their displacement at each time iteration. Results of the current density dependence of the vortex speed (see figure 4.7), evidence a linear dependence on J for low values. When J is increased towards values that will drive it into the normal state, the linear dependence is lost and there is a rapid increase in v [159, 197, 44]. This can be due to the quasiparticle spectrum changing from a superconducting to normal current when a vortex travels across the sample. At greater vortex velocity, quasiparticles switch more rapidly, increasing the rate that superconducting current is converted to normal current, increasing the annihilation rate of the superconducting order parameter. Give the range of velocities in figure 4.7, $v = 0.010 - 0.085\xi\tau_{GL}^{-1}$, for the example of thin niobium SN this equates to $v \simeq 1 - 10\text{kms}^{-1}$.

When the vortices are crossing synchronously the relation for the washboard frequency can be applied. With velocity and frequency of vortex crossing, the value for the lattice

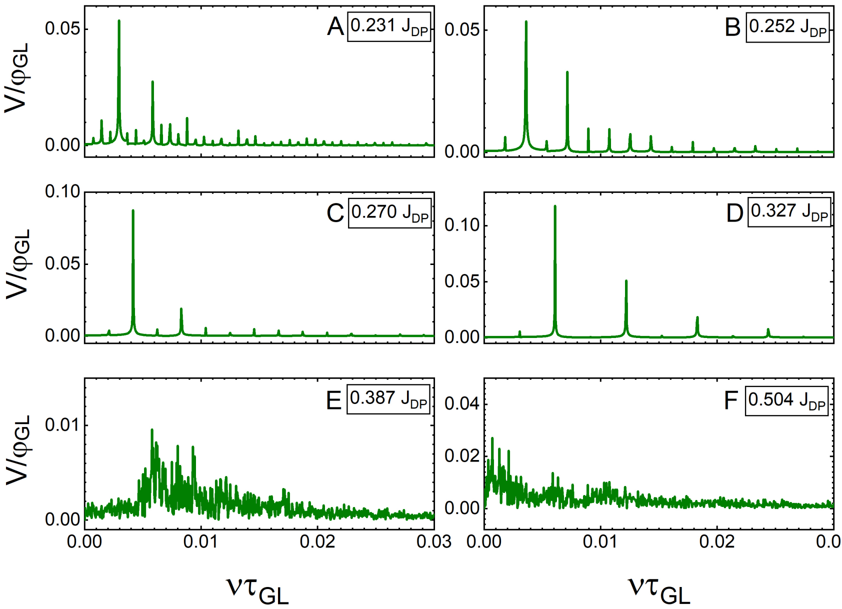

Figure 4.6: Spectra of modulation frequencies ν (normalised to τ_{GL}^{-1}) of the temporal voltage signals shown in figure 4.5.

spacing a can be obtained. Increasing the sourced current from J = 0.366 to $0.655 J_{DP}$, the values of the lattice spacing decreases from 6.2ξ to 2.8ξ. Two process are occurring, the energy barrier is lower and therefore vortex nucleation rate is higher, and the Lorentz force is stronger, the combination of the two act to reduce the size of the lattice parameter. A combination of increasing Lorentz force with the edge confining forces act on the vortex lattice causing a reduction of a, and increasing the dynamic vortex density. However, in the wider stripe ($w = 12\xi$) the same behaviour is not observed, in this case the value of the lattice parameter stays constant (3.6ξ) as the current is increased in the dissipative state. This continues until transitioning to asynchronous crossings. Studies of wider stripes has shown to not reproduce this effect as significantly as narrower stripes [44]. This further emphasises the strong confining effects that occur in very narrow superconducting nanostripes.

The synchronisation of vortex crossing in a fixed lattice at large applied currents was observed and discussed in [45], however an exact regime was not identified. To understand better the regime in which synchronous crossings can occur, a number of simulations were further performed [44]. Figure 4.8 shows another four examples of the modulations in $V(t)$, panels a.i-iv correspond to a stripe with $w = 12\xi$, and $H = 0.2H_{c2}$ which realises a single row of vortices in the static case (figure 3.5). At $J = 0.28J_{DP}$ the stripe starts dissipation with quasi-synchronous behaviour (a.i). At $J \simeq 0.36J_{DP}$ the quasi-synchronous crossings are starting to evolving into a more synchronised behaviour (a.ii). This continues to higher current densities but never transitions to a completely synchronous regime (a.iii). Then

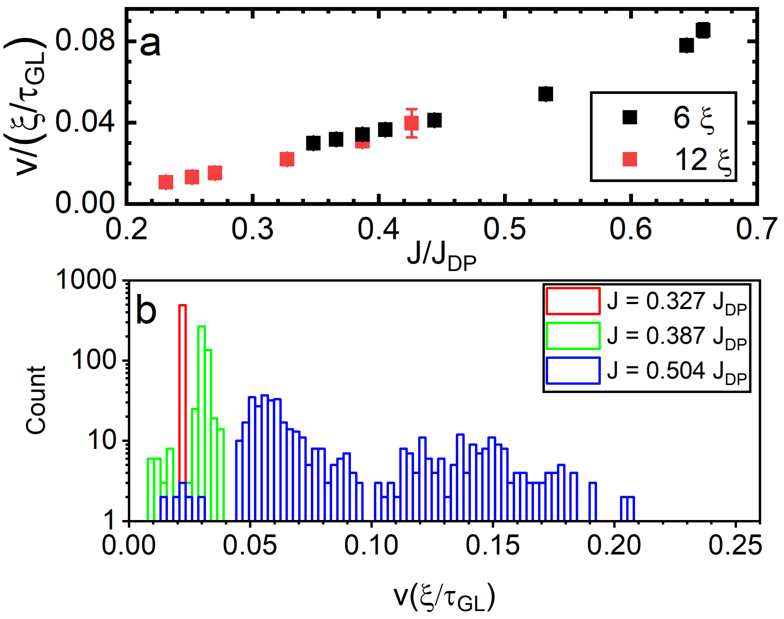

Figure 4.7: Panel a - Normalised average vortex velocity in units of $\xi\tau_{GL}^{-1}$ versus the normalised current density sourced to SN of width 6ξ and 12ξ under an applied magnetic field of $H = 0.25H_{c2}$. Panel b - Histogram of vortex velocities for different values of J relating to different vortex crossing regimes.

at $J = 0.48J_{DP}$ flux flow instability occurs (a.iv) and continues until the normal state at $J = 0.66J_{DP}$. Figure 4.8 panels b.i-iv show similar behaviour for a stripe of width $w = 24\xi$ and $H = 0.12H_{c2}$ (realising two-rows), it does not transition to synchronised crossings. The modulations shown in panels b.i-iv show less synchronised behaviour, which is likely related to the low vortex density unable to force the dynamic vortices into a fixed lattice. However, increasing the magnetic field for both stripes we observe the emergence of synchronous crossings once again, seen in panels c.i-iv and d.i-iv. This time the stripes with $w = 12$ and 24ξ at $H = 0.50$ and $0.15H_{c2}$ respectively, both realising three rows of vortices. For $w = 12\xi$ synchronous crossings start at $J \simeq 0.20J_{DP}$ and continue until the onset of flux-flow instability at $J = 0.28J_{DP}$. Similarly for the stripe with $w = 24\xi$ synchronous crossing occur at $J = 0.28J_{DP}$ and continue to larger current densities of $J = 0.42J_{DP}$, until the onset of flux-flow instability. The larger applied magnetic field for these two stripes leads to a greater vortex density, increasing the interactions forces, which allows for vortices to cross the stripe in a fixed lattice. These results (figures 4.3, 4.5, 4.8) with other simulations has revealed a regime related to vortex density where vortices cross the stripe in a fixed lattice synchronistically. By comparing the average vortex density at the fields for a given stripe that exhibits synchronous crossings, we see that if the condition $A \lesssim 80\xi^2$ is met, then synchronous crossings occur over a range of J.

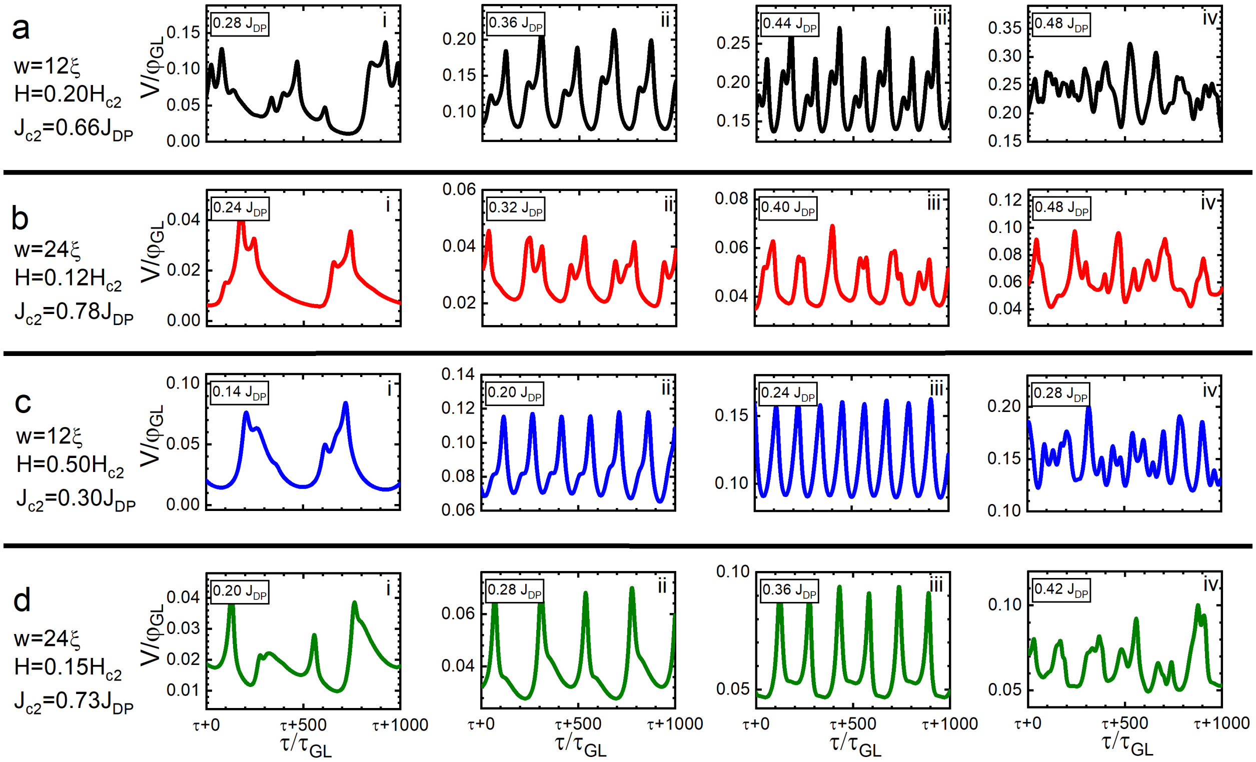

Figure 4.8: Temporal evolution of the normalized voltage drop, at increasing (indicated) values of the sourced current density for two SNs, of width 12ξ and 24ξ. All plots exhibit voltage modulations caused by vortex crossing. Panels a.i-iv: $w = 12\xi$, $H = 0.20H_{c2}$ (single row of vortices). Panels b.i-iv: $w = 24\xi$, $H = 0.12H_{c2}$ (two vortex rows). Panels c.i-iv: $w = 12\xi$, $H = 0.50H_{c2}$ (three rows). Panels d.i-iv: $w = 24\xi$, $H = 0.15H_{c2}$ (three rows). The first panel in each row corresponds to the onset of the dissipative state; the second and third belong to the synchronous/quasi-synchronous regime; the fourth is the onset of the flux-flow instability regime.

4.3.2 Vortex crossings in viscous condensate

The inelastic electron-phonon scattering time (τ_i) is related to the energy gap ($\Gamma = \frac{2\tau_i}{\hbar}|\Delta|$), and for a clean homogeneous superconductor with negligible defects, τ_i has very small values, so the energy gap is smeared out, leading to a gapless superconductor ($\Delta \to 0$) [141]. In a dirty superconductor, when defects on scales smaller than the coherence length ($d_{defect} << \xi(T)$) are present, an energy gap opens up, which increases τ_i, therefore increasing Γ. In the TDGL framework [144, 145], the effect of Γ will introduce viscous effects in the superconducting state, affecting the dynamic behaviour of the condensate. Such a system, with $\Gamma = 10$, when exposed to $H >> H_{c1}$ and $J_{c1} < J < J_c$ exhibits a rearrangement of the vortex lattice due to instabilities [45], where quasi-phase slips lies occurs (Figure 4.9, Panel B and C). The dynamic vortex reduces quasiparticles in front of its motion and produces an excess behind the core. This leads to a region with suppressed order parameter behind the vortex that attracts other vortices resulting in an effective interaction between vortices. The effect originates from the changing shape of the vortex core from non-equilibrium effects. In figure 4.9 the V-J characteristics for a stripe with $w = 12\xi$ and external $H = 0.5H_{c2}$, for different values of Γ (0, 10, 100) can be seen, with a zoom in the top-left inset. For the case of $\Gamma = 0$, the typical result is shown for reference. The black solid lines shows the curve for $\Gamma = 10$, with snapshots of the spatial distribution of the order parameter shown in the lower-right inset (highlighted by black circles on curve). It can be seen that $J_{c1} \simeq 0.1J_{DP}$ is the same when $\Gamma = 0$ and 10, but the dissipative state in which vortices cross the stripe extends to higher J when $\Gamma = 10$. The snapshots show how the vortex crossing transition from an unstable flux-flow state (A), to the quasi-phase slip (B), which continues to high values of J (C) where ultra fast vortex crossings occur. These are similar results to those discussed in the work of Vodolazov [45].

For wider stripes ($w \gtrsim 50\xi$) and $\Gamma = 10$, the coexistence of fast and slow moving vortex channels was observed [45]. Considering very dirty narrow stripes, such that $\Gamma = 100$ some peculiar behaviour is observed. In figure 4.9 it can be seen that superconductivity persists up to and large applied current densities, even greater than J_{DP}, as was suggested in [144] when $\Gamma > 10$. A large value for Γ indicates a large energy gap, which requires higher energy excitations to excite the quasi particles in order to transition to a normal state.

The labels from 1-10 correspond to snapshots of the spatial distribution of the order parameter, shown in figure 4.10. The start crossing the stripe in an asynchronous fashion with no order (panels 1 & 2). Increasing J produces higher vortex velocity which in this case leads to the formation of quasi-phase slip lines (panel 3). Here there exists simultaneously fast and slow moving vortices, where the fast moving vortices propagate in the quasi-phase slip lines. The co-existence of such vortices produces a deformation of the fast moving channel, which is kinked due to the interactions of the slow moving vortices. Increasing J further introduces more quasi-phase slip lines, as can be seen by comparing panels 3-8. As the number of quasi-phase slip lines increases the resistance in the stripe increases also. The different resistive states causes small steps in the V-J curve as seen in figure 4.9. The difference in the vortex velocities between the slow and fast moving vortices can be up to an order of magnitude different, and slow moving vortices seem to be quasi pinned. The dynamics of the vortices also changes as the current is being increased. For example when the kinked quasi-phase slip lines develop, fast moving vortices get trapped in the kink, and over time will leave the fast moving channel and enter the slow moving region. Evidence of this can be seen in some of the panels, for example panel 4 of figure 4.10 shows vortices leaving some of the fast moving channels. At $J \simeq 0.468J_{DP}$ (panel 8) the density of phase slips results vortices entering the slow moving region only from the kinks of the fast moving channels, as oppose to from the edge that occurs at lower J. Increasing the viscosity at large values of Γ results in interesting phenomena, and resistive states that would not exist in clean gapless superconductors.

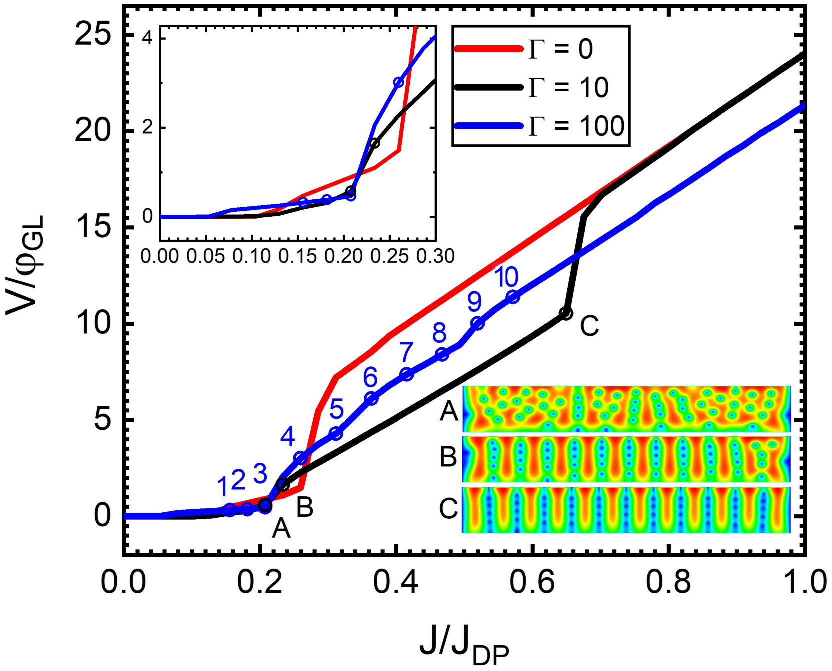

Figure 4.9: Normalised voltage drop as a function of the normalised current density, for a SN of width $w = 12\xi$, at $H = 0.50H_{c2}$, and different magnitudes of viscosity Γ. The bottom inset shows the spatial distribution of the superconducting order parameter for the stripe with $\Gamma = 10$, at different values of J: A: $0.207J_{DP}$, B: $0.238J_{DP}$, C: $0.650J_{DP}$, which are states indicated by back dots on the plot. A zoom of the low J regime, is detailed in the top inset. Blue dots on the $\Gamma = 100$ profile relate to the snap shots A-J shown in figure 4.10.

The FFT of $V(\tau)$ for a stripe of $w = 12\xi$ at different J for the case of $\Gamma = 10$ (corresponding to figure 4.9) can be seen in figure 4.11 (panels A-D). Panel A shows the spectrum of frequency modulations in $V(\tau)$ at $J \simeq 0.21J_{DP}$, where the stripe is in an asynchronous crossing flux flow regime, leading to a noisy spectrum with no clear spectral contributions. Increasing the current density to $J \simeq 0.24J_{DP}$ causes the rearrangement in vortex lattice to the quasi-phase slip resistive state as previously mentioned [45]. The FFT of $V(\tau)$ in this regime shows large peaks contributed to the synchronised crossing of vortices, with the addition of some noisy peaks, which are associated to channel that is not yet a quasi-phase slip line (panel B figure 4.9). The nature of the crossings involves vortices flowing in channels, behind a previous vortex (energetically favourable), which realises an imperfect lattice, where the time-average number of vortices in a given channel may differ, leading to additional modulations in $V(\tau)$. The average vortex speed can be obtained from the frequency of the first peak and the width ($\nu\xi = v$), and divide by the time-average number of vortices in the channels (5 vortices at $J = 0.24J_{DP}$), realising an average velocity of $v \simeq 0.048\xi\tau_{GL}^{-1}$. Increasing J further leads

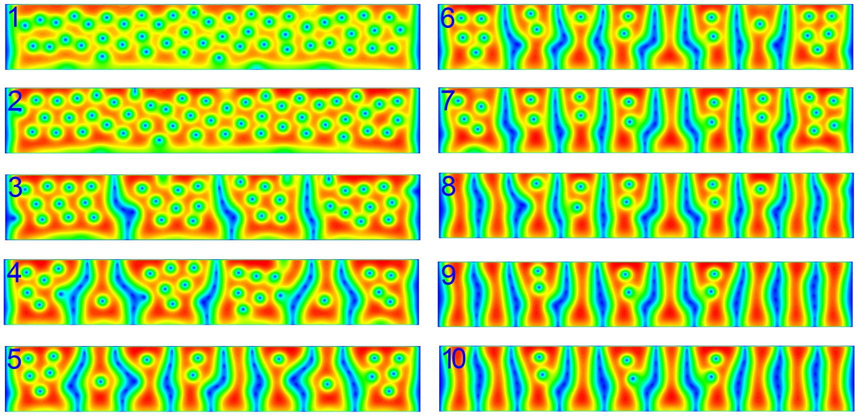

Figure 4.10: Spatial distribution of the superconducting order parameter for a stripe of width 12ξ, $\Gamma = 100$ with an applied magnetic field of $0.5H_{c2}$ at different current densities in units of J_{DP}: 1: 0.156, 2: 0.182, 3: 0.208, 4: 0.260, 5: 0.312, 6: 0.364, 7: 0.416, 8: 0.468, 9: 0.519, 10: 0.571. Each panel is a snapshot of the dynamic process during the crossings of vortices in the disipative state under different sourced currents. Black arrows in panel C highlight the non-linear vortex channel. White arrows in panel D show examples of vortices leaving the non-linear channel, at a kink in the channel.

to sharper and more pronounced peak in the FFT of $V(\tau)$ (panel C) and continues up to $J \simeq 0.650J_{DP}$ (panel D). At $J \simeq 0.650J_{DP}$ the fundamental mode has a frequency of $\nu \simeq 0.16\tau_{GL}^{-1}$ corresponding to $\nu \simeq 2.5$THz for the case of a thin niobium stripe. The vortices reach velocities up to $v \simeq 0.035\xi\tau_{GL}^{-1}$. Such a device could be used for applications involving terahertz electromagnetic emissions.

When considering a very viscous condensate as for $\Gamma = 100$, the FFT of the modulations in $V(\tau)$ do not show individual small line width contributions. When the vortices start crossing the stripe at $J \simeq 0.18J_{DP}$, they cross in an asynchronous fashion in the flux flow regime, and as a result have no clear contributions in the spectra (figure 4.11 panel E). Even when J is increased and fast moving channels in the form of quasi-phase slips appear multiple broad contributions can be seen in the spectra (panel F). Fast moving vortices have velocities between 0.02 - $0.05\xi\tau_{GL}^{-1}$ (figure 4.12, which are similar values to the case of clean superconductor ($\Gamma = 0$). Whilst, slow moving vortices have velocities of $0.005\xi\tau_{GL}^{-1}$, an order of magnitude slower. Figure 4.12 shows the vortex velocities for different sourced J, at $H =$ 0.4, 0.5, $0.6H_{C2}$. The large error bars present result from a broad distribution of vortex ve-

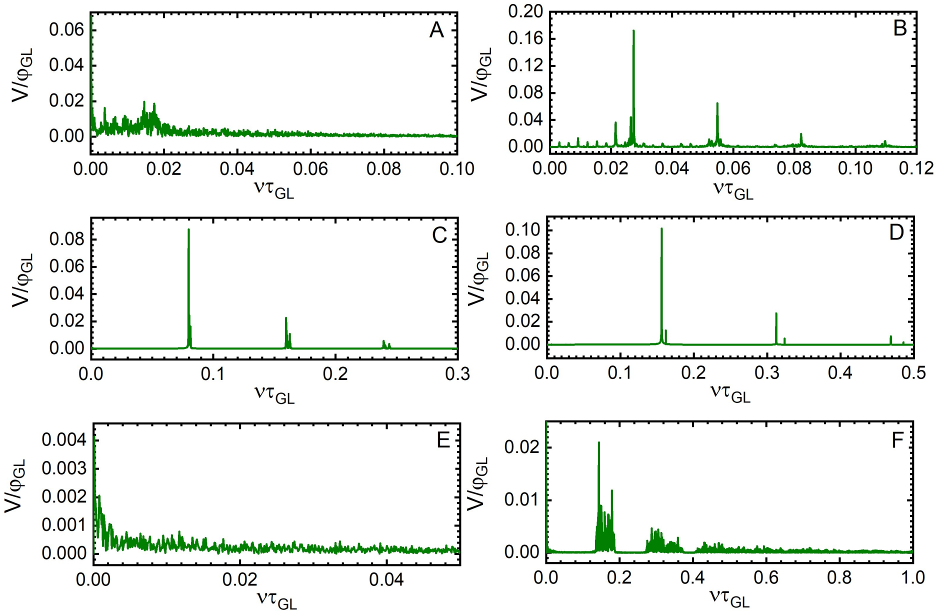

Figure 4.11: Spectrum of the voltage drop modulation for the SN of $w = 12\xi$ under an applied magnetic field of $H = 0.50\ H_{c2}$, with $\Gamma = 10$, for sourced current densities of: A: $0.208 J_{DP}$, B: $0.238 J_{DP}$, C: $0.416 J_{DP}$, D: $0.649 J_{DP}$. For $\Gamma = 100$ with values of J E: $0.182 J_{DP}$, F: $0.416 J_{DP}$.

locities, manifesting from the non-linear channels and their strong interactions with vortices. Considering a typical niobium stripe, slow moving vortices have velocities around 600ms^{-1}, whilst fast moving vortices have velocities around 5kms^{-1}, which is an order of magnitude larger than the ultra-fast vortices observed in [49]. The large broad distribution of vortex velocities and chaotic dynamic state leads to noisy modulations in $V(\tau)$. This suggests that a very viscous condensate would not realise the behaviour suitable for application purposes.

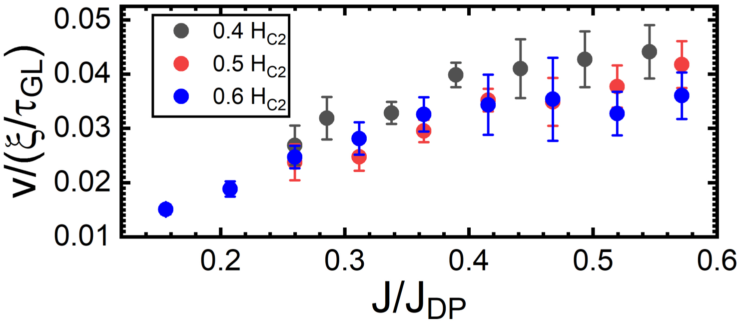

Figure 4.12: Average normalised vortex velocity as a function of the normalised sourced current density for a stripe with $\Gamma = 100$, of width 12ξ at applied magnetic fields of 0.4, 0.5 and $0.6H_{C2}$.

Chapter 5

Response to Thermal Fluctuations Towards Single Photon Detectors

In this section the response of superconducting nanostripes to thermal fluctuations will be discussed. Firstly, how the behaviour of phenomena discussed in this thesis will be affected by different thermal properties of materials, i.e. heat capacity, conductance, and dissipation. This is followed by an investigation of induced hot superconducting bands, where the bands are heated to temperatures $T < T_c$, and the lower-T regions confine the weaker superconducting bands. When a small magnetic field is applied, vortices will flow only through these heated channels in a synchronised fashion. Finally, a discussion about single photon detectors, how absorption of a photon can drive a stripe into the normal state, latching onto it, which can be resolved by coupling to a shunt resistor. Single photon detectors are sensitive to formation and location of the hotspot, and a discussion of how this is linked to detection efficiency and delay timing will be presented.

In this chapter we use the same gTDGL approach as in chapter 4. To model the thermal coupling of our sample to the substrate and the change of the local temperature we use the heat diffusion equation (eqn. 2.46)

$$\widetilde{c}\frac{\partial \widetilde{T}}{\partial \widetilde{t}} = \widetilde{k}\widetilde{\nabla}^2\widetilde{T} - \widetilde{h}\left(\widetilde{T} - \widetilde{T}_0\right) + (\widetilde{\nabla}\widetilde{V})^2. \tag{5.1}$$

where $\widetilde{T}_0$ is the dimensionless bath temperature. The variables $\widetilde{c}$, $\widetilde{k}$ and $\widetilde{h}$ are the dimensionless heat capacity, conductivity and transfer coefficient respectively, and we follow an approach similar to other studies [132, 152].

5.1 Heating induced effects

5.1.1 Variation of heat capacity, conductance and dissipation

In chapter 4, dynamic behaviour of vortices in current-carrying superconducting nanostripes were considered. The results presented assumed that heat would be removed from the system instantly, by considering a large heat transfer coefficient ($h \to \infty$). Heating in the superconductor occurs mostly from Joule heating, but external heating can occur from the absorption of photons and other particles like high energy electrons [198]. Therefore it's important to take a moment to analyse the J-V characteristic curve, comparing different value of material thermal parameters. Figure 5.1 shows just that for stripe of width $w = 19\xi(0)$ with $H = 0.025H_{c2}(0)$. In the top panel the material heat transfer K is compared, evidencing a transition to the normal state at lower J when K is reduced. Each curve transitions to the dissipative state at the same J_{c1}, but as the vortices start crossing the stripe and heating it, the heat must be removed sufficiently fast otherwise heating drives the superconductor into the normal state. Considering this effect for different values of heat conductance, h, bottom panels in figure 5.1 shows how a smaller heating conductance leads to transitions to the normal state at lower J. The lower conductance means there is less flow of heat perpendicular to the isotherms, if the heat can not be transmitted away from the hot regions at a quick enough rate the superconductor is driven into the normal state. So, small values of K and h inhibits the superconductors ability to dissipate away heat, requiring smaller J to drive the superconductor to the normal state.

Variation of the heat capacity between 0.1-1.0C_0 showed similar behaviour but less pronounced, for example at $C = 0.1C_0$ the last critical current was $J_{c2} = 0.56J_{DP}(T_{bath})$, whilst $C = 1.0C_0$ the critical current $J_{c2} = 0.58J_{DP}(T_{bath})$. Considering typical values for thin NbN [46], $C = 0.1C_0, K = 0.06K_0$, and $h = 2 \times 10^{-4}h_0$, we can expect a curve similar to that seen in figure 5.1, bottom panel for with the solid black line. Inspection of the modulations in $V(t)$ and their respective spectra of frequencies revealed the behaviour relating to synchronised vortex crossing is only affected by the range of J where synchronised crossings occurs (for given w and H). When heating effects are considered synchronised vortex crossings will still favour higher vortex density [44], but will continue up to smaller applied J before heating processes drive it to the normal state.

5.1.2 Hot vortex crossings

During energy dissipation from the crossing of normal vortex cores heat is produced and must be transferred to the thermal bath to avoid transition to the normal state, where removal of heat in the system happens over a time scale $\frac{Cd}{h}$. As a result, when heat fluctuations occur over shorter time scales than heat is removed, the superconductor will realise phase-slips that drive the entire superconductor into the normal state. So, to avoid this heating driven transition, it is favourable that C is large and/or h is small. Figure 5.2 shows the J-V characteristics, and spatial distributions of $|\Delta|^2$ and T of a SN with $w = 19\xi(0)$, at $T_{bath} = 0.9T_C$, with $H = 0.025H_{c2}(0)$, and material heating parameters $C = 0.3C_0$, $K = 0.06K_0$, and $h = 0.0002h_0$. The recorded critical current, $J \simeq 0.36J_{DP}(T_{bath})$ is to be expected, corresponding with similar results (see figure 4.1), and snapshots for the spatial distributions of $|\Delta|^2$ and T, at different values of J highlighted by green circles can be seen below the J-V curve. At $J = 0.36J_{DP}(T_{bath})$, $T(x, y)$, vortices enter a dissipative state shown in panel a (figure 5.2), vortices cross the stripe in a quasi-synchronous manner as expected

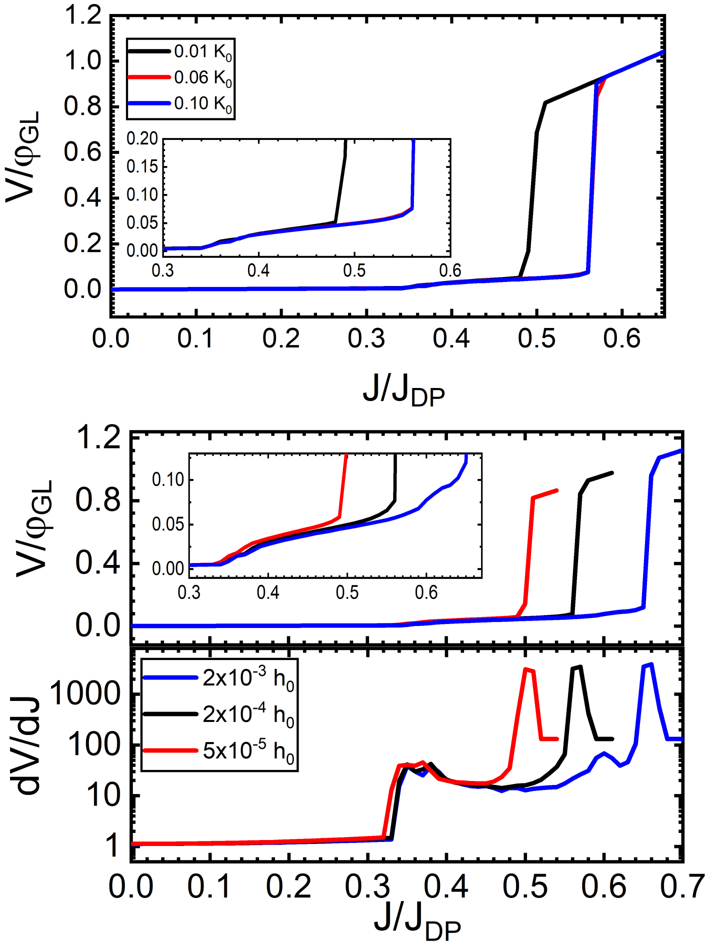

Figure 5.1: Normalised voltage drop as a function of normalised applied current density in units of $\varphi_{GL}(T_{bath})$ and $J_{DP}(T_{bath})$ respectively, for a stripe of width $w = 19\xi(0)$, at applied magnetic field of $H = 0.025H_{c2}(0)$. Top:- comparison of heat conductivity. Bottom:- comparison of heat transfer, with first derivative of V(J).

[44], and evidence of small heating effects can be seen.

This dissipation occurs from the normal vortex core, where the electric field is strongest. The electric field in the vortex core is mostly due to the gradient of electrostatic potential which is associated with the rapid changes of order parameter on opposite sides of the core. A dynamic vortex crossing a narrow stripe produces heat and also carries heat along with it. As the applied current density increases, the gradient of the electrostatic potential increases causing further heating (seen in panels b-e). With the increase of J, the evolution of hot bands can be noticed in the figure, emphasised by the contour lines. At J just below the critical current, for the transition to the normal state, strong heating effects can be seen (panel f). Evidence of heating from a previous vortex crossing can be observed when comparing $|\Delta|^2$ and T in panel e (also at lower J). A hot band is present in center of

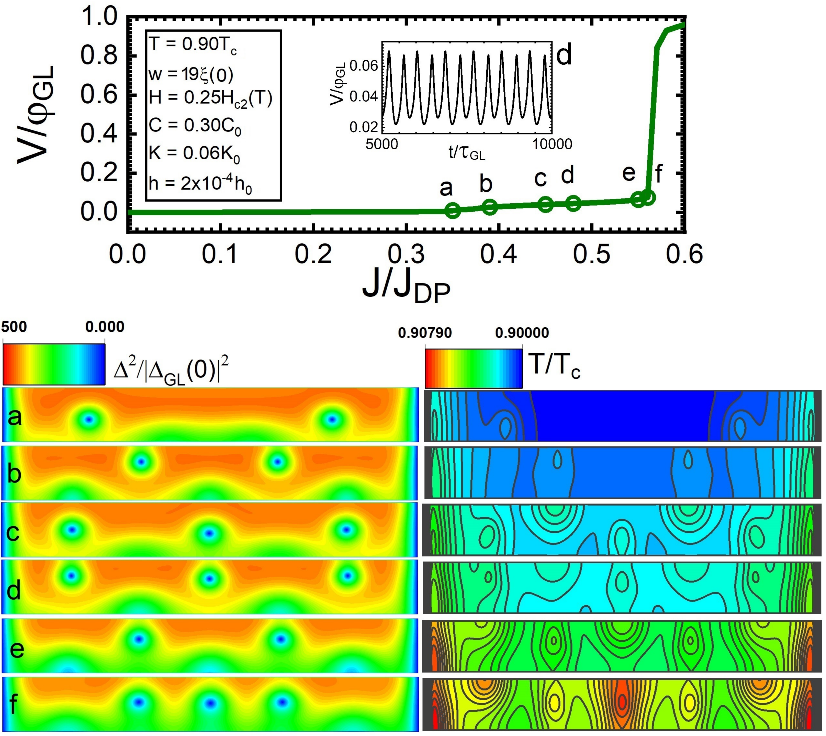

Figure 5.2: Top:- Normalised voltage drop as a function of normalised applied current density in units of $\varphi_{GL}(T_{bath})$ and $J_{DP}(T_{bath})$ respectively at temperature $T_{bath} = 0.9T_c$, for a stripe with width $w = 19\xi(0)$, with an applied magnetic field of $H = 0.025H_{c2}(0)$. The stripe has heating parameters of: heat capacity $C = 0.3C_0$, heat conductivity $K = 0.06K_0$, and heat transfer coefficient $h = 2 \times 10^{-4}h_0$. The plot shows open-circles that indicate the states analysed further at current densities in units of $J_{DP}(T_{bath})$: (a) 0.35, (b) 0.39, (c) 0.45, (d) 0.48, (e) 0.55, (f) 0.56. The inset shows the modulations in $V(t)$ for the superconducting state (d) with period $\tau = 415\tau_{GL}$. Bottom:- snapshots of the spatial distribution of the superconducting order parameter and the respective temperature for the states a-f.

the SN which is the cause of the transition to the normal state when $J \geq 0.56J_{DP}(T_{bath})$. Considering diffusion of heat can be described by the ratio k/C, when this ratio is low hot bands produced by vortex crossing would form at lower J due to the inability to dissipate heat efficiently. The thermal healing length ($\Lambda_h = \sqrt{kd/h}$) should be greater than the distance separating vortices, laterally and transversely, in order to avoid heating effects driving the superconductor to the normal state.

It's worth mentioning that when we consider heating effects with material parameters representative of thin niobium stripes the vortices transition from quasi-synchronous to synchronous crossings as the current is increased as evidenced by the inset within the top panel of figure 5.2. This is due to the fact that $H = 0.025H_{c2}(0)$ realises adequate vortex density according to figure 3.7, when relevant quantities are scaled by their temperature dependent units, where $w = 6\xi(T_{bath})$ and $H = 0.25H_{c2}(T_{bath})$. The system is highly sensitive to thermal fluctuations, and a change in temperature locally changes the local values of ξ, J_{DP}, and H_{c2}, which leads to novel behaviour as will be discussed next.

5.2 Superconducting hot-belt vortex crossings

In this section a discussion of the induction of hot regions on a narrow superconducting stripe will be presented. More specifically, the behaviour observed from inducing bands of hot superconducting regions ($T_{bath} < T < T_c$) will be shown, with comments on possible realisation of such a system and its applications. TDGL simulations are performed for induced hot bands/belts, creating channels where it's energetically favourable to cross, providing heated regions remain narrow as possible. Such process leads to coherent vortex crossings (weak response albeit).

5.2.1 Hot superconducting bands

The effects of vortices crossing the stripe in a dissipative state has shown the generation of "hot bands" in the spatial distribution of the temperature [199], as shown in the previous section. Conversely, if it's possible to artificially heat the stripe creating similar hot bands, then in the heated domain due to their respective thermal dependencies, $\xi(T)$ increases, $J_{DP}(T)$ decreases, and $H_{c2}(T)$ decreases. This would cause the superconducting state to behave differently between the cooler and heated regions for a given set of physical conditions, i.e T_0, J_{app}, and H_{app}. A possible candidate to produce such superconducting hot bands could be low energy electrons beams/guns [200, 201].

To simulate and analyse the superconducting behaviour in such a system, a stripe of width $w = 19\xi(0)$ was subject to an applied magnetic field of $H = 0.01H_{c2}(0)$, a normalised applied current density of $J = 0.0096J_{DP}(0)$, and a bath temperature of $T_0 = 0.9T_c$. With these conditions in place the stripe is in a fully superconducting state, without the presence of vortices. The ground state is found and used as the starting point to perform the simulation with the introduction of hot bands. In figure 5.3 results are shown for such simulation, where at a time $\tau = 1000\tau_{GL}(0)$, an external thermal potential creating hot bands are instantaneously generated with a temperature $T_{band} = 0.99T_c$ and width $D_{band} = 5\xi(0)$ for a total time of $\tau_{bands} = 5000\tau_{GL}(0)$. An effective temperature approach [202] was used to consider the initial heating of the hot-bands to T_{band}, similar to other work [203]. It's valid when the thermalization time is shorter than the inelastic relaxation time due to electron-phonon interactions τ_{e-ph}.

Panels a-d show snapshots of the spatial distribution of temperature, superconducting order parameter and supercurrent density at different times of the evolution of the superconducting state when hot bands are induced. Panel-e shows the voltage drop across the superconductor versus time, over the same period, where red circles highlight the superconducting states in panels a-d. The moment the thermal potential is applied (panel a), the superconductor has had no time to disperse the heat through material. The superconducting

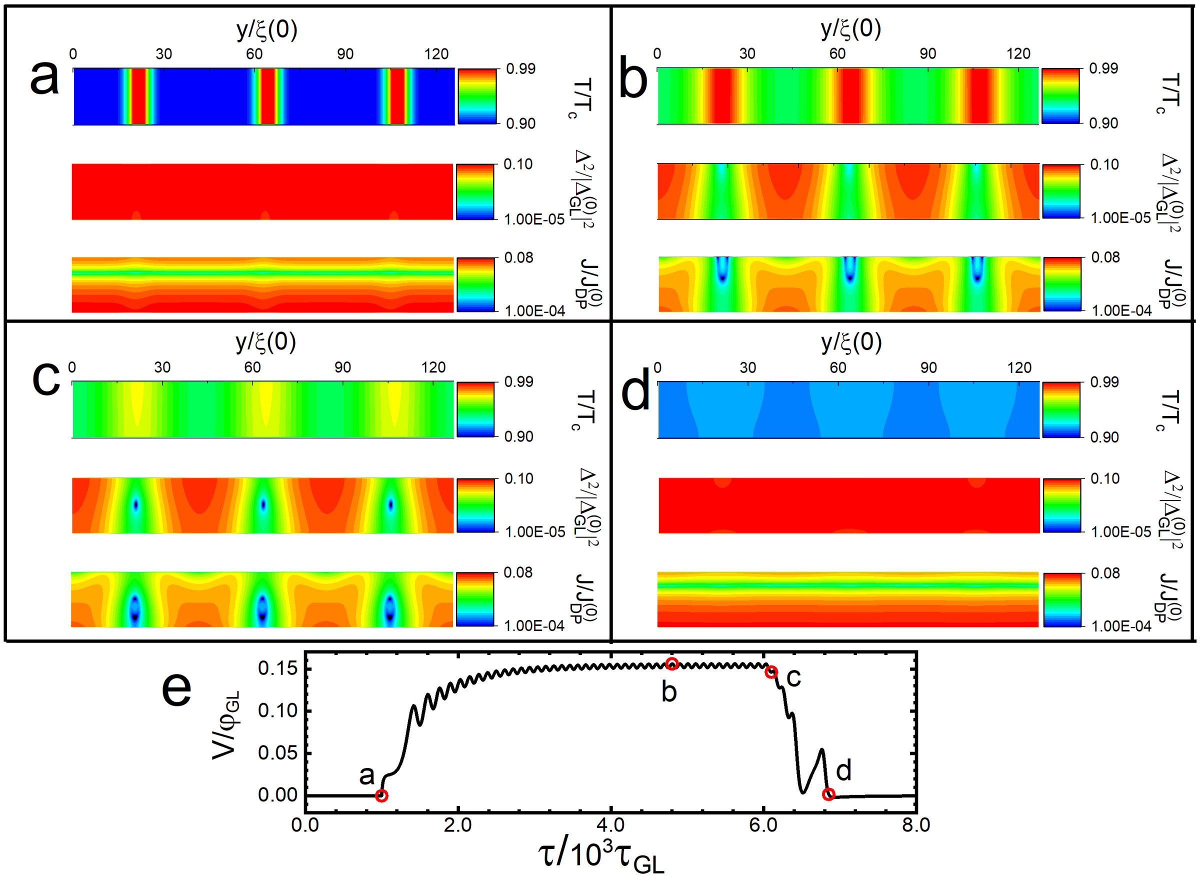

Figure 5.3: Panels a-d: Snapshots for the spatial distributions of normalised temperature, normalised Cooper pair density, and normalised supercurrent density, when hot bands of temperature $T_{band} = 0.99T_c$ with width $D_{band} = 5\xi(0)$ are realised for a duration of $t_{band} = 5000\tau_{GL}(0)$, on a stripe of width $w = 19\xi(0)$, under an applied magnetic field of $H = 0.01H_{c2}(0)$, with a normalised applied current density of $J = 0.0096J_{DP}(0)$, subject to a bath temperature of $T_0 = 0.9T_c$. Panel e: Normalised voltage as a function of normalised time covering the period the hot bands are induced. Panels a-d are taken at times highlighted with red circles in panel e.

order parameter and super current density is reduced in the domain of the hot bands, but unaffected in other regions, and is accompanied with an immediate large jump in $V(t)$. Then, $\tau \simeq 200\tau_{GL}(0)$ later, vortices nucleate at the stripes edge exclusively in the hot band domain, and start to move across the stripe in synchronised rows along their respective hot band. This increases V further, at $\tau \simeq 1250\tau_{GL}(0)$ the vortices leave the stripe at the opposite edge. At this time the superconductor is still heating, and has not reached a dynamic equilibrium. Vortices continue to cross the stripe periodically in rows, whilst the stripe progresses to a thermal equilibrium. After $\tau \simeq 4000\tau_{GL}(0)$, the stripe reaches a thermal and dynamic equilibrium, with vortices continuing to cross periodically in synchronised rows, evidenced by the oscillations in $V(\tau)$. An example of such a state is shown in panel-b, the unheated domains have increased in T due to the dispersion of heat from the hot bands, which should extend over lengths scales of the thermal healing length. The distribution of $|\Delta|^2$ shows how the hot bands have destroyed superconductivity by the small (non-zero) value in those domains, whilst the outer domains clearly show a more superconducting state. Vortices are present and can be seen in the distribution of $|\Delta|^2$ when plotted in logarithmic scale, and is evident in $V(\tau)$ by the presence of the oscillations. The coherence length is dependent on temperature, so as the temperature differs between the hot bands and outer domains, ξ will be different, being larger at higher temperature. At temperature $T_{band} = 0.99T_c$, $\xi(T_{band}) \simeq 1.8\xi(T_0)$, so the normal vortex core is nearly two times larger than it would be at bath temperature. In the hot band domain, both $H_{c2}(T_{band})$ and $J_{DP}(T_{band})$ are lower compared to their respective values at T_0. With the described configuration of physical parameters (T_0, J_{app}, and H_{app}), this led to the condition that in the hot band domain, $H_{app} > H_{c1}(T_{band})$ and $J_{app} > J_{c1}(T_{band})$, allowing for the nucleation and crossing of vortices. Even though the $H_{app} \simeq H_{c2}(T_{band})$ and $J_{app} \simeq 10.0J_{DP}(T_{band})$, the outer domains with a stronger superconducting state confines the weaker domain by shielding the magnetic flux quanta, forming a vortex. After a duration of τ_{band} the thermal potential is instantaneously switched off, figure 5.3 panel-c shows the distributions at a time $100\tau_{GL}(0)$ later, the superconductor has started to cool and the superconducting state in those domains begins to restore. After the snap shot (panel-c) is taken the stripe exhibits an additional 3 more periods of vortex crossings, which can be seen in the two small and one large peak in $V(\tau)$, occurring because the slightly raised temperature in those regions still lead a reduction of the edge barrier, sufficient enough for vortex entry and crossing. Panel-d shows the distributions a short time after the final vortex left the stripe, the temperature has now lowered close to T_0 and the superconductor is recovering to a fully superconducting state.

The behaviour of vortex crossings in hot bands of different widths is important to understand as significant differences occur both qualitatively and quantitatively when the width of the hot band domain is varied. Figure 5.4 shows the temporal variation for $|\Delta|^2$ and J, and $V(\tau)$ whilst hot bands are being induced for different widths of the hot bands $D_{band} = 2.5, 5$ and $15\xi(0)$. In each case the expected behaviour is observed, i.e. when the external potential is introduced vortices will start to cross the stripe repeatedly in synchronised rows. However, quantitative differences occur when comparing the different values of D_{band}. For example, the amplitude and period of oscillations in $|\Delta(\tau)|$ vary (figure 5.4, panel a). When the width of the induced hot band is small the amplitude is large and period longer compared to the wider hot bands. For example, the period of oscillation for $D_{band} = 2.5\xi(0)$ is $\tau_p = 123\tau_{GL}(0)$, and $100\tau_{GL}(0)$ when $D_{band} = 5\xi(0)$. The presence of a larger amplitude of the order parameter infers a higher free density, and as a result leads to a stronger superconducting current density in response to shielding any external magnetic field. The current density varies as the vortices cross the stripe (panel b), effecting the voltage drop across the stripe, $V(t)$ (panel c). where the inset highlights the periods and amplitudes of oscillations. When the width of the hot bands is to large the oscillations are small with a higher frequency. The cooler outer regions help to confine magnetic flux quanta as it crosses the stripe in the form

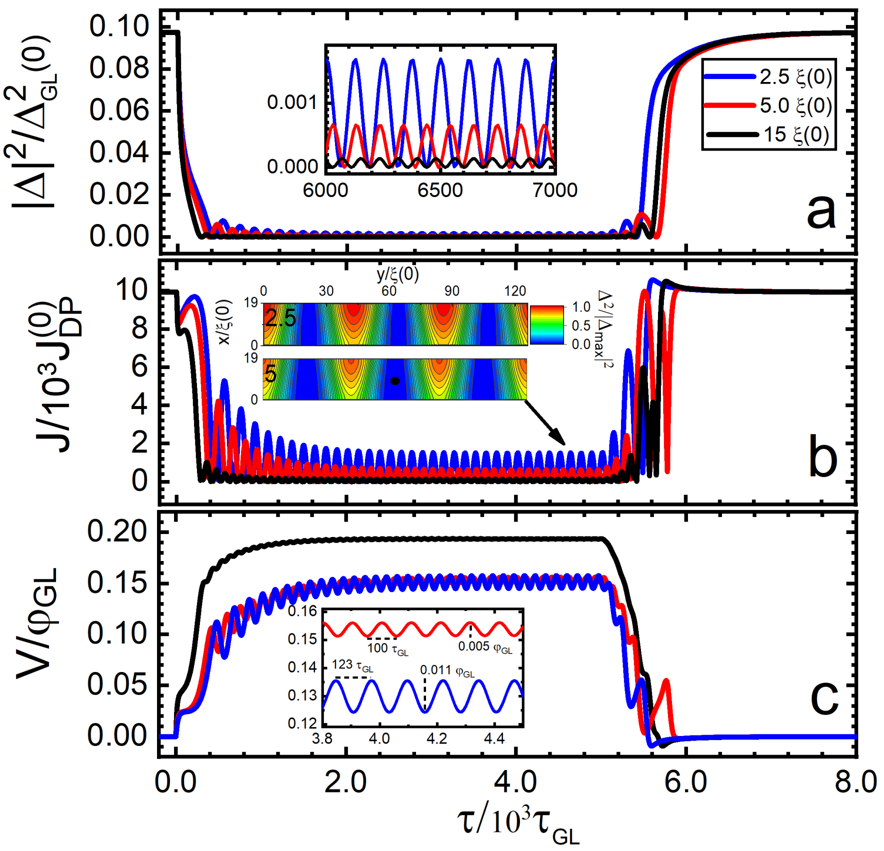

Figure 5.4: Plots are for a stripe of width $w = 19\xi(0)$, under an applied magnetic field of $H = 0.01H_{c2}(0)$, with a normalised applied current density of $J = 0.0096J_{DP}(0)$, subject to a bath temperature of $T_0 = 0.9T_c$. The hot bands induced last for a duration of $\tau = 5000\tau_{GL}(0)$, and are at temperature $T_{band} = 0.99T_c$. The data is recorded at the position located at the center of an induced hot band (black dot in snapshot), for hot bands of width $D_{band} = 2.5, 5$ and $15\xi(0)$. Panel a: Normalised Cooper pair density versus normalised time. Panel b: Normalised supercurrent density versus normalised time. Inset shows the spatial distribution of the superconducting order parameter (2.5 and $5\xi(0)$), taken at a time $\tau \simeq 4300\tau_{GL}(0)$ indicated by the black arrow. Panel c: Normalised voltage drop versus normalised time. Inset is a zoom to show the oscillations in the voltage, with period and amplitude of oscillations indicated.

of vortices. So as the bands are made wider the confining effect is reduced and oscillations become smaller as a result. For an EM emitter, the oscillations observed when the hot band has a small width may be more favourable. If it's possible that an external heating source can be implemented, which produces hot bands similar to those described, with a small H and J, oscillations should be observed, which may be favourable for the generation of EM waves in the MHz-GHz regime.

5.3 Photon detection via a current-carrying superconducting nanostripe

5.3.1 Current-carrying SNSPD

Superconducting nanostripes can be used as the main element of a superconducting nanowire single photon detector (SNSPD), which are commonly fabricated using NbN and TaN [204, 205, 206, 207, 208]. Typical SNSPDs can detect X-ray [208], UV [209], optical [210] and infrared photons [211], and have an efficiency of detection related to the photon's wavelength and the width of the nanostripe. The SNSPD is a specific type of bolometer, and the current-carrying superconducting thin film can be used for a superconducting nano-bolometer [6], including single electron detectors [198] with a mechanism analogous to the photon detector. Various experimental [3, 209, 212, 213, 214, 215, 216] and theoretical [130, 217, 218, 219] work attempted to explain the mechanism behind the detection of an absorbed photon. It was strongly argued that it is a vortex assisted mechanism [220, 203, 5], which creates normal hot-bands [220] and phase slips [221], causing the SNSPD to transition to the normal state, producing a detectable voltage signal. To study the response of a SNSPD the gTDGL framework in this thesis can be used, and is the same approach as other similar studies [132]. An effective temperature approach [202] is taken, assuming that a single absorbed photon creates a hotspot of radius R. The local temperature increase (ΔT), as a result of absorption, is instantaneously applied (ignoring heating) and follows the relation

$$2\pi\hbar c/\lambda = \Delta T \pi R_{initial}^2 C_v d, \tag{5.2}$$

where λ is the wavelength of photon, $R_{initial}$ is the initial radius of the hotspot (expands and dissipates over time), C_v is the heat capacity of quasiparticles (for simplicity is taken as heat capacity of metal in the normal state, when $T < T_c$), and d is the thickness of the superconducting material. The effects of such a hotspot in a current-carrying nanostripe were studied using the described theory [203], although in this work the heat diffusion equation is solved (more generalised version of the heat equation).

Niobium nitride is a typical material used to create SNSPDs with characteristic superconducting quantities: $T_c = 16$K, $\xi(0) = 4.2$nm, $\lambda(0) = 390$nm [212, 132], and $\Gamma = 3$ which is similar to [132]. The material thermal parameters are:- $C_v = 0.05C_0$ ($\simeq$0.2mJ/cm^{3}K), $K = 0.05K_0$ ($\simeq$1.2mW/cm^{3}K), $h = 0.002h_0$ ($\simeq$50W/cm^{2}K) [132, 152], with normal electrical conductivity $\sigma_n = 16\times10^6$S/m [222]. The example nanostripe has a width of $w =$ 160nm, in a thermal bath of $T = 0.9T_c$, then $\xi(0) = 4.2$nm ($w \simeq 12\xi(T)$). The length of the meandering stripe considered is $L = 100\mu$m, and a thickness $d = 5$nm assuming that $d \ll \xi, \lambda$. The length given is used to consider the kinetic inductance (discussed next), but to simulate the smaller region of concern, a similar approach to [203] is used, where the outer regions of "no concern" are simulated with a much higher Tc, using a "numerical trick" keeping the temperature unchanged ($T = 0.9T_c$) in that region.

Figure 5.5 shows the temporal variation of the superconducting order parameter (panel a) and the local temperature (panel b), located at the center of a hotspot created by a photon,

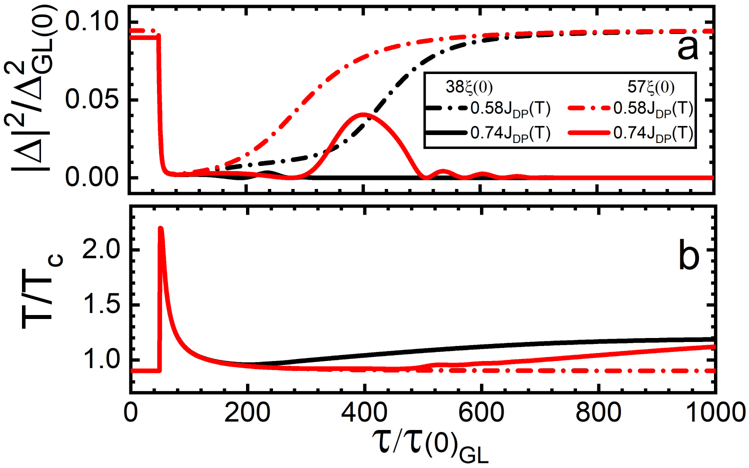

Figure 5.5: Time dependence of the magnitude of the order parameter (a) and temperature (b) in the center of the induced hotspot, for two values of the applied current density, $J = 0.58 J_{DP}(T_{bath})$ and $J = 0.74 J_{DP}(T_{bath})$, for two widths $w = 38, 57\xi(0)$, with bath temperature a thermal bath of temperature $T_{bath} = 0.9 T_c$, in zero magnetic field. The absorption of a photon induces a local instantaneous increase in temperature to $T_{spot} = 2.2$ T_c ($\Delta T = 1.3$ T_c).

for different applied biased currents of 0.58 and $0.74 J_{DP}(T_{bath})$, and different widths of $w = 38$ and $57\xi(0)$. A photon absorbed by the current-carrying superconducting stripe forms a hotspot of radius $R = 9.5\xi(0)$ and increases the temperature to $T = 2.2 T_c$ ($\Delta T = 1.3 T_c$), equivalent to a wavelength of 30μm (long wave IR). At the hotspot location superconductivity is destroyed, so the supercurrent flows around this region, and the current density increases which leads to current crowding [131]. If the biased current is too high then the current density around hotspot can exceed J_{DP}, causing the creation of a vortex-antivortex pair which travel to opposite side of the nanostripe. Evidence of this effect can be observed in figure 5.5-a at $J = 0.74 J_{DP}(T_{bath})$ for $w = 57\xi(0)$, where at $\tau \simeq 400\tau_{GL}(0)$ there is a large maximum in $|\Delta|^2$ that corresponds to the separation of the vortex-antivortex (V-aV) pair. This repeats two more times, whilst the order parameter decreases in magnitude, creating a hot normal belt which starts the heating of this domain. Evidence of this can be seen in figure 5.5-b at around $\tau \simeq 520\tau_{GL}(0)$, as is reported in [203]. The same occurs for a narrower stripe, but the creation of the first vortex-antivortex pair destroys superconductivity and start heating at earlier times. This normal domain needs a mechanism to help it cool, as it would "latch" onto the normal state otherwise [219], and continue to heat via traditional Joule heating. A comprehensive study on this system showed similar behaviour for a range of nanostripe widths ([203], figures 3,4,5). If the biased current density is below some threshold J_{det}^{min} the current crowing effect will not cause the creation of a V-aV pair which assists the formation of a normal belt leading to a detectable voltage signal. Figure 5.5 shows how with

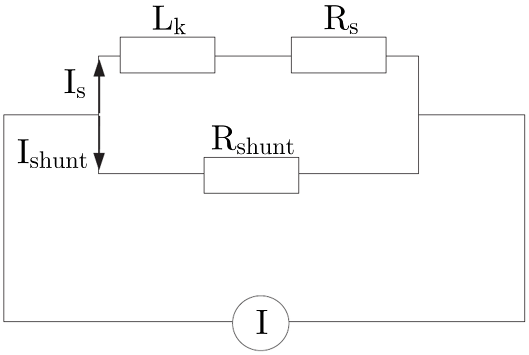

Figure 5.6: The electrical scheme representing the superconducting detector. The superconductor is modelled by kinetic inductance L_k and resistance R_s which appeared due to absorbing the photon. The shunt has resistance R_{shunt}.

$J = 0.58 J_{DP}(T_{bath})$ the superconducting state begins to recover almost immediately after the creation of the hotspot. The minimum current density required to form a hot normal band (assisted with v-aV creation), J_{det}^{min}, decreases with increasing photon energy, and increases with increasing width of SNSPD [203].

5.3.2 Inclusion of shunt resistor

To simulate a real experiment avoiding the issue of the superconductor latching onto the normal state, the electrical scheme shown in figure 5.6 is used, modelled by the equation [223]

$$L_K \frac{dJ_s}{dt} = (J - J_s) R_{shunt} - V_s, \tag{5.3}$$

where J_s is the current density applied across the superconductor, J is the total current density, R_{shunt} is the shunt resistor with a typical value of 50Ω, and V_s is the voltage drop across the superconductor; following the numerical approach used by [203, 5]. The gTDGL framework relies on dimensionless units for a solution, so inductance can be given in units of

$$L_{K_{GL}} = \frac{\Phi_0 e^* \pi}{8 k_B u} \frac{1}{\sigma_n \xi(0) T_c}, \tag{5.4}$$

which is ≃ 3pH for NbN. The resistance is given in units of

$$R_{GL} = \frac{1}{\sigma_n \xi(0)}, \tag{5.5}$$

which is ≃ 14.9Ω for NbN. The kinetic inductance of the stripe is given by [223]

$$L_K = \mu_0 \lambda_L^2 L (wd)^- 1, \tag{5.6}$$

where the length L considers the entire length of the meandering wire. Equation 5.2 is coupled to the gTDGL equations via J_s, and is solved using the Euler method [224]. Figure 5.7 shows the temporal variation of the voltage drop (panels a,d), and the current density (panels b,e) for both the SNSPD and shunt resistor. It also shows the superconducting order parameter with local temperature at the center of the hotspot (panels c,f), for two different hotspot temperatures of 2.2K (left) and 4.5K (right) with two values of bias current (0.58 and $0.74 J_{DP}(T_{bath})$) and width ($w = 38, 57\xi(0)$). The first difference noticed from introducing a shunt resistor is the recovery of the superconducting state with applied bias current $J = 0.74 J_{DP}(T_{bath})$ for the hotspot with $T = 2.2T_c$ (panel a-c, blue lines). The hotspot causes a resistive state in the SNSPD (panel a, blue solid line), and as a result part of the current is redirected to the shunt resistor (panel b, blue dashed line) which reduces the affect of Joule heating, allowing for the superconductor to cool (panel-c, blue dotted line) and return to a superconducting state (panel-c, solid blue line). As the superconducting stripe cools 6 pairs of a vortex-antivortex are created, evidenced by the oscillations in $V(\tau)$ and $|\Delta|^2(t)$ (figure 5.7 insets of panel a and c respectively), which is similar to voltage pulse observed in [203] (figures 7 and 8). Figure 5.7 e-f shows similar results but for a photon of wavelength $\simeq 5\mu$m, producing a hotspot of temperature with $\Delta T = 3.6T_c$. The higher energetic photon results with a larger voltage pulse, and the formation of vortex-antivortex pairs at the lower biased current $J = 0.58 J_{DP}(T_{bath})$. In the wider stripe for $w = 57\xi(0)$, the voltage drop across the stripe reaches its maximum (with lower amplitude) after a longer time, due to vortex-antivortex pair producing a normal hot-band that covers a larger area than the narrower case, requiring a longer time to transition to a normal state. The simulations are over simplified, they do not consider the loss of photon energy in the first stage of heating, neglect temperature dependence of heat capacity, simplifies energy transfer to photons (here neglected), and did not consider direct excitation from the incoming photon [203]. Although the approach adopted such simplifications the theory qualitatively captures the main physics of the processes occurring during the detection on a single photon.

5.3.3 Delay time and timing jitter

SNSPDs exhibit finite delay time τ_d in the appearance of a voltage pulse after absorption of a photon. There is a variation associated with τ_d called "timing jitter", which originates from experimental factors like the electronics and the read-out system. The timing jitter is also influenced by the dynamics of $|\Delta|^2$ and the position of where the photon is absorbed, generating a hotspot [225, 226, 5, 227]. Figure 5.8 shows the position (a) and current (a) dependence of τ_d when a photon. The figures show a number of interesting points, firstly, how τ_d decreases with increasing the applied current. Secondly, the jitter brought about by position of the hotspot is reduced as the current is increased, this is seen by the flattening of the profiles at higher I. Lastly, the greater the energy transferred by the photon causes both lower τ_d and jitter with respect to lower energies [225]. The same authors show theoretically it's possible that a given energy deposited at the centre of the stripe will not cause formation of vortices and appearance of the normal domain, but will do so if the energy is deposited

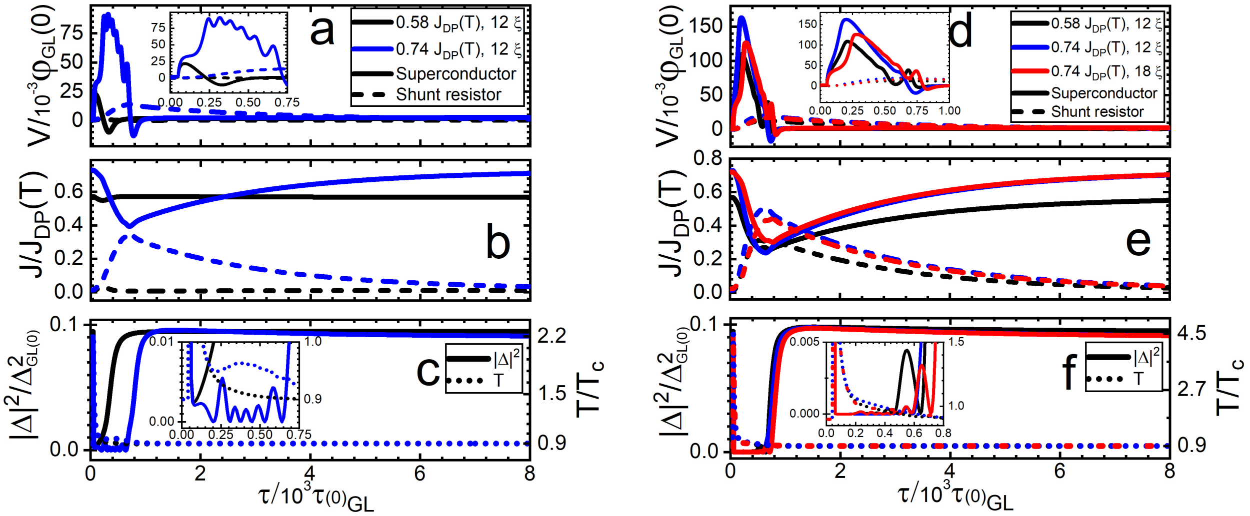

Figure 5.7: Stripe of width $w = 38, 57\xi(0)$, with hot-spot causing a local instantaneous increase in temperature to $T_{spot} = 2.2T_c$ (panels a-c), and $T_{spot} = 4.5T_c$ (panels d-f), with profiles for applied current densities of $J = 0.58$ and $0.74J_{DP}(0)$. Panel a,d - normalised voltage across the stripe as a function of normalised time. Solid line corresponds to the voltage drop across the superconductor, V_s, and the dotted lined corresponds to the potential difference across the shunt resistor, $(I - I_s)R_{shunt}$. Inset shows zoom of the same profile over the first $\sim 1000\tau_{GL}(0)$. Panel b,e - normalised current density as a function of normalised time for the current density in the superconductor (solid) and the shunt (dotted). Panel c,f - time dependence of the magnitude of the order parameter (solid) and temperature (dotted) in the center of the hotspot, where the inset shows a zoom of the same profiles over the first $\sim 800\tau_{GL}(0)$.

t!

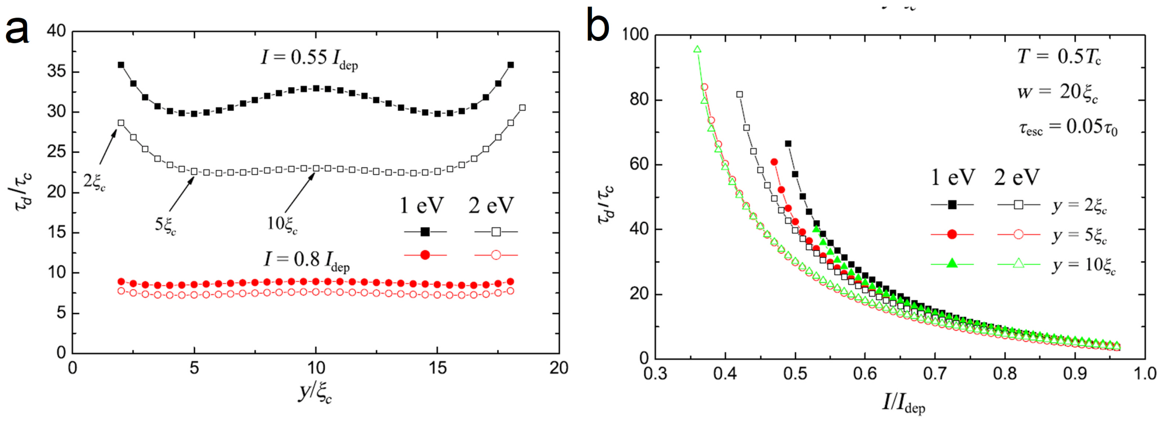

Figure 5.8: Dependencies of the delay time for a stripe of width $w = 20\xi$, at bath temperature $T = 0.5T_c$. Panel a- Position-dependent τ_d at different currents and deposited energies ($E = 1eV \longrightarrow T_{spot} = 2T_c$ and $E = 2eV \longrightarrow T_{spot} = 2.4T_c$). Panel b - Dependence of τ_d on current for three positions of the initial hotspot $y = 2, 5, 10\xi$ and two deposited energies 1 and 2eV. Taken from ref [225] figure 3.

away from the centre. The authors [225] claim their numerical results can be compared semi-quantitatively with experiments on dependence of timing jitter on the current and energy of the photon [228, 229]. The discrepancies originate from the treatment of the thermalization of electrons in the system. The model assumed complete thermalization, but it is only partially fulfilled due to relatively large inelastic electron-electron relaxation time for electrons with energy close to the energy gap and above the Fermi level, resulting with the electron distribution function deviating from Fermi-Dirac distribution. Ref [230] used two models in their study, quasi-equilibrium and non-thermal model, τ_d was shown to differ slightly, but was qualitatively similar.

5.3.4 Consequences of meandering geometry

The typical geometry of SNSPDs consisting of meandering nanostripes, with bends at 90 degrees (1.6) has consequences on it's dynamic behaviour after the absorption of a photon. Theoretical studies [132] have shown when a current is applied, the supercurrent density distribution is inhomogeneous, decaying rapidly from the inner corner to the outer [131]. The superconductor will remain in a zero-resistive state until a threshold voltage is reached, at which point vortices nucleate at the inside corner of the 90 degree bend and proceed to cross the stripe periodically [132]. The vortex nucleation rate at the inner corner increases with increasing of the applied current, until there is an increase in resistance at another threshold current, where a channel of kinematic vortices appears. Similarly to studies on narrow stripes, the value of the first threshold current significantly decreases with increasing width, whilst the second threshold current value decreases but only slightly [132]. When a photon strikes the central part of the stripe at low current densities the superconducting state remains stable against the photon action (similarly shown in figure 5.7 panel a, $J = 0.58J_{DP}(T_{bath})$). At higher applied current densities an unbinding of a vortex-antivortex pair occurs (seen in figure 5.7 panel a, $J = 0.74J_{DP}(T_{bath})$), an increases in rate with increasing current, until fast moving vortices create a normal belt that is detectable (electronically) [132]. The study [132] theoretically confirmed vortex-assisted photon counting mechanism [199, 203] at current densities just below J_c, where individual photons are detected thanks to the periodic motion of the vortex-antivortex pair [197]. The same study [132] theoretically demonstrates that a photon strikes the corner of the 90 degree bend, and a vortex is created at much lower applied currents than the critical one. The intensity/duration of the voltage signal as a result of the vortex motion if much smaller/longer than when comparing the signal for the unbinding of a vortex-antivortex. Instabilities occur after photon absorption due to the nucleation and dissociation of multiple-quantised vortices, where current density is greatest. No transition to a phase-slip state is observed, whilst the resistive state is characterised by a weakly dissipative vortex crossing [199]. In summary a photon strike at the corner of SNSPD at a 90 degree bend is less likely to be detected electronically than a strike in the main body[132].

5.3.5 Intrinsic detection efficiency

One of the main characteristics of a SNSPD is the intrinsic detection efficiency (IDE) which is the probability to detect a photon when it is absorbed by the main element of the SNSPD (superconducting current-carrying meandering nanostripe [216]). The IDE must be distinguished from the system detection efficiency which is the overall probability for the entire detector. A review [204] of proposed mechanisms for photon detection in SNSPDs suggested that the experimental cut-off in the detection efficiency is determined by the lack of the current-carrying ability of the superconducting condensate. Additionally, stating that the IDE depends on the applied currents proximity to the depairing current. Using a TDGL approach to consider a hotspot induced by a photon, (which takes into account the current crowding effect [131] and suppression of the superconductivity by the current [203]), the dependence of the IDE on applied current and field was studied [5]. They showed how the minimal current, at which the resistive state appears in a superconducting stripe, depended on the position along the width where the photon created a hotspot. For example, this current was minimal at the edges, with a minimum at a distance $\delta w = R$ (δw is the distance from the edge of stripe and R is the radius of hotspot), and decreased with radius of the hotspot (for fixed width of stripe, see figure 4 in [5]). If the applied current was below the detecting current for every position along the width of the stripe ($I_{det}(y)$), then IDE = 0. If the applied current exceed $I_{det}(y)$ along the width then IDE = 1, and IDE < 1 in some intermediate regime. This was in the absence of fluctuations, which in reality may cause the entry of a vortex that assist in the detection of the photon even when $I < I^{det}_{min}$ [5]. The effect of introducing a magnetic field was also studied, the Meissner effect causes the total supercurrent to be more on one side and less on the other. As a result, I_{det} is lower on the side where total super current is greatest, and vice versa. In order for a vortex to enter, the fluctuation must overcome the existing edge barrier barrier ΔF. The barrier ΔF can be numerically calculated using a method [156], and the IDE calculated using the Arrhenius law IDE $= \beta e^{-\Delta F/k_B T}$ (T is the temperature associated to the fluctuation) [5]. A smooth change of IDE(I) was observed between IDE = 0.05 - 1.0 associated with current induced vortex crossings (current crowding effect destroying order parameter), and a fast decay at IDE $<$ 0.05 associated to fluctuation assisted vortex entry, which is more of a probabilistic event associated with the Arrhenius law. The IDE, and thus the efficiency for a superconductor to detect the photon strongly depends on the applied current, and the wavelength of the photon [5], whilst relying on a vortex assisted mechanism [203, 220] for weak excitations. The qualitative behaviour of the IDE is assumed to be similar for narrow SNs, but reduce in standard deviation across the width of wider stripes.

Conclusion

The confinement of superconducting nanostripes to two dimensions results in a rich tapestry of complex phenomena. The primary objective of this thesis was to explore the ramifications of strong vortex confinement in narrow and thin superconducting nanostripes on their static and dynamic behavior. This was accomplished by utilizing a generalized version of the time-dependent Ginzburg-Landau formalism and numerically solving the equations self-consistently on a finite grid. Our research uncovered a diverse range of phenomena linked to confinement forces acting on superconducting vortices in both static and dynamic equilibrium, as supported by strong empirical evidence.

The objects of interest in our study were narrow nanostripes characterized by lateral dimensions comparable to the superconducting coherence length, resulting in a low or quasi-two dimensional regime that differed from the bulk case due to edge-induced interactions. The penetration of magnetic flux in the form of superconducting vortices in these nanostripes required external magnetic fields of higher strength than the bulk first critical field, H_{c1}. As the flux density increased, the superconducting vortices organized themselves into a lattice reminiscent of the Abrikosov configuration, albeit with significant deviations due to the pronounced confining edge forces that we demonstrated.

Our research has clearly demonstrated that at sufficiently high magnetic fields, superconducting vortices within the nanostripes arrange themselves into vortex rows, with their number increasing as the magnetic field strength is raised and the vortex density increases. However, it is essential to note that this phenomenon occurs only if the width of the nanostripe is sufficiently large to accommodate a new row of vortices. This was explicitly revealed in our vortex row phase diagram, which showed the transition to new vortex rows as a function of the nanostripe width and magnetic field strength. Our investigation also disclosed significant discrepancies from theoretical predictions that disregarded the effects of the edges. Specifically, the strong edge Meissner fields constrained and reduced the vortex density, thereby causing deviations from the expected transitions.

The confinement at the edges of the nanostripes intensified with an increase in the applied magnetic field, leading to evidence of non-monotonic behavior. Specifically, we observed the reconfiguration of two vortex rows back to a single row due to the interplay between the interaction of the vortices and the confinement forces at the edge, which changed as the magnetic field strength (H) was increased. This phenomenon resulted from a dimensional crossover regime between approximately $20 - 80$ coherence lengths (ξ). Additionally, the critical current exhibited a dependence on the applied magnetic field, exhibiting local minima and maxima. Pinning forces originating from commensurate effects between the width of the nanostripe and the number of vortex rows were responsible for this behavior.

We discovered that a sufficiently high vortex density ($\gtrapprox 80\xi$) enables vortices to cross a superconducting nanostripe in a synchronized manner. This phenomenon arises due to the interplay of vortex-vortex interactions, pinning forces from the edge Meissner field, and the Lorentz force. These synchronized vortex crossings produce oscillations in the electromagnetic field of the superconducting nanostripe, resulting in the emission of a photon whose energy is proportional to the oscillation frequency. This property is highly advantageous for nanoscale gigahertz-terahertz electromagnetic emitters. To simulate the effects of dirty superconductors, we introduced viscosity through the variable Γ_0, effectively opening an energy gap. Such effects give rise to a range of vortex dynamics, including the formation of multiple quasi-phase slip lines and quasi-synchronous vortex crossings, which are also beneficial for nanoscale electromagnetic emitters.

The dissipative state in a superconductor is characterized by Joule heating, which is a problematic behavior that can drive the material into the normal state when heat cannot be removed from the system at a sufficient rate. We demonstrated that this results in a reduction of the range of applied current at which the material remains in the superconducting state, ultimately lowering the upper critical current. Moreover, concerning the synchronization of vortex crossings, we found that for typical values of heating parameters (heat capacity C, transfer coefficient h , conductivity k), the criteria remain the same. However, as the applied current increases beyond a certain threshold, the material is driven into the normal state due to Joule heating.

The temperature dependence of physical quantities, such as the coherence length and Ginzburg-Landau current density, results in local variations of these properties within the material. Therefore, changes in temperature affect the behavior of the superconducting condensate locally. In our investigation, we examined the behavior of a system in which hot bands are induced laterally across a nanostripe by an external process, such as the diffraction of electromagnetic radiation. These hot bands are separated by the ambient state of the superconductor. We demonstrated that at sufficiently high values of applied current density and external magnetic field, the hot bands exhibit synchronised vortex crossings, which are confined by the superconducting state operating at lower localized temperatures. We propose that inducing narrow hot bands via illumination of a superconducting nanostripe is an alternative method for inducing highly synchronised vortex crossings. Our results show that the intensity modulation of the emitted radiation is amplified for narrower hot bands, highlighting the significance of confinement in the case of synchronised vortex crossings. However, we found that when the width of the hot bands exceeds approximately 5 times the coherence length at the given temperature, the amplitude of modulation decreases to negligible levels, rendering the device unsuitable for electromagnetic emitter purposes.

The superconducting nanostripe serves multi purposes, such as an emitter of photons and as a key component of superconducting single photon detectors. Upon absorption of a photon, a region of the nanostripe experiences a local temperature increase above the critical temperature. This causes the formation of a vortex-antivortex pair, which subsequently crosses the nanostripe and dissipates energy as heat, inducing a normal resistive hot-band region. This hot-band region results in the production of a detectable voltage pulse. Our investigations revealed that the characteristics of the voltage pulse depend on the magnitude of the applied current and the width of the nanostripe, with narrower geometries yielding larger amplitudes of the voltage pulse.

The operation of detectors is not only influenced by the nanostripe, but also by geometrical aspects such as meandering design, which leads to current crowding at corners. Such regions become favourable sites for vortex nucleation and crossing, which occurs at lower sourced currents. The delay time between photon absorption and the voltage pulse is dependent on the sourced current, with higher values favouring lower delay times. Moreover, the position of photon absorption introduces timing jitter to the process.

Throughout this thesis, we have conducted a comprehensive investigation into the phenomena associated with superconductivity at the nanoscale in narrow and thin superconducting nanostripe geometries. Our findings may provide valuable insights into analogous systems with similar physics. One such example is the behavior of vortices in a confined Bose-Einstein condensate in a "narrow channel" trap, where the confinement frequencies in the x and y directions differ [231]. It was observed that transitions to different numbers of vortex rows occur with an increasing dimensionless parameter β, which represents a coefficient for a fourth-order term in the free energy functional of the system. Our research adds to the understanding of these types of systems and their underlying physics.

Our findings and insights have the potential to advance the development of novel applications, such as nanoscale electromagnetic emitters that generate narrowband frequencies when vortices synchronously cross the nanostripe. The behaviors and dynamics we have observed are strongly influenced by system variables, such as the stripe width, applied magnetic field and current, among others. We expect that any nanoscale superconducting application utilizing the nanostripe geometry with parameters within the range of our studies will exhibit similar characteristics. One such application is the superconducting single photon detector, where the nanostripe serves as a crucial component.

In light of our findings on synchronised vortex rows, further exploration of resistive state transitions with varying viscosity through Γ, J, and H could be pursued to uncover regimes with highly regular and stable synchronised row crossings at higher frequencies. To fully account for heating in such a resistive system, it may be necessary to include the heat balance equation. Additionally, our investigation into hot bands induced below T_c but above T_{bath} could benefit from a more comprehensive study encompassing a wider range of applied fields and current densities. This intriguing concept, as evidenced by our initial results, may provide an effective mechanism for inducing synchronous vortex crossings and achieving single frequency modulations, which definitely warrants further investigations.

Appendix

Numerical approach and discretisation of equations

In order to perform simulations of superconducting behaviour, the extended gTDGL equations 2.43-2.46 must be solved on a finite grid, where the superconductor is discretised and the equations solved at each point. The finite-differences method [232] is a natural choice to solve such sets of differential equations. In order to properly capture the physics and dynamics of the system, it is important that the maximum size of the unit cell is less than $0.3\xi(0)$ along all axis. The superconducting systems studied in this work are thin superconductors that meet the high-κ criteria, so the vector potential and current density are considered to be uniformly distributed over the surface. This results with the equations having no z-components, and so the problem is reduced from 3D to 2D, leaving the boundary condition (equation 2.13) fulfilled at the surfaces along the z-axis.

The set of equations 2.43-2.46 are solved self-consistently through an iterative procedure. For a fast and stable convergence for the solution of the vector potential, the complex link variable vector is used

$$\mathbf{U}(\mathbf{r}_0, \mathbf{r}) = \sum_{\mu=x,y} \mathbf{e}_\mu e^{-i\int_{\mu_0}^{\mu} Q_\mu d\mu}, \tag{7}$$

where $\mathbf{e}_{\mu=x,y}$ are the unit vectors in the x and y direction, and $\mathbf{r}_0 = \sum_{\mu=x,y} \mathbf{e}_\mu \mu_0$ is a given reference point. The link variables are primarily introduced to restore gauge invariance, that gets lost when the partial differential equations are discretised using the finite differences method [233, 234, 235, 236]. When considering the componenets of the link varialbe vector, these rules must be followed

$$\frac{\partial U_\mu}{\partial \mu} = -iQ_\mu U_\mu, \tag{8}$$

$$\frac{\partial^2 U_\mu}{\partial \mu^2} = -i\frac{\partial Q_\mu}{\partial \mu} U_\mu - Q_\mu^2 U_\mu. \tag{9}$$

The term $\mathbf{J}_s = |\chi|^2(\widetilde{\nabla}\theta - \mathbf{Q})$ can be written as $\mathfrak{I}\left\{\chi^*(\widetilde{\nabla} - i\mathbf{Q})\right\}$, which allows for the first and second derivatives in equations 2.43-2.46 to be expressed as

$$\left(\widetilde{\nabla} - i\mathbf{Q}\right)\chi = \sum_{\mu=x,y} \mathbf{e}_\mu \frac{1}{U_\mu}\frac{\partial}{\partial \mu}(U_\mu \chi), \tag{10}$$

$$\left(\widetilde{\nabla} - i\mathbf{Q}\right)^2 \chi = \sum_{\mu=x,y} \mathbf{e}_\mu \frac{1}{U_\mu} \frac{\partial^2}{\partial \mu^2}(U_\mu \chi). \tag{11}$$

In equation 2.43 the term $\frac{\widetilde{\Gamma}^2}{2}\frac{\partial|\chi|^2}{\partial \widetilde{t}}$ is not suitable for numerical treatment, instead it can be written in a more convenient term

$$\frac{\widetilde{\Gamma}^2}{2}\frac{\partial|\chi|^2}{\partial \widetilde{t}}\chi = \frac{\widetilde{\Gamma}^2}{1+\widetilde{\Gamma}^2|\chi|^2}\,\mathrm{Re}\left\{\chi^*\Phi\right\}\chi, \tag{12}$$

where

$$\Phi = \frac{\sqrt{1+\widetilde{\Gamma}^2|\chi|^2}}{u}[(\widetilde{\nabla} - i\mathbf{Q})^2\chi + (f - g|\chi|^2)\chi].$$

The Euler method [224] is used to discretise the time derivatives, and the Gauss-Siedel method [237] to solve linear equations iteratively on a rectangular system of size $L_x \times L_y$, by combing the two the following expression is obtained for equation 2.43

$$\chi^{\widetilde{t}+\Delta\widetilde{t}}_{m,n} = \Delta\widetilde{t}\left[\frac{1}{\Delta\widetilde{t}} - i\widetilde{V}_{m,n} - \frac{\widetilde{\Gamma}^2}{1+\widetilde{\Gamma}^2|\chi^{\widetilde{t}}_{m,n}|^2}\,\mathrm{Re}\left\{\chi^{*\widetilde{t}}_{m,n}\Phi^{\widetilde{t}}_{m,n}\right\}\right]\chi^{\widetilde{t}}_{m,n} + \Delta\widetilde{t}\Phi^{\widetilde{t}}_{m,n} \tag{13}$$

where $n = 1, 2, .., N_x$ and $m = 1, 2, .., N_y$ are the indices in the x and y directions respectively (The total number of grid points are $N_\mu = \frac{L_\mu + \Delta_\mu}{\Delta_\mu}$), and that

$$\begin{aligned}
\Phi^{\widetilde{t}}_{m,n} = {} & \frac{\sqrt{1+\widetilde{\Gamma}^2|\chi^{\widetilde{t}}_{m,n}|^2}}{u}\,\frac{\widetilde{U}^{\widetilde{t}}_{x_{m+1,n}}\chi^{\widetilde{t}}_{m+1,n} - 2\chi^{\widetilde{t}}_{m,n} + \widetilde{U}^{\widetilde{t}}_{x_{m-1,n}}\chi^{\widetilde{t}}_{m-1,n}}{\Delta x^2} \\
& + \frac{\sqrt{1+\widetilde{\Gamma}^2|\chi^{\widetilde{t}}_{m,n}|^2}}{u}\,\frac{\widetilde{U}^{\widetilde{t}}_{x_{m,n+1}}\chi^{\widetilde{t}}_{m,n+1} - 2\chi^{\widetilde{t}}_{m,n} + \widetilde{U}^{\widetilde{t}}_{x_{m,n-1}}\chi^{\widetilde{t}}_{m,n-1}}{\Delta y^2} \\
& + \frac{\sqrt{1+\widetilde{\Gamma}^2|\chi^{\widetilde{t}}_{m,n}|^2}}{u}\left(f_{m,n} - g_{m,n}|\chi^{\widetilde{t}}_{m,n}|^2\right)\chi^{\widetilde{t}}_{m,n}
\end{aligned} \tag{14}$$

This equations contain different link variables that are modified for the forward and backward components in the x and y direction. The forward x and y components read

$$\widetilde{U}^{\widetilde{t}}_{x_{m+1,n}} = \frac{\widetilde{U}^{\widetilde{t}}_{x_{m+1,n}}}{\widetilde{U}^{\widetilde{t}}_{x_{m,n}}} = \frac{e^{-i\int_{x_0}^{x=(m+1)\Delta x} Q_x dx}}{e^{-i\int_{x_0}^{x=m\Delta x} Q_x dx}} \simeq e^{-iQ_{x_{m+1,n}}\Delta x}, \tag{15}$$

$$\widetilde{U}^{\widetilde{t}}_{y_{m,n+1}} = \frac{\widetilde{U}^{\widetilde{t}}_{y_{m,n+1}}}{\widetilde{U}^{\widetilde{t}}_{y_{m,n}}} = \frac{e^{-i\int_{y_0}^{y=(n+1)\Delta y} Q_y dy}}{e^{-i\int_{y_0}^{y=n\Delta x} Q_y dy}} \simeq e^{-iQ_{y_{m,n+1}}\Delta y}, \tag{16}$$

and the backward components are

$$\widetilde{U}^{\widetilde{t}}_{x_{m-1,n}} = \frac{\widetilde{U}^{\widetilde{t}}_{x_{m-1,n}}}{\widetilde{U}^{\widetilde{t}}_{x_{m,n}}} = \frac{e^{-i\int_{x_0}^{x=(m-1)\Delta x} Q_x dx}}{e^{-i\int_{x_0}^{x=m\Delta x} Q_x dx}} \simeq e^{iQ_{x_{m,n}}\Delta x}, \tag{17}$$

$$\widetilde{U}^{\tilde{t}}_{y_{m,n-1}} = \frac{\widetilde{U}^{\tilde{t}}_{y_{m,n-1}}}{\widetilde{U}^{\tilde{t}}_{y_{m,n}}} = \frac{e^{-i\int_{y_0}^{y=(n-1)\Delta y} Q_y dy}}{e^{-i\int_{y_0}^{y=n\Delta x} Q_y dy}} \simeq e^{iQ_{y_{m,n}}\Delta y}. \tag{18}$$

At the superconducting-insulator boundary ($n_{boundary} = 1, N_y$ and $m_{boundary} = 1, N_x$) the following conditions must be met: $U^{\tilde{t}}_{x_{m\pm1,n}}\chi^{\tilde{t}}_{x_{m\pm1,n}} = \chi^{\tilde{t}}_{m,n}|_{m=m_{boundary}}$, and $U^{\tilde{t}}_{y_{m,n\pm1}}\chi^{\tilde{t}}_{x_{m,n\pm1}} = \chi^{\tilde{t}}_{m,n}|_{n=n_{boundary}}$. At the superconducting-normal boundary there is no superconducting condensate, the order parameter is zero, and so the conditions are: $\chi^{\tilde{t}}_{m,n}|_{n=n_{boundary}} = 0$ and $\chi^{\tilde{t}}_{m,n}|_{m=m_{boundary}} = 0$. When $\widetilde{V} = 0$, in the zero-electrostatic potential gauge, equation 2.45 is ignored and 2.44 can be separated in these two scalar terms [238]

$$\widetilde{U}^{\tilde{t}+\Delta\tilde{t}}_{\mu_{m,n}} = \left(\frac{1}{\Delta\tilde{t}} - i\Delta\tilde{t}\mathfrak{F}\left\{\mathcal{F}^{\tilde{t}}_{\mu_{m,n}}\right\}\right)\widetilde{U}^{\tilde{t}}_{\mu_{m,n}}. \tag{19}$$

The functions $\mathcal{F}^{\tilde{t}}_{\mu_{m,n}}$ are expressed as

$$\begin{aligned}\mathcal{F}^{\tilde{t}}_{x_{m,n}} = \kappa^2 &\frac{\widetilde{U}^{*\tilde{t}}_{x_{m,n+1}}\widetilde{U}^{*\tilde{t}}_{y_{m,n}}\widetilde{U}^{\tilde{t}}_{x_{m,n}}\widetilde{U}^{\tilde{t}}_{y_{m+1,n}} - \widetilde{U}^{*\tilde{t}}_{x_{m,n}}\widetilde{U}^{*\tilde{t}}_{y_{m,n-1}}\widetilde{U}^{\tilde{t}}_{x_{m,n-1}}\widetilde{U}^{\tilde{t}}_{y_{m+1,n-1}}}{\Delta y^2} \\ &+ \widetilde{U}^{\tilde{t}}_{x_{m,n}}\chi^{*\tilde{t}}_{m,n}\chi^{\tilde{t}}_{m+1,n},\end{aligned} \tag{20}$$

$$\begin{aligned}\mathcal{F}^{\tilde{t}}_{y_{m,n}} = \kappa^2 &\frac{\widetilde{U}^{*\tilde{t}}_{x_{m-1,n+1}}\widetilde{U}^{*\tilde{t}}_{y_{m-1,n}}\widetilde{U}^{\tilde{t}}_{x_{m-1,n}}\widetilde{U}^{\tilde{t}}_{y_{m,n}} - \widetilde{U}^{*\tilde{t}}_{x_{m,n+1}}\widetilde{U}^{*\tilde{t}}_{y_{m,n}}\widetilde{U}^{\tilde{t}}_{x_{m,n}}\widetilde{U}^{\tilde{t}}_{y_{m+1,n}}}{\Delta x^2} \\ &+ \widetilde{U}^{\tilde{t}}_{x_{m,n}}\chi^{*\tilde{t}}_{m,n}\chi^{\tilde{t}}_{m,n+1}\end{aligned} \tag{21}$$

Equations A.13 is a type of diffusion equations, and requires the Crank-Nielson implicit method, providing a faster and stable solution [239]. At the edge of the simulated region ($n = n_{boundary}$,$m = m_{boundary}$) the relation between the link variables and the external magnetic field reads

$$\widetilde{B}_{ext} = \frac{1 - \widetilde{U}^{*\tilde{t}}_{x_{m,n+1}}\widetilde{U}^{*\tilde{t}}_{x_{m,n}}\widetilde{U}^{*\tilde{t}}_{y_{m,n}}\widetilde{U}^{*\tilde{t}}_{y_{m+1,n}}}{i\Delta x\Delta y}. \tag{22}$$

In the high-κ limit with Colmoumb gauge, when the magnetic field in the superconductor is homogeneous, equation 2.44 is omitted and the discretisation of equation 2.45 reads

$$\begin{aligned}&\frac{\widetilde{V}_{m+1,n} - 2\widetilde{V}_{m,n} + \widetilde{V}_{m-1,n}}{\Delta x^2} + \frac{\widetilde{V}_{m,n+1} - 2\widetilde{V}_{m,n} + \widetilde{V}_{m,n-1}}{\Delta y^2} \\ &\qquad = \frac{J_{S_{x_{m+1,n}}} - J_{S_{x_{m-1,n}}}}{2\Delta x} + \frac{J_{S_{y_{m,n+1}}} - J_{S_{y_{m,n-1}}}}{2\Delta y},\end{aligned} \tag{23}$$

with the supercurrent components expressed as

$$J_{S_{x_{m,n}}} = \mathfrak{F}\left\{\chi^{*\tilde{t}}_{m,n}\frac{\chi^{\tilde{t}}_{m+1,n}U^{\tilde{t}}_{m+1,n} - \chi^{\tilde{t}}_{m,n}}{\Delta x}\right\}, \tag{24}$$

$$J_{S_{y m,n}} = \mathfrak{F}\left\{\chi^{*\widetilde{t}}_{m,n}\frac{\chi^{\widetilde{t}}_{m,n+1}U^{\widetilde{t}}_{m,n+1} - \chi^{\widetilde{t}}_{m,n}}{\Delta y}\right\}. \tag{25}$$

The fast Fourier transform (FFT) algorithm [240] is used to numerically solve equation A.17, when simulating rectangular geometries. For other arbitrary geometries it is more suitable to use the successive over-relaxation method [241]. When considering the SI boundary, where no current flows perpendicular to the surface ($\mathbf{n}_{SI} \cdot \widetilde{\nabla}\widetilde{V} = 0$), the discretised electrostatic potential terms are $\widetilde{V}_{m\pm1,n} = \widetilde{V}_{m,n}|_{m=m_{boundary}}$ and $\widetilde{V}_{m,n\pm1} = \widetilde{V}_{m,n}|_{n=n_{boundary}}$. A transport current is applied via normal contacts with a SN boundary, the applied current transforms in a normal current with component perpendicular to the SN boundary ($\mathfrak{n}_{SN} \cdot \widetilde{\nabla}\widetilde{V} = \mathfrak{J}_a$), the electrostatic potential terms are $\widetilde{V}_{m\pm1,n} = \widetilde{V}_{m,n} \pm \widetilde{J}_a\Delta x|_{m=m_{boundary}}$ and $\widetilde{V}_{m,n\pm1} = \widetilde{V}_{m,n} \pm \widetilde{J}_a\Delta y|_{n=n_{boundary}}$. The collection of Neumann boundary conditions results in a situation where equation A.17, which is a type of Poisson equation, does not have a unique solution. To find a unique solution, additional conditions can be imposed, for example the we can define $< \widetilde{V} >= 0$, this will not affect the behaviour or physical quantities because they depend on the potential difference (voltage) U between points. Alternatively, it is more favourable to apply an external potential difference, such that the boundary conditions become $\widetilde{V}_{m,n} = \widetilde{V}_{ext}|_{m=m_{boundary}}$ and $\widetilde{V}_{m,n} = \widetilde{V}_{ext}|_{n=n_{boundary}}$. Finally, the discretisation of the thermal balance equation reads

$$\begin{aligned}\widetilde{T}^{\widetilde{t}+\Delta\widetilde{t}}_{m,n} &= \widetilde{T}^{\widetilde{t}}_{m,n} - \Delta\widetilde{t}\left(\widetilde{T}^{\widetilde{t}}_{m,n} - \widetilde{T}_0\right)\frac{\widetilde{h}}{\widetilde{c}} + \frac{\Delta\widetilde{t}}{\widetilde{c}}\mathbf{J}^{\widetilde{t}2}_{n_{m,n}} \\ &+ \Delta\widetilde{t}\left(\frac{\widetilde{T}^{\widetilde{t}}_{m+1,n} - 2\widetilde{T}^{\widetilde{t}}_{m,n} + \widetilde{T}^{\widetilde{t}}_{m-1,n}}{\Delta x^2} + \frac{\widetilde{T}^{\widetilde{t}}_{m,n+1} - 2\widetilde{T}^{\widetilde{t}}_{m,n} + \widetilde{T}^{\widetilde{t}}_{m,n-1}}{\Delta y^2}\right)\frac{\widetilde{k}}{\widetilde{c}},\end{aligned} \tag{26}$$

where this type of differential equation requires the alternating direction implicit method to find a solution [242]. At the SN boundary, a Dirichlet condition is used to specify that the metallic contact's temperature is set above the critical temperature, mainly $\widetilde{T} \geq 1$. At the SI boundary a Neumann boundary condition is imposed, such that $\widetilde{\nabla}\widetilde{T} = 0$, signifying an open flow of heat through the system.

Bibliography

[1] Robert H Hadfield. Single-photon detectors for optical quantum information applications. *Nature Photonics*, 3(12):696–705, 2009.

[2] Chandra M Natarajan, Michael G Tanner, and Robert H Hadfield. Superconducting nanowire single-photon detectors: physics and applications. *Superconductor Science and Technology*, 25(6):063001, 2012.

[3] GN Gol'Tsman, O Okunev, G Chulkova, A Lipatov, A Semenov, K Smirnov, B Voronov, A Dzardanov, C Williams, and Roman Sobolewski. Picosecond superconducting single-photon optical detector. *Applied Physics Letters*, 79(6):705–707, 2001.

[4] Eric A Dauler, Bryan S Robinson, Andrew J Kerman, Joel KW Yang, Kristine M Rosfjord, Vikas Anant, Boris Voronov, Gregory Gol'tsman, and Karl K Berggren. Multi-element superconducting nanowire single-photon detector. *IEEE Transactions on Applied Superconductivity*, 17(2):279–284, 2007.

[5] AN Zotova and D Yu Vodolazov. Intrinsic detection efficiency of superconducting nanowire single photon detector in the modified hot spot model. *Superconductor Science and Technology*, 27(12):125001, 2014.

[6] A Shurakov, Y Lobanov, and Grigory Goltsman. Superconducting hot-electron bolometer: from the discovery of hot-electron phenomena to practical applications. *Superconductor Science and Technology*, 29(2):023001, 2015.

[7] Adrian T Lee, Paul L Richards, Sae Woo Nam, Blas Cabrera, and Kent D Irwin. A superconducting bolometer with strong electrothermal feedback. *Applied Physics Letters*, 69(12):1801–1803, 1996.

[8] VK Vlasko-Vlasov, F Colauto, Alexandre I Buzdin, D Rosenmann, T Benseman, and W-K Kwok. Magnetic gates and guides for superconducting vortices. *Physical Review B*, 95(14):144504, 2017.

[9] VK Vlasko-Vlasov, F Colauto, Alexandre I Buzdin, D Rosenmann, T Benseman, and W-K Kwok. Manipulating Abrikosov vortices with soft magnetic stripes. *Physical Review B*, 95(17):174514, 2017.

[10] Rosa Córdoba, Pablo Orús, Željko L Jelić, Javier Sesé, Manuel Ricardo Ibarra, Isabel Guillamón, Sebastián Vieira, Juan José Palacios, Hermann Suderow, Milorad V Milosević, et al. Long-range vortex transfer in superconducting nanowires. *Scientific Reports*, 9(1):1–10, 2019.

[11] J Brooke, David Bitko, Rosenbaum, and Gabriel Aeppli. Quantum annealing of a disordered magnet. *Science*, 284(5415):779–781, 1999.

[12] MW Johnson, P Bunyk, F Maibaum, E Tolkacheva, AJ Berkley, EM Chapple, R Harris, J Johansson, T Lanting, I Perminov, et al. A scalable control system for a superconducting adiabatic quantum optimization processor. *Superconductor Science and Technology*, 23(6):065004, 2010.

[13] Frederick W Strauch, Philip R Johnson, Alex J Dragt, CJ Lobb, JR Anderson, and FC Wellstood. Quantum logic gates for coupled superconducting phase qubits. *Physical Review Letters*, 91(16):167005, 2003.

[14] Tadashi Kadowaki and Hidetoshi Nishimori. Quantum annealing in the transverse Ising model. *Physical Review E*, 58(5):5355, 1998.

[15] Giuseppe E Santoro, Roman Martoňák, Erio Tosatti, and Roberto Car. Theory of quantum annealing of an Ising spin glass. *Science*, 295(5564):2427–2430, 2002.

[16] Davide Pastorello and Enrico Blanzieri. Quantum annealing learning search for solving QUBO problems. *Quantum Information Processing*, 18(10):1–17, 2019.

[17] Fred Glover, Gary Kochenberger, and Yu Du. A tutorial on formulating and using QUBO models. *arXiv preprint arXiv:1811.11538*, 2018.

[18] Aleta Berk Finnila, MA Gomez, C Sebenik, Catherine Stenson, and Jimmie D Doll. Quantum annealing: A new method for minimizing multidimensional functions. *Chemical Physics Letters*, 219(5-6):343–348, 1994.

[19] Arnab Das and Bikas K Chakrabarti. Colloquium: Quantum annealing and analog quantum computation. *Reviews of Modern Physics*, 80(3):1061, 2008.

[20] Fuyuki Ando, Yuta Miyasaka, Tian Li, Jun Ishizuka, Tomonori Arakawa, Yoichi Shiota, Takahiro Moriyama, Youichi Yanase, and Teruo Ono. Observation of superconducting diode effect. *Nature*, 584(7821):373–376, 2020.

[21] Akito Daido, Yuhei Ikeda, and Youichi Yanase. Intrinsic Superconducting Diode Effect. *Physical Review Letters*, 128(3):037001, 2022.

[22] Charles Reichhardt and CJ Olson Reichhardt. Jamming and diode effects for vortices in nanostructured superconductors. *Physica C: Superconductivity*, 470(19):722–725, 2010.

[23] JF Wambaugh, C Reichhardt, CJ Olson, F Marchesoni, and Franco Nori. Superconducting fluxon pumps and lenses. *Physical Review Letters*, 83(24):5106, 1999.

[24] Andrea Perali, Antonio Bianconi, Alessandra Lanzara, and Naurang L Saini. The gap amplification at a shape resonance in a superlattice of quantum stripes: A mechanism for high-T_c. *Solid State Communications*, 100(3):181–186, 1996.

[25] Nicola Pinto, S Javad Rezvani, Andrea Perali, Luca Flammia, Milorad V Milošević, Matteo Fretto, Cristina Cassiago, and Natascia De Leo. Dimensional crossover and incipient quantum size effects in superconducting niobium nanofilms. *Scientific Reports*, 8(1):1–12, 2018.

[26] VV Moshchalkov, Lut Gielen, C Strunk, Rik Jonckheere, X Qiu, C Van Haesendonck, and Yvan Bruynseraede. Effect of sample topology on the critical fields of mesoscopic superconductors. *Nature*, 373(6512):319–322, 1995.

[27] CP Bean and JD Livingston. Surface barrier in type-II superconductors. *Physical Review Letters*, 12(1):14, 1964.

[28] Tristan Cren, Denis Fokin, François Debontridder, Vincent Dubost, and Dimitri Roditchev. Ultimate vortex confinement studied by scanning tunneling spectroscopy. *Physical Review Letters*, 102(12):127005, 2009.

[29] GR Berdiyorov, XH Chao, FM Peeters, HB Wang, VV Moshchalkov, and BY Zhu. Magnetoresistance oscillations in superconducting strips: A Ginzburg-Landau study. *Physical Review B*, 86(22):224504, 2012.

[30] PW Anderson and AH Dayem. Radio-frequency effects in superconducting thin film bridges. *Physical Review Letters*, 13(6):195, 1964.

[31] Rosa Córdoba, TI Baturina, J Sesé, A Yu Mironov, JM De Teresa, MR Ibarra, DA Nasimov, AK Gutakovskii, AV Latyshev, I Guillamón, et al. Magnetic field-induced dissipation-free state in superconducting nanostructures. *Nature Communications*, 4 (1):1–7, 2013.

[32] GR Berdiyorov, MV Milošević, ML Latimer, ZL Xiao, WK Kwok, and FM Peeters. Large magnetoresistance oscillations in mesoscopic superconductors due to current-excited moving vortices. *Physical Review Letters*, 109(5):057004, 2012.

[33] Gregory J Kimmel, Andreas Glatz, Valerii M Vinokur, and Ivan A Sadovskyy. Edge effect pinning in mesoscopic superconducting strips with non-uniform distribution of defects. *Scientific Reports*, 9(1):1–12, 2019.

[34] DY Vodolazov. Vortex-induced negative magnetoresistance and peak effect in narrow superconducting films. *Physical Review B*, 88(1):014525, 2013.

[35] PG De Gennes. Vortex nucleation in type-II superconductors. *Solid State Communications*, 3(6):127–130, 1965.

[36] L Kramer. Stability limits of the Meissner state and the mechanism of spontaneous vortex nucleation in superconductors. *Physical Review*, 170(2):475, 1968.

[37] Ryuzo Kato, Yoshihisa Enomoto, and Sadamichi Maekawa. Effects of the surface boundary on the magnetization process in type-II superconductors. *Physical Review B*, 47(13):8016, 1993.

[38] I Aranson, M Gitterman, and B Ya Shapiro. Onset of vortices in thin superconducting strips and wires. *Physical Review B*, 51(5):3092, 1995.

[39] D Yu Vodolazov, IL Maksimov, and EH Brandt. Vortex entry conditions in type-II superconductors.: Effect of surface defects. *Physica C: Superconductivity*, 384(1-2): 211–226, 2003.

[40] J Gutierrez, Bart Raes, Joris Van de Vondel, AV Silhanek, RBG Kramer, GW Ataklti, and Victor V Moshchalkov. First vortex entry into a perpendicularly magnetized superconducting thin film. *Physical Review B*, 88(18):184504, 2013.

[41] Nodar Samkharadze, A Bruno, Pasquale Scarlino, G Zheng, DP DiVincenzo, L DiCarlo, and LMK Vandersypen. High-kinetic-inductance superconducting nanowire resonators for circuit QED in a magnetic field. *Physical Review Applied*, 5(4):044004, 2016.

[42] LN Bulaevskii and EM Chudnovsky. Electromagnetic radiation from vortex flow in type-II superconductors. *Physical Review Letters*, 97(19):197002, 2006.

[43] OV Dobrovolskiy, VM Bevz, M Yu Mikhailov, OI Yuzephovich, VA Shklovskij, RV Vovk, MI Tsindlekht, R Sachser, and M Huth. Microwave emission from superconducting vortices in Mo/Si superlattices. *Nature Communications*, 9(1):1–9, 2018.

[44] Benjamin McNaughton, Nicola Pinto, Andrea Perali, and Milorad V Milošević. Causes and consequences of ordering and dynamic phases of confined vortex rows in superconducting nanostripes. *Nanomaterials*, 12(22):4043, 2022.

[45] D Yu Vodolazov and FM Peeters. Rearrangement of the vortex lattice due to instabilities of vortex flow. *Physical Review B*, 76(1):014521, 2007.

[46] ŽL Jelić, MV Milošević, and AV Silhanek. Velocimetry of superconducting vortices based on stroboscopic resonances. *Scientific Reports*, 6(1):1–8, 2016.

[47] Lior Embon, Yonathan Anahory, Željko L Jelić, Ella O Lachman, Yuri Myasoedov, Martin E Huber, Grigori P Mikitik, Alejandro V Silhanek, Milorad V Milošević, Alexander Gurevich, et al. Imaging of super-fast dynamics and flow instabilities of superconducting vortices. *Nature Communications*, 8(1):1–10, 2017.

[48] G Carapella, P Sabatino, C Barone, S Pagano, and M Gombos. Current driven transition from Abrikosov-Josephson to Josephson-like vortex in mesoscopic lateral S/S'/S superconducting weak links. *Scientific Reports*, 6(1):1–12, 2016.

[49] OV Dobrovolskiy, D Yu Vodolazov, F Porrati, R Sachser, VM Bevz, M Yu Mikhailov, AV Chumak, and M Huth. Ultra-fast vortex motion in a direct-write Nb-C superconductor. *Nature Communications*, 11(1):1–10, 2020.

[50] SE Hebboul, DP Johnson, and M Rokhlin. Radio-frequency oscillations in two-dimensional superconducting In-InO$_x$: a possible evidence for vortex density waves. *Physical Review Letters*, 82(4):831, 1999.

[51] H Kamerlingh Onnes. Experiments on the condensation of helium by expansion. In *KNAW Proceedings*, volume 10, pages 1907–1908, 1908.

[52] Heike Kamerlingh Onnes. The superconductivity of mercury. *Comm. Phys. Lab. Univ. Leiden*, 122:122–124, 1911.

[53] Walther Meissner and Robert Ochsenfeld. Ein neuer effekt bei eintritt der supraleitfähigkeit. *Naturwissenschaften*, 21(44):787–788, 1933.

[54] Cornelis Jacobus Gorter and H Casimir. On supraconductivity I. *Physica*, 1(1-6): 306–320, 1934.

[55] Fritz London and Heinz London. The electromagnetic equations of the supraconductor. *Proceedings of the Royal Society of London. Series A-Mathematical and Physical Sciences*, 149(866):71–88, 1935.

[56] Bascom S Deaver Jr and William M Fairbank. Experimental evidence for quantized flux in superconducting cylinders. *Physical Review Letters*, 7(2):43, 1961.

[57] Lev Davidovich Landau and Vitaly Lazarevich Ginzburg. On the theory of superconductivity. *Zh. Eksp. Teor. Fiz.*, 20:1064, 1950.

[58] Richard P Feynman. Chapter II Application of quantum mechanics to liquid helium. In *Progress in low temperature physics*, volume 1, pages 17–53. Elsevier, 1955.

[59] Alexei Alexeyevich Abrikosov. The magnetic properties of superconducting alloys. *Journal of Physics and Chemistry of Solids*, 2(3):199–208, 1957.

[60] Herbert Fröhlich. Theory of the superconducting state. I. The ground state at the absolute zero of temperature. *Physical Review*, 79(5):845, 1950.

[61] CA Reynolds, B Serin, WH Wright, and LB Nesbitt. Superconductivity of isotopes of mercury. *Physical Review*, 78(4):487, 1950.

[62] John Bardeen, Leon N Cooper, and J Robert Schrieffer. Microscopic theory of superconductivity. *Physical Review*, 106(1):162, 1957.

[63] Leon N Cooper. Bound electron pairs in a degenerate Fermi gas. *Physical Review*, 104 (4):1189, 1956.

[64] Lev Petrovich Gor'kov. Microscopic derivation of the Ginzburg-Landau equations in the theory of superconductivity. *Sov. Phys. JETP*, 9(6):1364–1367, 1959.

[65] Brian David Josephson. Possible new effects in superconductive tunnelling. *Physics Letters*, 1(7):251–253, 1962.

[66] J George Bednorz and K Alex Müller. Possible high T_c superconductivity in the Ba-La- Cu- O system. *Zeitschrift für Physik B Condensed Matter*, 64(2):189–193, 1986.

[67] Hidenori Takagi, Shin-ichi Uchida, Koichi Kitazawa, and Shoji Tanaka. High-T_c superconductivity of La-Ba-Cu oxides. II.–specification of the superconducting phase. *Japanese journal of applied physics*, 26(2A):L123, 1987.

[68] Chu CW. Evidence for superconductivity above 40 K in the La-Ba-Cu-O compound system. *Physical Review Letters*, 58(4):405, 1987.

[69] RJ Cava, RB Van Dover, B Batlogg, and EA Rietman. Bulk superconductivity at 36 K in La 1.8 Sr 0.2 CuO 4. *Physical Review Letters*, 58(4):408, 1987.

[70] CW Chu, PH Hor, RL Meng, L Gao, and ZJ Huang. Superconductivity at 52.5 K in the lanthanum-barium-copper-oxide system. *Science*, 235(4788):567–569, 1987.

[71] ZY Ran, X Chu, JH Wang, DN Zheng, SL Jia, ZH Mai, and ZX Zhao. On the 110K superconducting phase in the Bi-Sr-Ca-Cu oxide system. *Modern Physics Letters B*, 2 (05):699–706, 1988.

[72] Pierre-Gilles De Gennes. *Superconductivity of metals and alloys.* CRC Press, 2018.

[73] Michael Tinkham. *Introduction to superconductivity.* Courier Corporation, 2004.

[74] Geoffrey Stenuit, Sébastien Michotte, Jan Govaerts, and Luc Piraux. Temperature dependence of penetration and coherence lengths in lead nanowires. *Superconductor Science and Technology*, 18(1):174, 2004.

[75] José A Flores-Livas, Lilia Boeri, Antonio Sanna, Gianni Profeta, Ryotaro Arita, and Mikhail Eremets. A perspective on conventional high-temperature superconductors at high pressure: Methods and materials. *Physics Reports*, 856:1–78, 2020.

[76] Werner Buckel and Reinhold Kleiner. *Superconductivity: fundamentals and applications.* John Wiley & Sons, 2008.

[77] Heike Kamerlingh Onnes. Investigations into the properties of substances at low temperatures, which have led, amongst other things, to the preparation of liquid helium. *Nobel lecture*, 4:306–336, 1913.

[78] Frank Steglich, J Aarts, CD Bredl, W Lieke, D Meschede, W Franz, and H Schäfer. Superconductivity in the Presence of Strong Pauli Paramagnetism: $CeCu_2Si_2$. *Physical Review Letters*, 43(25):1892, 1979.

[79] A Hebard, M Rosseinky, R Haddon, D Murphy, S Glarum, T Palstra, A Ramirez, and A Karton. Potassium-doped C60. *Nature*, 350:600–601, 1991.

[80] ZK Tang, Lingyun Zhang, Ning Wang, XX Zhang, GH Wen, GD Li, JN Wang, Che Ting Chan, and Ping Sheng. Superconductivity in 4 angstrom single-walled carbon nanotubes. *Science*, 292(5526):2462–2465, 2001.

[81] Yoichi Kamihara, Takumi Watanabe, Masahiro Hirano, and Hideo Hosono. Iron-based layered superconductor La $[O_{1-x}\ F_x]$ FeAs (x= 0.05- 0.12) with $T_c = 26$K. *Journal of the American Chemical Society*, 130(11):3296–3297, 2008.

[82] Elliot Snider, Nathan Dasenbrock-Gammon, Raymond McBride, Mathew Debessai, Hiranya Vindana, Kevin Vencatasamy, Keith V Lawler, Ashkan Salamat, and Ranga P Dias. Room-temperature superconductivity in a carbonaceous sulfur hydride. *Nature*, 586(7829):373–377, 2020.

[83] Pia Jensen Ray. *Structural Investigation of La (2-x) Sr (x) CuO (4+ y): Following a Staging as a Function of Temperature.* Niels Bohr Institute, Copenhagen University, 2015.

[84] Maw-Kuen Wu, Jo R Ashburn, ClJ Torng, Ph H Hor, Rl L Meng, Lo Gao, Z Jo Huang, YQ Wang, and aCW Chu. Superconductivity at 93 K in a new mixed-phase Y-Ba-Cu-O compound system at ambient pressure. *Physical Review Letters*, 58(9):908, 1987.

[85] Hiroshi Maeda, Yoshiaki Tanaka, Masao Fukutomi, and Toshihisa Asano. A new high-T_c oxide superconductor without a rare earth element. *Japanese Journal of Applied Physics*, 27(2A):L209, 1988.

[86] Hideo Hosono, Akiyasu Yamamoto, Hidenori Hiramatsu, and Yanwei Ma. Recent advances in iron-based superconductors toward applications. *Materials today*, 21(3):278–302, 2018.

[87] Qimiao Si, Rong Yu, and Elihu Abrahams. High-temperature superconductivity in iron pnictides and chalcogenides. *Nature Reviews Materials*, 1(4):1–15, 2016.

[88] Hideo Hosono and Kazuhiko Kuroki. Iron-based superconductors: Current status of materials and pairing mechanism. *Physica C: Superconductivity and its Applications*, 514:399–422, 2015.

[89] Morton E Jones and Richard E Marsh. The preparation and structure of magnesium boride, MgB_2. *Journal of the American Chemical Society*, 76(5):1434–1436, 1954.

[90] Jun Nagamatsu, Norimasa Nakagawa, Takahiro Muranaka, Yuji Zenitani, and Jun Akimitsu. Superconductivity at 39 K in magnesium diboride. *nature*, 410(6824):63–64, 2001.

[91] Cristina Buzea and Tsutomu Yamashita. Review of the superconducting properties of MgB_2. *Superconductor Science and Technology*, 14(11):R115, 2001.

[92] Victor Moshchalkov, Mariela Menghini, Taichiro Nishio, QH Chen, AV Silhanek, Vu Hung Dao, LF Chibotaru, ND Zhigadlo, and J Karpinski. Type-1.5 Superconductivity. *Physical Review Letters*, 102(11):117001, 2009.

[93] Benjamin J Senkowicz, Jonathan E Giencke, Satyabrata Patnaik, Chang-Beom Eom, Eric E Hellstrom, and David C Larbalestier. Improved upper critical field in bulk-form magnesium diboride by mechanical alloying with carbon. *Applied Physics Letters*, 86 (20):202502, 2005.

[94] T Skoskiewicz. Superconductivity in the palladium-hydrogen and palladium-nickel-hydrogen systems. *physica status solidi (a)*, 11(2):K123–K126, 1972.

[95] B Stritzker and W Buckel. Superconductivity in the palladium-hydrogen and the palladium-deuterium systems. *Zeitschrift für Physik A Hadrons and nuclei*, 257(1): 1–8, 1972.

[96] SS Kalsi, D Aized, B Conner, G Snitchier, J Campbell, RE Schwall, J Kellers, Th Stephanblome, A Tromm, and P Winn. HTS SMES magnet design and test results. *IEEE transactions on applied superconductivity*, 7(2):971–976, 1997.

[97] WA Little. Possibility of synthesizing an organic superconductor. *Physical Review*, 134 (6A):A1416, 1964.

[98] John Singleton and Charles Mielke. Quasi-two-dimensional organic superconductors: a review. *Contemporary Physics*, 43(2):63–96, 2002.

[99] Klaus Bechgaard, Kim Carneiro, Malte Olsen, Finn Berg Rasmussen, and Claus S Jacobsen. Zero-Pressure Organic Superconductor: Di-(Tetramethyltetraselenafulvalenium)-Perchlorate [(TMTSF) $2ClO_4$]. *Physical Review Letters*, 46(13):852, 1981.

[100] Wynn CG Ho, MJP Wijngaarden, Philip Chang, Craig O Heinke, Dany Page, Mikhail Beznogov, and Daniel J Patnaude. Cooling of the Cassiopeia A neutron star and the effect of diffusive nuclear burning. In *AIP Conference Proceedings*, volume 2127, page 020007. AIP Publishing LLC, 2019.

[101] Sean A Hartnoll, Christopher P Herzog, and Gary T Horowitz. Building a holographic superconductor. *Physical Review Letters*, 101(3):031601, 2008.

[102] Gary T Horowitz. Introduction to holographic superconductors. In *From gravity to thermal gauge theories: the AdS/CFT correspondence*, pages 313–347. Springer, 2011.

[103] Pallab Basu, Anindya Mukherjee, and Hsien-Hang Shieh. Supercurrent: vector hair for an AdS black hole. *Physical Review D*, 79(4):045010, 2009.

[104] MA Obolenskii, AV Bondarenko, VI Beletskii, VN Morgun, and VP Popov. Synthesis and physical properties of $YBa_2Cu_3O_7$ single crystals. *Fizika Nizkikh Temperatur*, 16: 1103–1127, 1990.

[105] Hyung-Woo Lee, Ki-Chan Kim, and Ju Lee. Review of maglev train technologies. *IEEE transactions on magnetics*, 42(7):1917–1925, 2006.

[106] Yuri Lvovsky, Ernst Wolfgang Stautner, and Tao Zhang. Novel technologies and configurations of superconducting magnets for MRI. *Superconductor Science and Technology*, 26(9):093001, 2013.

[107] Ewald Moser, Elmar Laistler, Franz Schmitt, and Georg Kontaxis. Ultra-high field NMR and MRI—the role of magnet technology to increase sensitivity and specificity. *Frontiers in Physics*, 5:33, 2017.

[108] Takashi Nakamura, Daiki Tamada, Yousuke Yanagi, Yoshitaka Itoh, Takahiro Nemoto, Hiroaki Utumi, and Katsumi Kose. Development of a superconducting bulk magnet for NMR and MRI. *Journal of Magnetic Resonance*, 259:68–75, 2015.

[109] Anthony J Annunziata, Orlando Quaranta, Daniel F Santavicca, Alessandro Casaburi, Luigi Frunzio, Mikkel Ejrnaes, Michael J Rooks, Roberto Cristiano, Sergio Pagano, Aviad Frydman, et al. Reset dynamics and latching in niobium superconducting nanowire single-photon detectors. *Journal of Applied Physics*, 108(8):084507, 2010.

[110] Davide Uglietti. A review of commercial high temperature superconducting materials for large magnets: from wires and tapes to cables and conductors. *Superconductor Science and Technology*, 32(5):053001, 2019.

[111] C Homan, C Cummings, and C Fowler. Superconducting augmented rail gun (SARG). *IEEE Transactions on magnetics*, 22(6):1527–1531, 1986.

[112] Yiying Wu, Benjanim Messer, and Peidong Yang. Superconducting MgB_2 Nanowires. *Advanced Materials*, 13(19):1487–1489, 2001.

[113] Jacob Oestergaard, Jan Okholm, Karin Lomholt, and Ole Toennesen. Energy losses of superconducting power transmission cables in the grid. *IEEE transactions on applied superconductivity*, 11(1):2375–2378, 2001.

[114] RC Jaklevic, John Lambe, AH Silver, and JE Mercereau. Quantum interference effects in Josephson tunneling. *Physical Review Letters*, 12(7):159, 1964.

[115] Philip W Anderson and John M Rowell. Probable observation of the Josephson superconducting tunneling effect. *Physical Review Letters*, 10(6):230, 1963.

[116] RL Fagaly. Superconducting quantum interference device instruments and applications. *Review of Scientific Instruments*, 77(10):101101, 2006.

[117] Maria José Martínez-Pérez and Dieter Koelle. NanoSQUIDs: Basics & recent advances. *Superconductors at the Nanoscale*, pages 339–382, 2017.

[118] Julian Kelly, Rami Barends, Austin G Fowler, Anthony Megrant, Evan Jeffrey, Theodore C White, Daniel Sank, Josh Y Mutus, Brooks Campbell, Yu Chen, et al. State preservation by repetitive error detection in a superconducting quantum circuit. *Nature*, 519(7541):66–69, 2015.

[119] Frank Arute, Kunal Arya, Ryan Babbush, Dave Bacon, Joseph C Bardin, Rami Barends, Rupak Biswas, Sergio Boixo, Fernando GSL Brandao, David A Buell, et al. Quantum supremacy using a programmable superconducting processor. *Nature*, 574 (7779):505–510, 2019.

[120] Michel H Devoret, Andreas Wallraff, and John M Martinis. Superconducting qubits: A short review. *arXiv preprint cond-mat/0411174*, 2004.

[121] Mark W Johnson, Mohammad HS Amin, Suzanne Gildert, Trevor Lanting, Firas Hamze, Neil Dickson, Richard Harris, Andrew J Berkley, Jan Johansson, Paul Bunyk, et al. Quantum annealing with manufactured spins. *Nature*, 473(7346):194–198, 2011.

[122] John M Goodkind. The superconducting gravimeter. *Review of Scientific Instruments*, 70(11):4131–4152, 1999.

[123] R Stolz, M Schmelz, V Zakosarenko, C Foley, K Tanabe, X Xie, and RL Fagaly. Superconducting sensors and methods in geophysical applications. *Superconductor Science and Technology*, 34(3):033001, 2021.

[124] Daniel Bratton, Da Yang, Junyan Dai, and Christopher K Ober. Recent progress in high resolution lithography. *Polymers for Advanced Technologies*, 17(2):94–103, 2006.

[125] Yifang Chen. Nanofabrication by electron beam lithography and its applications: A review. *Microelectronic Engineering*, 135:57–72, 2015.

[126] Ping Li, Siyu Chen, Houfu Dai, Zhengmei Yang, Zhiquan Chen, Yasi Wang, Yiqin Chen, Wenqiang Peng, Wubin Shan, and Huigao Duan. Recent advances in focused ion beam nanofabrication for nanostructures and devices: fundamentals and applications. *Nanoscale*, 13(3):1529–1565, 2021.

[127] José María De Teresa. Nanoscale direct-write fabrication of superconducting devices for application in quantum technologies. *Materials for Quantum Technology*, 2023.

[128] Fabrizio Porrati, Sven Barth, Roland Sachser, Oleksandr V Dobrovolskiy, Anja Seybert, Achilleas S Frangakis, and Michael Huth. Crystalline niobium carbide superconducting nanowires prepared by focused ion beam direct writing. *ACS nano*, 13(6): 6287–6296, 2019.

[129] Peter K Day, Henry G LeDuc, Benjamin A Mazin, Anastasios Vayonakis, and Jonas Zmuidzinas. A broadband superconducting detector suitable for use in large arrays. *Nature*, 425(6960):817–821, 2003.

[130] Alex D Semenov, Gregory N Gol'tsman, and Alexander A Korneev. Quantum detection by current carrying superconducting film. *Physica C: Superconductivity*, 351(4):349–356, 2001.

[131] John R Clem and Karl K Berggren. Geometry-dependent critical currents in superconducting nanocircuits. *Physical Review B*, 84(17):174510, 2011.

[132] GR Berdiyorov, MV Milošević, and FM Peeters. Spatially dependent sensitivity of superconducting meanders as single-photon detectors. *Applied Physics Letters*, 100 (26):262603, 2012.

[133] Abhijit Biswas, Ilker S Bayer, Alexandru S Biris, Tao Wang, Enkeleda Dervishi, and Franz Faupel. Advances in top–down and bottom–up surface nanofabrication: Techniques, applications & future prospects. *Advances in colloid and interface science*, 170 (1-2):2–27, 2012.

[134] D Mailly. Nanofabrication techniques. *The European Physical Journal Special Topics*, 172(1):333–342, 2009.

[135] John Melngailis. Focused ion beam technology and applications. *Journal of Vacuum Science & Technology B: Microelectronics Processing and Phenomena*, 5(2):469–495, 1987.

[136] T Thurn-Albrecht, J Schotter, Gi A Kastle, N Emley, T Shibauchi, L Krusin-Elbaum, K Guarini, CT Black, MT Tuominen, and TP Russell. Ultrahigh-density nanowire arrays grown in self-assembled diblock copolymer templates. *Science*, 290(5499):2126–2129, 2000.

[137] E Zeldov, AI Larkin, VB Geshkenbein, M Konczykowski, D Majer, B Khaykovich, VM Vinokur, and H Shtrikman. Geometrical barriers in high-temperature superconductors. *Physical Review Letters*, 73(10):1428, 1994.

[138] Maamar Benkraouda and John R Clem. Critical current from surface barriers in type-II superconducting strips. *Physical Review B*, 58(22):15103, 1998.

[139] LD Landau and IM Khalatnikov. On the theory of superconductivity. Collected Papers of LD Landau, 1965.

[140] LD Landau and IM Khalatnikov. On the anomalous absorption of sound near a second order phase transition point. In *Dokl. Akad. Nauk SSSR*, volume 96, page 25, 1954.

[141] Albert Schmid. A time dependent Ginzburg-Landau equation and its application to the problem of resistivity in the mixed state. *Physik der kondensierten Materie*, 5(4): 302–317, 1966.

[142] Albert Schmid and Gerd Schön. Linearized kinetic equations and relaxation processes of a superconductor near T_c. *Journal of Low Temperature Physics*, 20(1):207–227, 1975.

[143] JC Phillips. Gapless superconductivity. *Physical Review Letters*, 10(3):96, 1963.

[144] Lorenz Kramer and RJ Watts-Tobin. Theory of dissipative current-carrying states in superconducting filaments. *Physical Review Letters*, 40(15):1041, 1978.

[145] RJ Watts-Tobin, Y Krähenbühl, and L Kramer. Nonequilibrium theory of dirty, current-carrying superconductors: Phase-slip oscillators in narrow filaments near T_c. *Journal of Low Temperature Physics*, 42(5):459–501, 1981.

[146] Lev Davidovich Landau and Evgenii Mikhailovich Lifshitz. *Course of theoretical physics, Vol 5.* Elsevier, 2013.

[147] Alexandre I Buzdin. Proximity effects in superconductor-ferromagnet heterostructures. *Reviews of Modern Physics*, 77(3):935, 2005.

[148] GR Berdiyorov, MV Milošević, and FM Peeters. Vortex configurations and critical parameters in superconducting thin films containing antidot arrays: Nonlinear Ginzburg-Landau theory. *Physical Review B*, 74(17):174512, 2006.

[149] Nikolai Kopnin. *Theory of nonequilibrium superconductivity*, volume 110. Oxford University Press, 2001.

[150] A Vl Gurevich and RG Mints. Self-heating in normal metals and superconductors. *Reviews of modern physics*, 59(4):941, 1987.

[151] James F Annett et al. *Superconductivity, superfluids and condensates*, volume 5. Oxford University Press, 2004.

[152] D Yu Vodolazov, FM Peeters, Mathieu Morelle, and Victor V Moshchalkov. Masking effect of heat dissipation on the current-voltage characteristics of a mesoscopic superconducting sample with leads. *Physical Review B*, 71(18):184502, 2005.

[153] J Pearl. Current distribution in superconducting films carrying quantized fluxoids. *Applied Physics Letters*, 5(4):65–66, 1964.

[154] Co Po Bean. Magnetization of hard superconductors. *Physical Review Letters*, 8(6): 250, 1962.

[155] Charles P Bean. Magnetization of high-field superconductors. *Reviews of Modern Physics*, 36(1):31, 1964.

[156] D Yu Vodolazov. Saddle point states in two-dimensional superconducting films biased near the depairing current. *Physical Review B*, 85(17):174507, 2012.

[157] Mauro M Doria, JE Gubernatis, and D Rainer. Virial theorem for Ginzburg-Landau theories with potential applications to numerical studies of type-II superconductors. *Physical Review B*, 39(13):9573, 1989.

[158] MV Milošević and R Geurts. The Ginzburg-Landau theory in application. *Physica C: Superconductivity*, 470(19):791–795, 2010.

[159] Leonardo Rodrigues Cadorim, Alexssandre de Oliveira Junior, and Edson Sardella. Ultra-fast kinematic vortices in mesoscopic superconductors: the effect of the self-field. *Scientific Reports*, 10(1):1–8, 2020.

[160] BJ Baelus and FM Peeters. Dependence of the vortex configuration on the geometry of mesoscopic flat samples. *Physical Review B*, 65(10):104515, 2002.

[161] U Essmann and H Träuble. The direct observation of individual flux lines in type-II superconductors. *Physics Letters A*, 24(10):526–527, 1967.

[162] JR Clem. Paper K36. 06. *Bull. Am. Phys. Soc*, 43:411, 1998.

[163] Gheorghe Stan, Stuart B Field, and John M Martinis. Critical field for complete vortex expulsion from narrow superconducting strips. *Physical Review Letters*, 92(9):097003, 2004.

[164] Aleksej A Abrikosov. Nobel Lecture: Type-II superconductors and the vortex lattice. *Reviews of modern physics*, 76(3):975, 2004.

[165] GM Maksimova. Mixed state and critical current in narrow semiconducting films. *Physics of the Solid State*, 40(10):1607–1610, 1998.

[166] Evgeny F Talantsev, AE Pantoja, Wayne P Crump, and Jeffery L Tallon. Current distribution across type-II superconducting films: a new vortex-free critical state. *Scientific Reports*, 8(1):1–9, 2018.

[167] Evgeny F Talantsev and Jeffery L Tallon. Universal self-field critical current for thin-film superconductors. *Nature Communications*, 6(1):1–8, 2015.

[168] Evgeny F Talantsev, Wayne P Crump, and Jeffery L Tallon. Universal scaling of the self-field critical current in superconductors: from sub-nanometre to millimetre size. *Scientific Reports*, 7(1):1–15, 2017.

[169] Andrey A Elistratov, Denis Yu Vodolazov, Igor L Maksimov, and John R Clem. Field-dependent critical current in type-II superconducting strips: Combined effect of bulk pinning and geometrical edge barrier. *Physical Review B*, 66(22):220506, 2002.

[170] BI Ivlev and NB Kopnin. Electric currents and resistive states in thin superconductors. *Advances of Physics*, 33(1):47–114, 1984.

[171] James S Langer and Vinay Ambegaokar. Intrinsic resistive transition in narrow superconducting channels. *Physical Review*, 164(2):498, 1967.

[172] Shuichi Tahara, Steven M Anlage, J Halbritter, Chang-Beom Eom, DK Fork, TH Geballe, and MR Beasley. Critical currents, pinning, and edge barriers in narrow $YB_2Cu_3O_{7-\delta}$ thin films. *Physical Review B*, 41(16):11203, 1990.

[173] D Kouzoudis, M Breitwisch, and DK Finnemore. Edge barrier pinning for a single superconducting vortex. *Physical Review B*, 60(14):10508, 1999.

[174] MR Koblischka and Masato Murakami. Pinning mechanisms in bulk high-T_c superconductors. *Superconductor Science and Technology*, 13(6):738, 2000.

[175] Günter Zerweck. On pinning of superconducting flux lines by grain boundaries. *Journal of Low Temperature Physics*, 42(1):1–9, 1981.

[176] IL Maksimov, RM Ainbinder, and D Yu Vodolazov. Anomalous peak-effect in type-II superconductors: A competition between bulk pinning and a surface barrier. *Physica C: Superconductivity and its applications*, 451(2):127–133, 2007.

[177] VV Shmidt and AA Balkov. Critical current in superconducting films. *Sov. Phys. JETP*, 30(6):1137–1142, 1970.

[178] T Yamashita and L Rinderer. Temperature dependence of the vortex nucleation field of thin-film, type-II superconductors. *Journal of Low Temperature Physics*, 24(5): 695–699, 1976.

[179] D Dew-Hughes. Flux pinning mechanisms in type-II superconductors. *Philosophical Magazine*, 30(2):293–305, 1974.

[180] M Vélez, JI Martín, JE Villegas, Axel Hoffmann, EM González, JL Vicent, and Ivan K Schuller. Superconducting vortex pinning with artificial magnetic nanostructures. *Journal of Magnetism and Magnetic Materials*, 320(21):2547–2562, 2008.

[181] GR Berdiyorov, MV Milošević, and FM Peeters. Novel commensurability effects in superconducting films with antidot arrays. *Physical Review Letters*, 96(20):207001, 2006.

[182] D Yu Vodolazov, BA Gribkov, SA Gusev, A Yu Klimov, Yu N Nozdrin, VV Rogov, and SN Vdovichev. Considerable enhancement of the critical current in a superconducting film by a magnetized magnetic strip. *Physical Review B*, 72(6):064509, 2005.

[183] O-A Adami, ŽL Jelić, Cun Xue, Mahmoud Abdel-Hafiez, Benoit Hackens, Victor V Moshchalkov, MV Milošević, Joris Van de Vondel, and AV Silhanek. Onset, evolution, and magnetic braking of vortex lattice instabilities in nanostructured superconducting films. *Physical Review B*, 92(13):134506, 2015.

[184] D Yu Vodolazov, K Ilin, M Merker, and M Siegel. Defect-controlled vortex generation in current-carrying narrow superconducting strips. *Superconductor Science and Technology*, 29(2):025002, 2015.

[185] AI Bezuglyj, VA Shklovskij, B Budinska, B Aichner, VM Bevz, M Yu Mikhailov, D Yu Vodolazov, W Lang, and OV Dobrovolskiy. Vortex jets generated by edge defects in current-carrying superconductor thin strips. *arXiv preprint arXiv:2204.06467*, 2022.

[186] DY Vodolazov and FM Peeters. Superconducting rectifier based on the asymmetric surface barrier effect. *Physical Review B*, 72(17):172508, 2005.

[187] Hans Hilgenkamp and Jochen Mannhart. Grain boundaries in high-T_c superconductors. *Reviews of Modern Physics*, 74(2):485, 2002.

[188] JH Durrell, CB Eom, A Gurevich, EE Hellstrom, C Tarantini, A Yamamoto, and DC Larbalestier. The behavior of grain boundaries in the Fe-based superconductors. *Reports on Progress in Physics*, 74(12):124511, 2011.

[189] AT Fiory. Quantum interference effects of a moving vortex lattice in Al films. *Physical Review Letters*, 27(8):501, 1971.

[190] JM Harris, Nai Phuan Ong, R Gagnon, and L Taillefer. Washboard Frequency of the Moving Vortex Lattice in $YBa_2Cu_3O_6$.93 Detected by ac-dc Interference. *Physical Review Letters*, 74(18):3684, 1995.

[191] Yoshihiko Togawa, Ryuichi Abiru, Katsuya Iwaya, Haruhisa Kitano, and Atsutaka Maeda. Direct Observation of the Washboard Noise of a Driven Vortex Lattice in a High-Temperature Superconductor, $Bi_2Sr_2CaCu_2O_y$. *Physical Review Letters*, 85(17): 3716, 2000.

[192] OV Dolgov and N Schopohl. Transition radiation of moving Abrikosov vortices. *Physical Review B*, 61(18):12389, 2000.

[193] Oleksandr V Dobrovolskiy, Roland Sachser, Michael Huth, Valerij A Shklovskij, Ruslan V Vovk, Volodymyr M Bevz, and Menachem I Tsindlekht. Radiofrequency generation by coherently moving fluxons. *Applied Physics Letters*, 112(15):152601, 2018.

[194] HA Hafez, X Chai, A Ibrahim, S Mondal, D Férachou, X Ropagnol, and T Ozaki. Intense terahertz radiation and their applications. *Journal of Optics*, 18(9):093004, 2016.

[195] Joo-Hiuk Son, Seung Jae Oh, and Hwayeong Cheon. Potential clinical applications of terahertz radiation. *Journal of Applied Physics*, 125(19):190901, 2019.

[196] A A Gowen, Créidhe O'Sullivan, and CP O'Donnell. Terahertz time domain spectroscopy and imaging: Emerging techniques for food process monitoring and quality control. *Trends in Food Science & Technology*, 25(1):40–46, 2012.

[197] GR Berdiyorov, MV Milošević, and FM Peeters. Kinematic vortex-antivortex lines in strongly driven superconducting stripes. *Physical Review B*, 79(18):184506, 2009.

[198] Michael Rosticher, FR Ladan, JP Maneval, SN Dorenbos, T Zijlstra, TM Klapwijk, V Zwiller, A Lupaşcu, and Gilles Nogues. A high efficiency superconducting nanowire single electron detector. *Applied Physics Letters*, 97(18):183106, 2010.

[199] LN Bulaevskii, MJ Graf, CD Batista, and VG Kogan. Vortex-induced dissipation in narrow current-biased thin-film superconducting strips. *Physical Review B*, 83(14): 144526, 2011.

[200] Dmitry A Orlov, M Lestinsky, F Sprenger, D Schwalm, AS Terekhov, and A Wolf. Ultra-Cold Electron Beams for the Heidelberg TSR and CSR. In *AIP Conference Proceedings*, volume 821, pages 478–487. American Institute of Physics, 2006.

[201] DA Orlov, F Sprenger, M Lestinsky, U Weigel, AS Terekhov, D Schwalm, and A Wolf. Photocathodes as electron sources for high resolution merged beam experiments. In *Journal of Physics: Conference Series*, volume 4, page 045. IOP Publishing, 2005.

[202] Francesco Giazotto, Tero T Heikkilä, Arttu Luukanen, Alexander M Savin, and Jukka P Pekola. Opportunities for mesoscopics in thermometry and refrigeration: Physics and applications. *Reviews of Modern Physics*, 78(1):217, 2006.

[203] AN Zotova and D Yu Vodolazov. Photon detection by current-carrying superconducting film: A time-dependent Ginzburg-Landau approach. *Physical Review B*, 85(2): 024509, 2012.

[204] R Lusche, A Semenov, K Ilin, M Siegel, Y Korneeva, A Trifonov, A Korneev, G Goltsman, Denis Vodolazov, and H-W Hübers. Effect of the wire width on the intrinsic detection efficiency of superconducting-nanowire single-photon detectors. *Journal of Applied Physics*, 116(4):043906, 2014.

[205] A Korneev, P Kouminov, V Matvienko, G Chulkova, K Smirnov, B Voronov, GN Gol'tsman, M Currie, W Lo, K Wilsher, et al. Sensitivity and gigahertz counting performance of NbN superconducting single-photon detectors. *Applied Physics Letters*, 84(26):5338–5340, 2004.

[206] G Gol'Tsman, O Okunev, G Chulkova, A Lipatov, A Dzardanov, K Smirnov, A Semenov, B Voronov, C Williams, and Roman Sobolewski. Fabrication and properties of an ultrafast NbN hot-electron single-photon detector. *IEEE Transactions on applied superconductivity*, 11(1):574–577, 2001.

[207] WeiJun Zhang, LiXing You, Hao Li, Jia Huang, ChaoLin Lv, Lu Zhang, XiaoYu Liu, JunJie Wu, Zhen Wang, and XiaoMing Xie. NbN superconducting nanowire single photon detector with efficiency over 90% at 1550 nm wavelength operational at compact cryocooler temperature. *Science China Physics, Mechanics & Astronomy*, 60 (12):1–10, 2017.

[208] Can Yang, Mengting Si, Xingyu Zhang, Aobo Yu, Jia Huang, Yiming Pan, Hao Li, Lingyun Li, Zhen Wang, Shuo Zhang, et al. Large-area TaN superconducting microwire single photon detectors for X-ray detection. *Optics Express*, 29(14):21400–21408, 2021.

[209] A Verevkin, J Zhang, Roman Sobolewski, A Lipatov, O Okunev, G Chulkova, A Korneev, K Smirnov, GN Gol'tsman, and A Semenov. Detection efficiency of large-active-area NbN single-photon superconducting detectors in the ultraviolet to near-infrared range. *Applied Physics Letters*, 80(25):4687–4689, 2002.

[210] Yu P Korneeva, D Yu Vodolazov, AV Semenov, IN Florya, N Simonov, E Baeva, AA Korneev, GN Goltsman, and TM Klapwijk. Optical single-photon detection in micrometer-scale NbN bridges. *Physical Review Applied*, 9(6):064037, 2018.

[211] Peng Hu, Hao Li, Lixing You, Heqing Wang, You Xiao, Jia Huang, Xiaoyan Yang, Weijun Zhang, Zhen Wang, and Xiaoming Xie. Detecting single infrared photons toward optimal system detection efficiency. *Optics Express*, 28(24):36884–36891, 2020.

[212] M Tarkhov, J Claudon, J Ph Poizat, A Korneev, A Divochiy, O Minaeva, V Seleznev, N Kaurova, B Voronov, AV Semenov, et al. Ultrafast reset time of superconducting single photon detectors. *Applied Physics Letters*, 92(24):241112, 2008.

[213] Aleksander Divochiy, Francesco Marsili, David Bitauld, Alessandro Gaggero, Roberto Leoni, Francesco Mattioli, Alexander Korneev, Vitaliy Seleznev, Nataliya Kaurova, Olga Minaeva, et al. Superconducting nanowire photon-number-resolving detector at telecommunication wavelengths. *Nature Photonics*, 2(5):302–306, 2008.

[214] Andrew J Kerman, Joel KW Yang, Richard J Molnar, Eric A Dauler, and Karl K Berggren. Electrothermal feedback in superconducting nanowire single-photon detectors. *Physical Review B*, 79(10):100509, 2009.

[215] H Shibata, H Takesue, T Honjo, T Akazaki, and Y Tokura. Single-photon detection using magnesium diboride superconducting nanowires. *Applied Physics Letters*, 97(21): 212504, 2010.

[216] Mattias Hofherr, Dagmar Rall, Konstantin Ilin, Michael Siegel, Alexej Semenov, H-W Hübers, and NA Gippius. Intrinsic detection efficiency of superconducting nanowire single-photon detectors with different thicknesses. *Journal of Applied Physics*, 108(1): 014507, 2010.

[217] Alexei Semenov, Andreas Engel, H-W Hübers, Konstantin Il'in, and Michael Siegel. Spectral cut-off in the efficiency of the resistive state formation caused by absorption of a single-photon in current-carrying superconducting nano-strips. *The European Physical Journal B-Condensed Matter and Complex Systems*, 47(4):495–501, 2005.

[218] A Jukna, J Kitaygorsky, D Pan, A Cross, A Perlman, I Komissarov, O Okunev, K Smirnov, A Korneev, G Chulkova, et al. Dynamics of hotspot formation in nanostructured superconducting stripes excited with single photons. *Acta Physica Polonica-Series A General Physics*, 113(3):955–958, 2008.

[219] Joel KW Yang, Andrew J Kerman, Eric A Dauler, Vikas Anant, Kristine M Rosfjord, and Karl K Berggren. Modeling the electrical and thermal response of superconducting nanowire single-photon detectors. *IEEE transactions on applied superconductivity*, 17 (2):581–585, 2007.

[220] Lev N Bulaevskii, Matthias J Graf, and Vladimir G Kogan. Vortex-assisted photon counts and their magnetic field dependence in single-photon superconducting detectors. *Physical Review B*, 85(1):014505, 2012.

[221] Biao Zhang, Labao Zhang, Qi Chen, Yanqiu Guan, Guanglong He, Yue Fei, Xiaohan Wang, Jiayu Lyu, Jingrou Tan, Haochen Li, et al. Photon-assisted Phase Slips in Superconducting Nanowires. *Physical Review Applied*, 17(1):014032, 2022.

[222] Zhen Wang, Akira Kawakami, Yoshinori Uzawa, and Bokuji Komiyama. Superconducting properties and crystal structures of single-crystal niobium nitride thin films deposited at ambient substrate temperature. *Journal of Applied Physics*, 79(10):7837–7842, 1996.

[223] Alexei Semenov, Philipp Haas, Heinz-Wilhelm Hübers, Konstantin Ilin, Michael Siegel, Alexander Kirste, Dietemar Drung, Thomas Schurig, and Andreas Engel. Intrinsic quantum efficiency and electro-thermal model of a superconducting nanowire single-photon detector. *Journal of Modern Optics*, 56(2-3):345–351, 2009.

[224] Kendall E Atkinson. *An introduction to numerical analysis*. John wiley & sons, 2008.

[225] D Yu Vodolazov. Minimal timing jitter in superconducting nanowire single-photon detectors. *Physical Review Applied*, 11(1):014016, 2019.

[226] D Yu Vodolazov. Single-photon detection by a dirty current-carrying superconducting strip based on the kinetic-equation approach. *Physical Review Applied*, 7(3):034014, 2017.

[227] Andreas Engel, Julia Lonsky, Xiaofu Zhang, and Andreas Schilling. Detection mechanism in SNSPD: numerical results of a conceptually simple, yet powerful detection model. *IEEE Transactions on Applied Superconductivity*, 25(3):1–7, 2014.

[228] Mariia Sidorova, Alexej Semenov, Heinz-Wilhelm Hübers, Ilya Charaev, Artem Kuzmin, Steffen Doerner, and Michael Siegel. Physical mechanisms of timing jitter in photon detection by current-carrying superconducting nanowires. *Physical Review B*, 96(18):184504, 2017.

[229] Misael Caloz, Matthieu Perrenoud, Claire Autebert, Boris Korzh, Markus Weiss, Christian Schönenberger, Richard J Warburton, Hugo Zbinden, and Félix Bussières. High-detection efficiency and low-timing jitter with amorphous superconducting nanowire single-photon detectors. *Applied Physics Letters*, 112(6):061103, 2018.

[230] D Yu Vodolazov and FM Peeters. Temporary cooling of quasiparticles and delay in voltage response of superconducting bridges after abruptly switching on the supercritical current. *Physical Review B*, 90(9):094504, 2014.

[231] SI Matveenko, D Kovrizhin, S Ouvry, and GV Shlyapnikov. Vortex structures in rotating Bose-Einstein condensates. *Physical Review A*, 80(6):063621, 2009.

[232] Randall J LeVeque. *Finite difference methods for ordinary and partial differential equations: steady-state and time-dependent problems*. SIAM, 2007.

[233] Mauro M Doria, JE Gubernatis, and D Rainer. Solving the Ginzburg-Landau equations by simulated annealing. *Physical Review B*, 41(10):6335, 1990.

[234] Stephen L Adler and Tsvi Piran. Relaxation methods for gauge field equilibrium equations. *Reviews of Modern Physics*, 56(1):1, 1984.

[235] Holger Frahm, Salman Ullah, and Alan T Dorsey. Flux dynamics and the growth of the superconducting phase. *Physical Review Letters*, 66(23):3067, 1991.

[236] William D Gropp, Hans G Kaper, Gary K Leaf, David M Levine, Mario Palumbo, and Valerii M Vinokur. Numerical simulation of vortex dynamics in type-II superconductors. *Journal of Computational Physics*, 123(2):254–266, 1996.

[237] Eugene Isaacson and Herbert Bishop Keller. *Analysis of numerical methods*. Courier Corporation, 2012.

[238] T Winiecki and CS Adams. A fast semi-implicit finite-difference method for the TDGL equations. *Journal of Computational Physics*, 179(1):127–139, 2002.

[239] John Crank and Phyllis Nicolson. A practical method for numerical evaluation of solutions of partial differential equations of the heat-conduction type. *Advances in Computational Mathematics*, 6(1):207–226, 1996.

[240] Kamisetty Ramamohan Rao, Do Nyeon Kim, and Jae Jeong Hwang. *Fast Fourier transform: algorithms and applications*, volume 32. Springer, 2010.

[241] William H Press, Saul A Teukolsky, William T Vetterling, and Brian P Flannery. *Numerical recipes 3rd edition: The art of scientific computing*. Cambridge University Press, 2007.

[242] Donald W Peaceman and Henry H Rachford, Jr. The numerical solution of parabolic and elliptic differential equations. *Journal of the Society for industrial and Applied Mathematics*, 3(1):28–41, 1955.